

Dissertation
submitted to the
Combined Faculties of the Natural Sciences and Mathematics
of the Ruperto-Carola-University of Heidelberg, Germany,
for the degree of
Doctor of Natural Sciences

Put forward by
Richard Teague
born in Cheltenham, United Kingdom

Oral examination: January 20th, 2017

**TRACING THE EARLIEST STAGES OF PLANET
FORMATION THROUGH MODELLING AND SUB-MM
OBSERVATIONS**

RICHARD TEAGUE

REFEREES:

PROF. DR. THOMAS HENNING

PROF. DR. CORNELIS DULLEMOND

Abstract

This thesis explores the utility of molecular line emission as a tool to unravel the physical structures and processes involved in planet formation.

Observations of molecular ions, HCO^+ and DCO^+ , in the disk of DM Tauri allow for a study of the ionization structure. These constraints are an essential ingredient in modelling the physical and chemical evolution of a disk which directly impact the efficiency of planet formation.

We also present the first spatially resolved direct measurement of turbulence in a protoplanetary disk using CO, CN and CS molecular line emission. Such a measurement is vital in identifying the physical mechanisms driving turbulence. In addition, we perform a thorough analysis of all uncertainties involved when determining turbulent velocities in disks and demonstrate that all measurements of turbulence will be ultimately limited by the precision to which the gas temperature can be derived.

Finally, the CS emission profile from TW Hydrae displays a dip-like feature coincident with features observed in scattered light observations of the disk, suggesting a common origin. Extensive modelling demonstrates that this may be the first detection of a surface density perturbation through molecular line emission, potentially the manifestation of an embedded protoplanet or a strong magneto-rotational instability.

Zusammenfassung

Diese Dissertation untersucht die Emissionslinien unterschiedlicher Moleküle als Mittel, die physikalischen Strukturen und Prozesse der Planetenentstehung zu verstehen.

Beobachtungen der ionisierten Moleküle HCO^+ und DCO^+ in der Scheibe von DM Tauri erlauben es uns, die Ionisationsstruktur zu erkunden. Diese Bedingungen sind essentiell, um die physikalische und chemische Entwicklung der Scheibe zu simulieren, die einen direkten Einfluss auf die Effizienz der Planetenentstehung hat.

Wir zeigen die erste direkte, räumlich aufgelöste Messung von Turbulenzen in einer protoplanetarischen Scheibe anhand der Emissionslinien von CO, CN und CS. So eine Messung ist notwendig, um die physikalischen Prozesse von Turbulenzen zu analysieren. Zudem führen wir eine gründliche Analyse aller möglichen Unsicherheiten, die bei der Bestimmung turbulenter Geschwindigkeiten in Scheiben entstehen, durch und zeigen, dass alle Messungen von Turbulenzen schlussendlich davon abhängen, mit welcher Präzision die Gastemperatur bestimmt werden kann.

Des Weiteren zeigt das Emissionsprofil von CS in TW Hydra einen Abfall, der ebenfalls in Beobachtungen des reflektierten Lichtes der Scheibe zu sehen ist, was auf einen gemeinsamen Ursprung hinweist. Eine ausführliche Analyse zeigt, dass dies die erste Entdeckung einer Oberflächenperturbation anhand der Emissionslinien der Moleküle ist, die möglicherweise auf einen Protoplaneten oder eine Magneto-Rotationsinstabilität schließen lässt.

For my parents.

Contents

1	Introduction	1
1.1	The Solar System and Beyond	1
1.2	The Cradles of Planet Formation	2
1.3	Molecular Probes of Physical Conditions	6
1.4	Structure of this Thesis	13
2	Modelling a Protoplanetary Disk	17
2.1	Physical Models	17
2.2	Chemical Models	21
2.3	Radiative Transfer	26
2.4	Simulating Observations	32
3	Observing Protoplanetary Disks	35
3.1	Spectral Energy Distributions - SEDs	36
3.2	Radio Observations	37
3.3	Model Fitting	43
4	Deuterium Fractionation and Ionisation in DM Tau	47
4.1	Motivation	47
4.2	Observations	48
4.3	Chemical Modelling	52
4.4	Discussion	56
4.5	Summary	64
5	Measuring Turbulence in TW Hya	67
5.1	Motivation	67
5.2	Observations	68
5.3	Separating Turbulent Velocity Dispersions	69
5.4	Results and Discussion	75
5.5	Summary	83
6	A Surface Density Perturbation Traced by Molecular Emission	85
6.1	Motivation	85
6.2	Observations	86
6.3	Modelling Surface Density Perturbations	89

6.4	Results	91
6.5	Discussion	97
6.6	Conclusion	102
7	Summary and Outlook	103
7.1	Summary	103
7.2	Outlook	104
A	CN in TW Hya	107
B	Error Derivations for Turbulence	109
B.1	Direct Turbulent Velocity Dispersion	109
B.2	Co-spatial Kinetic Temperature	110
B.3	Co-spatial Turbulent Velocity Dispersion	110
C	Physical Models from Chapter 6	113
	Glossary	117
	Bibliography	119
	Acknowledgements	127

Introduction

1.1 The Solar System and Beyond

The study of planet formation holds a somewhat privileged position in astronomy as one of the few disciplines where we can go beyond remote sensing and visit objects of interest. Since 1959, some 89 missions have been successfully launched to study the planets, moons, comets and asteroids of the Solar System (see, for example, the stunningly detailed images of the surface of Pluto taken by NASA's *New Horizons* mission in Fig. 1.1). Of these, 40 included a successful 'soft landing', allowing for the transmission of data collected directly from surface of these bodies.

These space laboratories have enabled us to measure the mineralogical and molecular make-up of Solar System bodies to exquisite precision. For example, ESA's *Rosetta* mission and its *Philae* lander were able to measure high levels of deuteration, molecules enriched in deuterium relative to hydrogen, suggesting that the water is of a different origin to that found on Earth (Altwegg et al., 2015). Such findings allow us to paint an incredibly specific, if not fine-tuned, picture of how planet formation works in the context of the Solar System. However, it would be incredibly closed minded to consider the Solar System archetypal of all planetary systems; extrapolating what we have learned to exoplanetary systems. Indeed, the very fact that life has found a way to emerge on Earth marks the Solar System as, thus far, an anomaly.

This reasoning has been confirmed with the advent of large exoplanet (extra-solar) surveys, such as NASA's hugely successful *Kepler* mission, which alone has confirmed well over 2,000 planets, or ground-based surveys such as the HATSouth¹ and WASP² projects. Together, these efforts have led to the discovery of 3,533 confirmed planets in 2,650 planetary systems. These systems display a whole range of system architectures, unlike that of the Solar System, and are comprised of several planetary types, some of which are unrepresented in the Solar System, such as hot-Jupiters or super-Earths (Jupiter mass planets on orbits with periods of only a matter of days and planets with a mass range

¹ <http://www.mpia.de/homes/mancini/hat-south.html>

² <https://wasp-planets.net/>

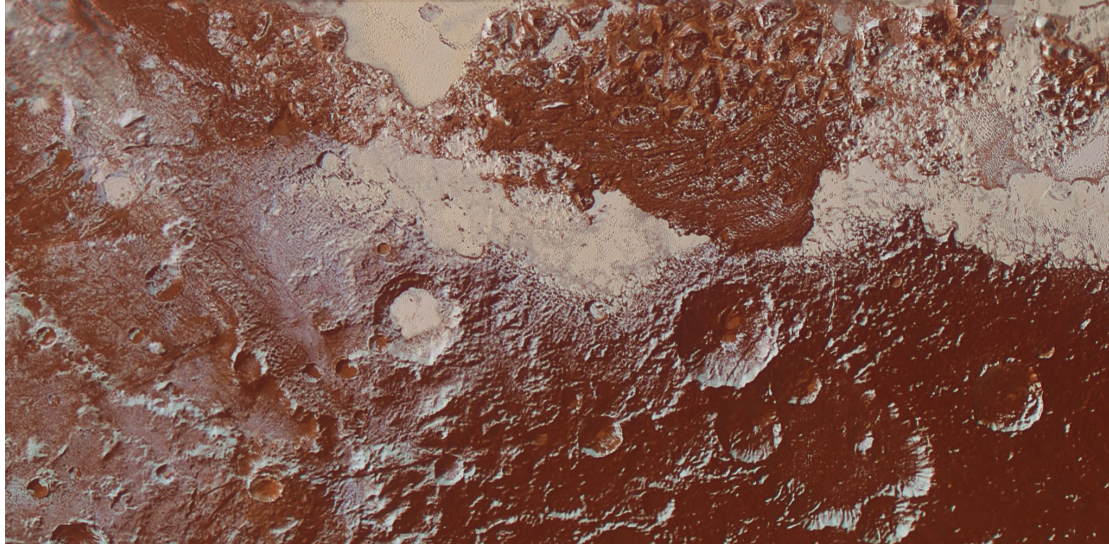


Figure 1.1 The surface of Pluto as seen by NASA’s *New Horizons* probe. The width of the image is 420 km. Volatile rich craters, indicative of extensive geological processing, can be seen in the bottom right of the image, while methane-rich ices dominate the tectonic ridges in the bottom left. Image credits: NASA / JHUAPL / SwRI.

typically $15 - 17 M_{\oplus}$, respectively). Such a diversity of planets and planetary systems challenges our planet formation theories to explain the observed menagerie of planets.

It is therefore essential to move beyond the Solar System in pursuit of understanding planet formation. While surveys will continue to add to the abundance of known planets, to truly understand the physical processes involved, we must delve into the earlier stages and understand the formation environments of these planetary systems: protoplanetary disks.

1.2 The Cradles of Planet Formation

Protoplanetary disks are a natural outcome of star formation. The star formation process begins with a gravitationally unstable fragment within a molecular cloud which collapses isothermally. As the central densities increase, the core becomes more and more opaque to its own radiation, and the internal temperature begins to rise, retarding the collapse. Eventually, the central region becomes optically opaque at $\sim 10^{-13} \text{ g cm}^{-3}$ and the collapse halts, forming the first hydrostatic core. The flow of gas on this core makes it hotter, leading first to H_2 dissociation at temperatures between 2000 and 3000 K, followed by the ionisation of atomic hydrogen at $\sim 10^4$ K. This dissociation and ionisation takes energy, allowing the core to contract further. The process continues until the internal pressure becomes high enough to counter-balance the gravitational collapse, reaching the state of hydrostatic equilibrium, and the protostar is born.

Excess material, which is slowly rotating with respect to the newly formed star, continues to collapse. Conservation of angular momentum results in the in-falling gas, which originates at positions away from the rotation axis, to form an accretion disk around the star. The continued accretion onto the star, caused by the removal of angular momentum

through turbulent viscosity, drives stellar jets and outflows and winds which blow the excess molecular cloud away over time scales of 10^4 to 10^5 years, leaving behind only a star and disk system.

Once the envelope has been removed, the disk³ is subject to the harsh radiation of the newly born star, heating the upper atmosphere while viscous heating provides an efficient energy source within the inner few au during the early stages. As the disk is in near hydrostatic equilibrium, this heating sets the vertical profile of the disk, causing the outer regions to flare. The resulting disk can be characterised by the strong radial and vertical gradients found in the temperature and density profiles.

The disk actively accretes onto the star at a rate of $\dot{M}_{\text{disk}} \sim 10^{-8} M_{\odot} \text{ yr}^{-1}$ (Gullbring et al., 1998; Andrews et al., 2010), as shown by the ultraviolet (UV) continuum excess from the continuum shock of material falling onto the central star, extremely broad emission lines, for example H α , Br γ and Ca II, and forbidden emission lines from stellar winds and jets (Hartigan et al., 1995; Muzerolle et al., 2001, 2005; Natta et al., 2006). Such accretion requires the transport of mass inwards and therefore a transport of angular momentum outwards. Shakura & Sunyaev (1973) argued (in the context of accretion disks around black holes, but adapted for protoplanetary disks) that this can be achieved through a disk-wide viscosity ν which can be described by,

$$\nu = \alpha c_s H, \quad (1.1)$$

where H is the pressure scale height of the disk, c_s is the sound speed of the gas and α is a proportionality coefficient. This α -prescription was widely adopted and gave rise to the α -disk model where disks contained a disk-wide α (see Chapter 2 and Lynden-Bell & Pringle, 1974; Pringle, 1981).

In terms of sources of viscosity, molecular viscosity and radiative viscosity are too weak to enable the angular moment transport required to produce the observed accretion rates. Instead, turbulence is believed to be the dominant source of viscosity in a disk. The most promising candidate thus far is the magneto-rotational instability (MRI) (Balbus & Hawley, 1990), where turbulence is driven due to the shear of the ionized gas which is coupled to the magnetic fields that pervade the disk. In order to be active, however, MRI requires a minimum ionization fraction, $x(e)$, for the coupling of the gas and the magnetic fields. Other hydrodynamical instabilities have been identified which do not require an ionized disk, for example the baroclinic instability (Klahr & Bodenheimer, 2003), the Rossby-wave instability (Lovelace et al., 1999), the vertical shear instability (Nelson et al., 2013), the convective over-stability (Klahr & Hubbard, 2014) and zombie vortex instabilities (Marcus et al., 2015). Despite not requiring a particular ionization fraction, these instabilities have their own requirements on the physical structure in order to be active, for example a strong vertical temperature gradient is required for a vertical shear instability. Observational constraints are required to distinguish between potential mechanisms and place limits on the level of turbulence present.

³ Hereafter disk implicitly means protoplanetary disk.

Within a disk, the refractory material locked in grains is typically $\sim 1\%$ of the disk mass⁴. These grains are shepherded together by turbulence, inciting grain growth and the start of planet formation. The first stages of growth typically proceed through coagulation where low velocity collisions on the order of 1 m s^{-1} are sufficient to begin the planet building process from grains of $a \approx \mu\text{m}$ size (Blum & Wurm, 2008).

As the grains continue to grow, physical processes are believed to limit the size which can be attained through such collisions. The ‘bouncing barrier’ limits particles to sizes of $a \lesssim 1 \text{ mm}$ as the relative velocities of such sized particles are typically such that collisions are elastic and thus do not allow coagulation (Zsom & Dullemond, 2008; Zsom et al., 2010). Similarly, at radii of a few au, the fragmentation barrier prevents slightly larger sizes of $a \approx 1 \text{ cm}$ to grow, as here collisions are typically disruptive, fragmenting the particles rather than growing them (Dullemond & Dominik, 2005).

While the small grains are well coupled with the gas, larger grains slowly decouple from the gas and settle towards the midplane. Furthermore, lacking the pressure support that gas feels, resulting in a sub-Keplerian rotation, grains experience a headwind from the gas as they continue to orbit at the Keplerian velocity. This constant perturbation results in the radial drift of grains; the slow inwards procession required to conserve angular momentum. Weidenschilling (1977) (see also Whipple, 1972) argues that this is a final barrier in the growth of grains as in the less dense outer disk, growth time scales for small grains are much smaller than for the inward drift; particles would fall into the central star before they grew to planet building sizes. This is known as the ‘meter-sized barrier’.

Self gravity is often invoked to overcome this problematic regime of planetesimal formation. With the sedimentation of grains, the midplane becomes progressively more massive until the dust mass becomes such that fragments can collapse under their own gravity (Safronov, 1972; Goldreich & Ward, 1973). The exact dynamical process which sets off this collapse is currently unknown, however recent theoretical work shows, however, that even with favourable conditions, these mechanisms require a high density of $\sim 10 \text{ cm}$ sized grains which still prove a challenge to create (Cuzzi et al., 2016). As a turbulent midplane can limit the sedimentation of grains, preventing this scenario, observational constraints are sorely needed to understand the dynamics of the midplanes of disks.

Alternatively, the streaming instability has shown great promise in quickly growing metre-sized particles to km-sized planetesimals (Youdin & Goodman, 2005; Johansen et al., 2007). The collective drag force of a clump of particles will resist the radial drift of the clump, allowing for particles which are drifting inwards at faster velocities to collide contribute to the over density. However, this clumping requires an extremely low gas-to-dust ratios of $\lesssim 10 \%$ (Johansen et al., 2009; Carrera et al., 2015), which may not be achievable. Drążkowska & Dullemond (2014) suggest that this would only be likely

⁴ There is currently much debate over the gas-to-dust ratio in disks. While many believe disks inherit the interstellar medium (ISM) value of 100, recent observations, e.g. Ansdell et al. (2016), challenge this, finding ratios of ~ 10 . This is discussed later in Section 1.3.

in the outer disk due to the increased Stokes numbers of the particles involved and the abundances of ices enhancing the sticking properties of the grains.

These theories all assume dust particles to be nicely spherical, as is the wont of physicists. A more realistic assumption is that the grains residing in disks will be extremely porous with collisions building fluffy aggregates outside the water snowline (Okuzumi et al., 2012; Kataoka et al., 2013). Due to the porosity of such grains, they can withstand considerably higher velocity collisions, while coupling more effectively to the gas, minimising the radial drift. These attributes allow such fluffy aggregates to efficiently form km-sized bodies, circumventing the meter and bouncing barriers. Distinguishing the presence of these particles remains a challenge.

Beyond these sizes, in the regime of km-sized bodies, gravity becomes the dominant agent in further growth of the planetesimals and the final stages of planet formation are, in relative terms, easy. Runaway growth occurs as large planetesimals accrete the surround material with gravitational focussing increasing the effective cross section of the larger body, a phase known as pebble accretion (Ormel & Klahr, 2010). The region around the body from which material is accreted is known as the feeding zone and scales as

$$\sigma_{\text{feeding}} = \pi a^2 \left(1 + \left[\frac{v_{\text{esc}}}{v_{\text{rel}}} \right]^2 \right), \quad (1.2)$$

where v_{esc} and v_{rel} are the escape and relative velocities of the colliding planetesimals respectively (Lissauer, 1993). Building bodies up to sizes of ~ 100 km (Wetherill & Stewart, 1989; Thommes et al., 2003), these large bodies will perturb smaller bodies in their wake, reducing the efficiency of the accretion and growth of other bodies, thus entering a regime of oligarchic growth (Thommes & Duncan, 2006). Smaller particle sizes, such as fragments from previous collisions or boulders, are more readily accreted as they are more likely to be kept dynamically cold.

While these processes yield an abundance of Mars-mass planets, they struggle to produce Earth and Venus analogues and the cores necessary to see gas-giant formation (a core of $\sim 10 M_{\oplus}$ is required for runaway gas accretion). A disk mass an order of magnitude larger is necessary to overcome these issues with in-situ formation. Unfortunately, current estimates of disk masses, both the dust and gas masses, suffer from uncertainties of around an order of magnitude each, leaving a huge amount of uncertainty this particular problem.

The mechanism is known as the core accretion scenario and currently the most widely accepted scenario. A competing theory is the disk instability scenario where a disk is sufficiently massive that it fragments and quickly collapses to planetesimals. However, rotating disks are linearly stable to perturbations and would quickly stabilize through the formation of spiral arms (Gammie, 2001). Furthermore, this process is incredibly sensitive to the cooling rate of the disk as if the over-densities do not cool fast enough they can be easily sheared apart due to the rotation of the disk (Rice et al., 2005). As the disk masses are so poorly constrained, temperature structures must be used in conjunction

to understand the feasibility of self-gravity induced planet formation and to potentially place constraints on the cooling rates of disks.

In the final stages of the disk's lifetime, material from the disk continues to accrete onto the central star, the inner regions of the disk will slowly drain and observational signatures of accretion start to become scarcer (Hartigan et al., 1995). Using the presence of an infra-red (IR)-bright inner disk as a proxy for disk lifetimes, Mamajek (2009) estimate that protoplanetary disks have a lifetime of between 2 and 3 Myrs, while Fedele et al. (2010), in a survey of stellar clusters in the 1 to 50 Myr range, found no accretion signatures for systems older than 10 Myrs.

Armitage (2015) points out that a naive comparison between a typical disk mass, $M_{\text{disk}} \sim 5 \times 10^{-3} M_{\odot}$ and typical accretion rate $\dot{M}_{\text{disk}} \sim 10^{-8} M_{\odot} \text{ yr}^{-1}$ (Gullbring et al., 1998; Andrews et al., 2010) yields a characteristic time scale of 0.5 Myr. This is comparable to the disk lifetime estimates when considering the large uncertainties in both M_{disk} and \dot{M}_{disk} . Such an argument suggests that removal of the disk mass can be entirely accounted for by accretion.

Nonetheless, photoevaporation has also been shown to aid in the removal of material from disks (for example, Hollenbach et al., 1994) whereby high-energy radiation photodissociates or ionized molecular gas, heating it to such an extent that it becomes unbound from the disk (Ercolano et al., 2014). In addition, magneto-hydrodynamic (MHD) winds have also been shown to contribute to disk dispersion, however observations of signatures of winds are distinctly lacking (Pascucci et al., 2011; Manara et al., 2014).

1.3 Molecular Probes of Physical Conditions

The theory of planet formation is in a healthy position with numerous dynamical processes proposed to solve the issues faced in forming planets and creating a diversity of systems as observed. These efficiency, or in some cases, presence, of these processes are highly sensitive to the physical properties of the disk, such as the temperature, density and ionization structure. In order to distinguish between physical processes and explore their impact on the disk structure, better observational constraints are required.

Continuum emission, sensitive to the \sim mm sized grains, provides an unparalleled opportunity to image disks at high spatial resolution; recently Andrews et al. (2016) achieved a projected resolution of \sim 1 au revealing a rich ring structure in the TW Hya disk (see Fig. 1.2). Due to the sedimentation of larger dust-grains, mm-continuum emission will predominantly arise from the disk midplane, tracing the region where planets are forming. While providing some constraints on disk dust mass and dust temperature, due to ambiguity between dust mm opacities and dust properties and composition, it is incredibly hard to infer local physical properties from continuum alone. Despite this hurdle, the short integration times needed to detect and image a disk at these resolutions allows for large samples of disks to be studied.

Molecular line emission, on the other hand, is an excellent probe for the study of physical conditions found in protoplanetary disks. At the low temperatures expected in

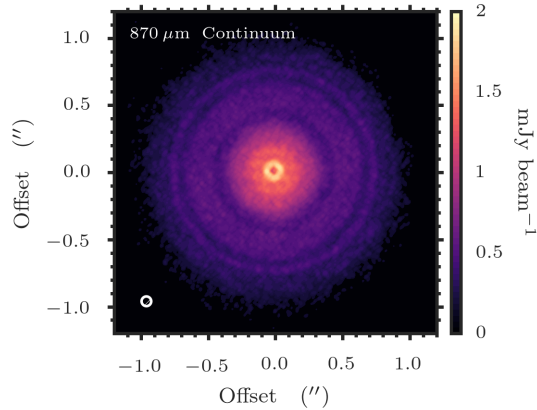


Figure 1.2 TW Hya at 870 μm from [Andrews et al. \(2016\)](#).

a disk (~ 10 to 100 K), low rotational transitions ($J \lesssim 10$) of many abundant molecules are easily excited. Observing a range of molecules provides unique possibility to study the chemical make-up of the disk, tracing distinct regions and local physical properties to which the chemistry is sensitive to. Furthermore, by spectrally resolving the emission line, key kinematical information about the disk can be extracted, providing valuable insights into the dynamical processes present. Table 1.1 shows some of the molecular tracers commonly observed in protoplanetary disks and the physical property of interest.

By using a combination of continuum and molecular line emission, huge strides have been made in the understanding of disks since the original detection of a protoplanetary disk. The first glimpse of a circumstellar disk was the observation of continuum emission centred on HL Tau ([Sargent & Beckwith, 1987](#)). Several years later, the double-peaked profile indicative of Keplerian rotation was observed in a handful of systems ([Weintraub et al., 1989](#); [Sargent & Beckwith, 1991](#); [Koerner et al., 1993](#); [Dutrey et al., 1994](#)), cementing the idea of rotating media around young stars. Today, with observatories such as the Atacama Large Millimetre Array (ALMA) and the Karl G. Jansky Very Large Array (VLA), observations constraints continue to help refine the theories of planet formation, and with the James Webb Space Telescope (JWST) in the near future and the European Extremely Large Telescope (E-ELT) under construction, the topic of planet formation is entering a golden age.

Mass

The mass of a disk has a strong impact on its evolution. For example, [Mordasini et al. \(2012\)](#) has demonstrated that the ability of a disk in creating hot-Jupiters is strongly linked to the mass of the disk, while [Manara et al. \(2016\)](#) have shown an almost linear correlation between the disk mass and the accretion rate. However, measuring the mass of a disk remains a fundamental problem in which huge amounts of observing time and theoretical efforts have been, and still are, invested in.

As continuum images were far more readily attainable than its molecular emission counterpart, initial estimates of disk gas mass scaled the mass estimates of the dust

Table 1.1 Molecular Probes of Protoplanetary Disks

MOLECULES	TRACES WHICH PHYSICAL PROPERTY
CO, ^{13}CO , C^{18} , C^{17}O	Density and Temperature
HD, CS, H_2CO	Density
NH_3 , H_2	Temperature
HCO^+ , N_2H^+ , C^+	Ionization
HCN, CN, C_2H	Photoprocesses
Complex Organic Molecules (COMS)	Surface Chemistry
DCO^+ , N_2D^+ , DCN	Deuterium Fractionation

Note: Adapted from [Henning & Semenov \(2013\)](#).

mass by 100 to account for the ISM gas-to-dust ratio of 100:1. This relied on the assumption that the continuum emission was optically thin and so provided a lower limit to the masses of disks. Following [Beckwith et al. \(1990\)](#), the mass of a disk can be estimated from:

$$\log M_{\text{disk}} = \log F_{\nu} + 2 \log d - \log(\zeta \cdot \kappa_{\nu}) - \log B_{\nu}(\langle T \rangle), \quad (1.3)$$

where ζ is the dust-to-gas ratio, κ_{ν} the dust opacity and $B_{\nu}(\langle T \rangle)$ is the Planck function at the average disk temperature. Clearly this estimate is limited as ζ , κ_{ν} and T will all strongly be a function of location. Nonetheless, many large surveys have used this relation to measure dust masses, most notably [Beckwith et al. \(1990\)](#), [Andrews & Williams \(2007\)](#) and [Andrews et al. \(2013\)](#). More recently, [Barenfeld et al. \(2016\)](#) detected 53 disks in the Upper Scorpius OB Association in dust continuum, 26 of which were additionally detected in CO. From the dust masses, the authors found a weak dependence between the dust mass and the stellar mass of $M_{\text{dust}} \propto M_{\star}^{1.67 \pm 0.37}$. This relationship is consistent with the result for the Chamaeleon I star forming region reported by [Pascucci et al. \(2016\)](#) with $M_{\text{dust}} \propto M_{\star}^{1.3-1.9}$.

With observations of molecular emission becoming more achievable, the gas content came under more scrutiny. Despite H_2 being the dominant molecule in a disk, its homonuclear structure leaves it without a permanent dipole moment and therefore non-emitting at the temperatures found in disks. Hydrogen-deuteride, HD, would provide the best probe of H_2 , however the fundamental transition at $112 \mu\text{m}$ is unable to be observed with current instrumentation. *Herschel* was able to observe 7 disks at this frequency and detected HD emission in 3 of those targets: TW Hya, DM Tau and GM Aur ([Bergin et al., 2013](#); [McClure et al., 2016](#)). From model fitting, the disks masses were found to fall between 10^{-2} and $10^{-1} M_{\odot}$, however the results require intimate knowledge of the thermal structure in order to distinguish between abundance and excitation effects.

As the second most abundant gas-phase molecule in a disk, CO acts as a reasonable proxy of H_2 with easily excited rotational transitions. Initial gas mass measurements were limited by the optical thickness of CO. [Ansdell et al. \(2016\)](#) attempted to alleviate this issue and carried out a survey of disks in the Lupus star forming region, detecting 61 disks in mm-continuum and lines of ^{13}CO and C^{18}O . Using the methodology outlined in

Williams & Best (2014), the authors converted line and continuum fluxes into measured gas and dust mass respectively, finding a gas-to-dust ratio considerably smaller than the canonical 100. Such a finding calls into question the validity of assuming a gas-to-dust ratio of 100 in disks and therefore the conversion used in Eqn. 1.3.

This discrepancy in gas-to-dust ratios can be a result of poorly constrained gas masses, dust masses or a combination of both. Isotopologue-selective dissociation has been shown to bias the mass measurement from CO isotopologue lines (Miotello et al., 2014, 2016), however the effect is not believed to be severe enough to account for the discrepancy in measured mass. Recent work has also suggested that there is a strong carbon depletion in some disks, such as TW Hya, HD 163296 and DM Tau (Schwarz et al. (2016); Kama et al. (2016b); McClure et al. (2016)), which would reduce the relative abundance of CO with respect to H₂ compared to that measured in the ISM while also pointing towards non-ISM isotopic ratios (for example, a standard ISM ¹³C / ¹²C ratio is ~ 80, while Piétu et al. (2007) argue for a lower ratio of ¹³CO / ¹²CO ~ 20 in disks). Multi-wavelength continuum observations will allow for better estimations of the dust mass, while observations of multiple carbon bearing species will help calibrate models of CO emission in measuring the gas mass.

Temperature

Understanding the temperature structure is not only essential in setting constraints for modelling the physical evolution of the disk, but also in interpreting observed emission. For instance, the mass of a disk, derived from Eqn. 1.3, is incredibly sensitive to the assumed temperature. Similarly, the intensity of line emission depends on both the excitation conditions, temperature and density, but also on the abundance of the molecule. In turn, the abundance of a molecule depends on the chemical evolution which is regulated by the thermal structure of the disk (see Section 2.2 in Chapter 2). An accurate measure of the thermal structure of a disk is therefore essential in deriving physical properties of the disk from observations.

Molecular line emission is the most appropriate tool as the observation of multiple transitions from a single species allows for an excitation analysis to be performed resulting in a temperature (Mangum & Shirley, 2016, provide a thorough tutorial of such a process). However, there are pitfalls to this method. Molecular emission traces primarily a region where the molecule is most abundant, leaving one ignorant about the remaining disk. In addition, each transition will have a different optical depth resulting in each transition a different region in the disk. In the case of a fully optically thick transition, such as the low *J* transition ¹²CO lines, the emission will only be tracing down to the $\tau \approx 1$ surface, avoiding the bulk CO reservoir altogether (see Fig. 2.8 in Chapter 2). Therefore, in order to infer a global thermal structure, several emission lines from a range of density and temperature tracers (such as those described in Table 1.1) must be observed.

It was Dartois et al. (2003) who were the first to observationally detect a vertical temperature gradient in the disk around DM Tauri, despite theoretical considerations suggesting one should be present. As with measurements of disk masses, CO isotopo-

logues were used in place of ^{12}CO because of their range of optical depths, each sensitive to different vertical regions in the disk. The authors demonstrated that a simple, vertically isothermal disk model was unable to simultaneously fit the observations without invoking exotic temperature or chemical structures. [Akiyama et al. \(2011\)](#) followed a similar approach to infer a temperature gradient in the disk of HD 163296. More recently, [Rosenfeld et al. \(2013\)](#) used the high spatial resolution of ALMA ($\theta_{\text{beam}} \approx 0.5''$) to spatially resolve the flared molecular regions of CO in HD 163296.

A less direct method has been used in several studies which aim to reproduce the spectral energy distribution (SED) and large samples of line emission for individual sources. By fitting the SED, dominated by the stellar emission and refractory component of the disk, a temperature structure can be constrained. By simultaneously calculating molecular abundances in order to account for the impact of molecular line cooling, the molecular line emission provides even stronger constraints on the gas temperature. For example, *ProDiMo* (Protoplanetary Disk Model) combines a thermo-chemical model with extensive chemistry and 2D continuum radiative transfer to model a self-consistent disk ([Woitke et al., 2009](#)). By such a procedure, disk structures can be found which are consistent with a huge range of observations⁵, from SED to molecular and atomic line emission (see also the models by [Akimkin et al., 2013](#); [Gorti et al., 2011](#)).

An excellent example of the power of such a methodology is TW Hya. As the closest protoplanetary disk to Earth, $d \approx 59 \pm 1$ pc ([Gaia Collaboration et al., 2016](#)), and viewed at a favourable near face-on orientation, $i \approx 7^\circ$ ([Qi et al., 2004](#)), there is a tremendous amount of archival data for the source. [Gorti et al. \(2011\)](#) exploited this and performed extensive modelling to constrain a temperature, density and ionization structure of TW Hya which produced emission consistent with observations from UV to mm wavelengths. This physical structure was used widely in this thesis, continuing to produce molecular emission consistent with new observations, suggesting that the thermal structure is well constrained, providing a foundation upon which predications can be made. In addition, [Kama et al. \(2016b\)](#) used the DALI code ([Bruderer et al., 2009, 2012](#); [Bruderer, 2013](#)), considered separate gas and dust distributions to explore the carbon and oxygen depletion in TW Hya by fitting a range of carbon bearing species (C, C^+ , CO and C_2H) emission. This study allowed for tight constraints to the physical structure in addition to quantifying the carbon depletion expected.

Although these models produce results which are consistent with a huge range of observations, they still rely on a modelling framework which may be flawed. Nearly edge-on disks, such as the Flying Saucer with $i \approx 90^\circ$ ([Guilloteau et al., 2016](#)), and AA Tau at $i \approx 70^\circ$ ([Andrews & Williams, 2007](#)), provide the best opportunity to directly image the vertical structure of disks and therefore constrain the global temperature and density structures. ALMA observations of these objects will provide direct evidence for the vertical structure of these disk with which the thermo-chemical codes, as mentioned above, can be calibrated with.

⁵ The final results for a range of well known sources are publicly available: <http://www-star.st-and.ac.uk/~pw31/DIANA/DIANAstandard/>.

Ionization

The ionization structure is a fundamental ingredient of a protoplanetary disk; driving both the chemical and physical evolution. Chemically, ion-neutral reactions dominate in the low temperature environments of a disk with the beginnings of chemical complexity starting with the ionization of H_2 into H_3^+ (Herbst & Klemperer, 1973; Henning & Semenov, 2013). In terms of the physical evolution, MRI requires a minimum ionization level for the gas to efficiently couple with the magnetic fields to drive the necessary turbulence. As such, many attempts have been made to infer the ionization fraction in a disk.

Chemical modelling suggests that the ionization structure is highly stratified with different ionizing sources dominating the local ionization in different regions (Aikawa & Herbst, 1999; Semenov et al., 2004): stellar and interstellar far-ultraviolet (FUV) to UV in the upper layers, stellar X-rays in the warm, molecular regions, and cosmic ray particles (CRP) and the decay of short lived radionuclides (SLRN) in the midplane. However, as there is a shortfall in accurately measured stellar spectra, deriving an ionization structure will ultimately be limited by the prior knowledge of the impinging radiation.

Nonetheless, by self-consistently modelling a disk and observing key molecular species, the ionisation structure can be constrained. The molecular ion content of disks is dominated by H_3^+ , HCO^+ and N_2H^+ (including their deuterated isotopologues) and so observations would provide tight constraints of the ionization structure (for example, Dutrey et al., 2007; Teague et al., 2015; Cleaves et al., 2015a). The first of these detected in a disk was HCO^+ in the disks around GG Tau and DM Tau (Dutrey et al., 1997), with the deuterated isotopologue DCO^+ being detected later in TW Hya (van Dishoeck et al., 2003). N_2H^+ and N_2D^+ have also been detected (Dutrey et al., 2007; Huang & Öberg, 2015), however the emission is much weaker due to the considerably lower abundances than HCO^+ .

Extensive analysis of the sources of ionization in a protoplanetary disks has been carried out by Cleaves et al. (2013a,b, 2014a, 2015b) who also make use of new ALMA data. The authors advocate for a reduced CRP ionization flux of $\zeta_{\text{H}_2} \lesssim 10^{-19} \text{ s}^{-1}$, almost 2 orders of magnitudes lower than for the ISM, due to the shielding provided by the strong stellar winds. Furthermore, the authors demonstrate the X-rays provide a lasting effect on the chemistry of a disk, proposing the use of multiple molecular ions to provide constraints.

More sensitive observations of less abundance ions in conjunction with simultaneous monitoring of the host stars in FUV, UV and X-ray wavelengths provides the best opportunity to understand the ionization structure of disks. The increased sensitivity of ALMA is opening up the possibility of providing tight constraints on the electron fraction in disks, although limitations in observing the midplane in molecular ion line emission will ultimately set how well the ionization fraction can be understood.

Dynamics

Although the ionization fraction of the disk remains illusive, bringing into question the activeness of MRI, signatures of highly dynamic disks are frequently observed: active accretion onto the central star and stark sub-structures observed in both thermal continuum emission and scattered light. These pieces of evidence point to a distinctly non-quiescent disk permeated by turbulent motions.

Several attempts have been made to measure the suspected turbulence through the broadening of emission lines,

$$\Delta V = \sqrt{v_{\text{turb}}^2 + \frac{2kT_{\text{kin}}}{\mu m_p}}, \quad (1.4)$$

where v_{turb} is the turbulent velocity component, μ is the molecular weight of the emitting molecule and m_p is the proton mass. Allowing for a radial gradient in v_{turb} and using a more simplistic, vertically isothermal disk model, [Dartois et al. \(2003\)](#) and [Piétu et al. \(2007\)](#) measured turbulent broadening profiles on the order of $\lesssim 100$ to 200 m s^{-1} for the disks around DM Tau, MWC 480 and LkCa 15 with observations from the Plateau de Bure Interferometer (PdBI). [Guilloteau et al. \(2012\)](#) used CS emission in DM Tau in place of CO in an attempt to minimise the thermal broadening component ($\mu_{\text{CS}} = 44$, compared to $\mu_{\text{CO}} = 28$), however found similar values as previous measurements. [Hughes et al. \(2011\)](#) attempted to fit high spectral resolution Smithsonian Millimetre Array (SMA) observations of CO in TW Hya and HD 163296 with a model containing a variable turbulent width. The authors found an upper limit of $v_{\text{turb}} \lesssim 40 \text{ m s}^{-1}$ for TW Hya and $v_{\text{turb}} \sim 300 \text{ m s}^{-1}$ for HD 163296. Although these models included a full chemical network and a realistic thermal structure, a globally homogeneous value for v_{turb} would limit the fit as most instabilities produce large gradients in v_{turb} , both radially and vertically.

The most recent work in this context (except of [Teague et al., 2016](#), presented in Chapter 5) has been that of [Flaherty et al. \(2015\)](#) who have used multiple CO transitions observed with ALMA to place very tight constraints on v_{turb} in HD 163296. The results are in stark contrast with those of [Hughes et al. \(2011\)](#), finding $v_{\text{turb}} \lesssim 0.03 c_s$, where c_s is the local soundspeed. The authors chose to parametrise v_{turb} as a function of c_s rather than in absolute units as the Mach number of turbulence is predicted to be near constant across the radius of the disk ([Flock et al., 2015](#)), however impose a parametric temperature structure which could confuse interpretation.

In comparison to the turbulent width, little work has been done in regard to the bulk motion of the gas; little more than cursory checks are typically made to confirm that an object is in near Keplerian rotation. The rotation profile can be used to derive a dynamical mass of the central star (e.g. [Simon et al., 2000](#)), however these work focus on the stellar component rather than the disk. Nonetheless, with modern instrumentation allowing for considerable higher spectral resolutions ($\approx 30 \text{ m s}^{-1}$ are routinely achieved), analyses of the bulk gas motion have started to show their potential.

For instance, [Rosenfeld et al. \(2012\)](#) demonstrated that the high-velocity channels of CO emission observed with ALMA was inconsistent with a model with a typical ther-

mal structure. The authors advocated for a warp in the disk, such that the inclination changes from $i \approx 8^\circ$ at 5 au, increasing to $i \approx 5^\circ$ at 100 au, a finding consistent with the azimuthal dependence observed in scattered light by NICMOS on the Hubble Space Telescope (HST) (Debes et al., 2013). A similar skewed rotation profile observed in the transition disk HD 142527 from CO emission was interpreted as radial inflow of gas onto the central star (Casassus et al., 2013), although Rosenfeld et al. (2013) demonstrated that it is impossible to distinguish between a warped inner disk and radial in-fall onto the star. Supplementary observations are necessary in order to distinguish between scenarios.

Molecular Inventory

In addition to studying the physics of planet formation, the chemistry is equally important. As the planets accrete material from their surroundings, the chemical make-up of a planetary atmosphere should therefore be indicative of their formation location in the disk. Indeed, with an ever increasing sample size of exoplanets thanks to the likes of NASA's mission *Kepler*, abundance retrieval methods have been developed and refined (for a review, see Crossfield, 2015). These findings suggest that the [C] / [O] ratio in the atmosphere are a key diagnostic in this area, sensitive to the radial position of formation (Öberg et al., 2011a; Walsh et al., 2015). Furthermore, these conclusions are bolstered with the abundance measurements in comets with missions, such as the European Space Agency (ESA) *Rosetta* mission, which should be tracing the molecular abundances in the planet forming midplanes of protoplanetary disks (Drozdovskaya et al., 2016).

In addition, population syntheses are now making predictions for the bulk properties of large samples of exoplanets given contemporary knowledge of planet formation and the chemistry in protoplanetary disks (for example, Ida & Lin, 2004; Mordasini et al., 2009; Cridland et al., 2016). It is therefore essential to calibrate chemical models of protoplanetary disks in order to make fair comparisons between models and observations.

A majority of the molecules detected in protoplanetary disks are simple, di- or tri-atomic molecules, similar to those observed in the ISM and star forming regions (Caselli & Ceccarelli, 2012; Henning & Semenov, 2013). With the large collecting area of ALMA's 50 dishes, less abundant species are starting to be detected, such as the elusive CH_3OH (Walsh et al., 2016). With an ever larger repertoire of observed emission (both atomic and molecular line emission as well as continuum), models of specific protoplanetary disks will become ever more accurate (see the discussion above regarding the temperature structure).

1.4 Structure of this Thesis

With the huge influx of detailed observations of protoplanetary disks from a range of observatories and theoretic models including ever more complex physics at smaller and smaller scales, our understanding of planet formation is coming under ever more scrutiny.

This thesis aims to use a combination of sub-mm interferometric observations with chemical and physical modelling to answer questions related to planet formation:

1. **Is the level of deuteration an accurate ‘chemical clock’ for protoplanetary disks?** Deuterated molecules may provide an opportunity to date the age of a protoplanetary disk, thereby creating an evolutionary sequence of protoplanetary disks and allow for comparisons with values measured for Solar System bodies.
2. **Can observations of key molecular ions help constrain the ionization structure of a disk?** Knowledge of the ionisation structure is essential for modelling both the physical evolution of the disk if the MRI is present and the chemical evolution.
3. **Is it possible to directly constrain the level of turbulence in a disk from observations?** Constraints on the level of turbulence present in protoplanetary disks are distinctly lacking and thus far are all strongly model dependent. The high angular and spectral resolutions afforded by ALMA promise the most accurate constraints on turbulence to date.
4. **Can molecular emission be used to help trace surface density perturbation in disks?** A connection must be made between the features observed in scattered light and thermal continuum emission by tracing the intervening, molecular rich gas.

The following two chapters, Chapters 2 and 3, I will introduce and review the modelling and observational techniques frequently used in this pursuit with particular attention paid to those used in the work presented here. Chapter 2 looks at the numerical models commonly used in the literature and compares their strengths in terms of analysing observations and making predictions, while Chapter 3 discusses the techniques used in extracting physical properties from a range of types of observations.

Chapter 4 uses a combination of PdBI observations of the key molecular ions HCO^+ and DCO^+ in DM Tauri and extensive chemical modelling to constrain the ionization structure and the thermal history through the efficiency of deuterium fractionation. It is based on the work [Teague et al. \(2015\)](#) published in *Astronomy & Astrophysics*.

Chapter 5 uses ALMA observations of CO, CN and CS emission to provide the first spatially resolved measurement of turbulent linewidths in a protoplanetary disk, TW Hydrae. The study focusses on the methodology of measuring turbulence and the limitations involved which have important implications for all future work aimed at studying turbulence in disks. The chapter is based on [Teague et al. \(2016\)](#), published in *Astronomy & Astrophysics*.

In Chapter 6, the same observational data of Chapter 5 is analysed, displaying features consistent with a surface density depression, making it the first detection of a surface density perturbation with molecular emission. Modelling allows for a measure of the depth to be estimated and compared with previously published models which invoked a

surface density perturbation to explain the similar dip feature seen in scattered light. This Chapter is based on work submitted to *The Astrophysical Journal*.

A summary of the findings will be made in Chapter 7, with a discussion of the future work which can use the findings presented in Chapters 4, 5 and 6 as a springboard.

Modelling a Protoplanetary Disk

To compare one's theoretical understanding of protoplanetary disks to observations requires first the building a model of what one would expect to observe. For the case of protoplanetary disks, this is a multi-step process. Starting from a physical structure (temperature and density) of the disk, chemical modelling calculates a set of atomic and molecular abundances as a function of position in the disk. These are then, in turn, used to run radiative transfer models which first calculates the excitation of the particular species before producing images of the observed emission through ray-tracing. This Chapter will briefly review the current methods used in modelling protoplanetary disks with particular attention paid to those used in the rest of the thesis.

2.1 Physical Models

The evolution of a protoplanetary disk is dictated by the temperature and density structures. Acting in tandem, these parameters will dictate which instabilities are present and which are suppressed, setting the physical and chemical evolution of the disk and the efficiency of the disk in forming planets. As such, it is essential that the numerical description of these parameters are as accurate as possible so as not to introduce errors with each additional modelling step.

Symmetry is heavily exploited in the study of protoplanetary disks with a view to speeding computation. Disks are generally considered to be azimuthally symmetric and mirrored in the (x, y) plane¹. Thus, one needs to only consider the cylindrical coordinates (r, z) , or polar coordinates, (r, θ) . In the majority of this thesis, I will work in cylindrical coordinates unless stated otherwise.

Surface Density

The foundation of nearly all models is the surface density of the disk, the mass as a function of radius. Following the likes of [Lynden-Bell & Pringle \(1974\)](#) and [Hartmann et al.](#)

¹ Aside from some disks displaying local perturbation such as spiral arms in scattered light, disks are predominantly symmetric at current resolutions.

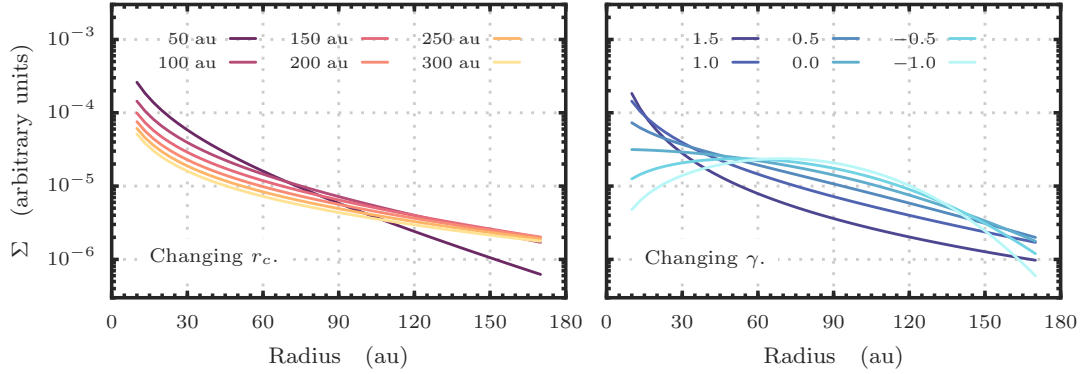


Figure 2.1 Surface density prescriptions using Eqn. 2.1. The left panel shows the effect of changing r_c with $\gamma = 1$ while the right shows changing γ with r_c fixed at 100 au with an equal gas mass for all surface densities.

(1998), assuming a time-independent viscosity which scales radially as $\nu \propto r^\gamma$, yields,

$$\Sigma = \frac{M_{\text{gas}}(2-\gamma)}{2\pi r_c^2} \cdot \left(\frac{r}{r_c}\right)^{-\gamma} \exp\left[-\left(\frac{r}{r_c}\right)^{2-\gamma}\right], \quad (2.1)$$

where r_c is a characteristic radius and M_{gas} is the gas mass of the disk. Figure 2.1 demonstrates the effects of changing r_c in the left panel, and changing γ in the right. Typically, gas dominated disks have $\gamma \approx 1$ and r_c ranging between 10s and 100s of au.

Temperature Structure

Beyond an isothermal disk, the simplest form of thermal structure is a vertically isothermal disk where the gas (and dust) temperature is a power-law, so at radial position r :

$$T(r) = T_c \left(\frac{r}{r_c}\right)^{-q} \quad (2.2)$$

where T_c is the temperature at r_c and q describes the fall off of temperature, with typical values of $q \approx 0.4 - 0.5^2$.

This form, however, fails to capture the vertical gradients in temperature expected, and observed, in disks. Determining a temperature structure observationally is a challenge, although some parametric forms of temperature structure have yielded reasonable success in reproducing observations (Chiang & Goldreich, 1997; Dartois et al., 2003; Rosenfeld et al., 2013). These forms consider two layers, the midplane and atmosphere, which each have their own power-law description, as in Eqn. 2.2, and are connected through a smoothly varying function. A commonly used form is,

$$T(r, z) = \begin{cases} T_{\text{atm}}(r) + (T_{\text{mid}}(r) - T_{\text{atm}}(r)) \cdot \left(\sin \frac{\pi z}{2z_q}\right)^{2\delta} & \text{if } z < z_q, \\ T_{\text{atm}}(r) & \text{if } z \geq z_q, \end{cases} \quad (2.3)$$

² A general argument for this behaviour is that the heating is dominated by stellar radiation which drops off as $r^{-0.5}$. A more thorough argument is presented in Pringle (1981), which requires conservation of mass in the disk while accretion is present.

where $T_{\text{mid}}(r)$ and $T_{\text{atm}}(r)$ are power-law profiles, z_q describes the height of the disk ‘atmosphere’ and δ sets the vertical temperature gradient, typically with $\delta = 1$. A common prescription for z_q is $4H_p$ where H_p is the pressure scale height,

$$H_p = \sqrt{\frac{k T_{\text{mid}}(r) r^3}{\mu m_p G M_\star}}. \quad (2.4)$$

Currently there are no observational constraints on the functional form of the connection between the midplane and atmospheric layer, however future observations of nearby edge of disks will allow for a much better understanding.

A third possibility is to use a thermo-chemical model which iteratively solves for the temperature and density structure of the disk by considering the balance of heating and cooling processes. These models include chemical evolution, to correctly account for the line cooling, and grain evolution, which will affect the opacity of the disk to the incident stellar radiation. Such models include that of, [Jonkheid et al. \(2004\)](#), [Gorti et al. \(2011\)](#), which was used extensively in this thesis, ANDES ([Akimkin et al., 2013](#)), DALI ([Bruderer et al., 2012](#)) and ProDiMo ([Woitke et al., 2009](#)).

Figure 2.2 compares these temperature structures in the right hand column. The top panel shows the thermal structure of TW Hya as modelled by [Gorti et al. \(2011\)](#), which has been used extensively in Chapters 5 and 6. The central and bottom panels show two examples using the parametric form of Eqns. 2.3 and 2.2 respectively, where the parameters have been chosen to qualitatively recover the temperature structure of the thermo-chemical model. A temperature structure from a thermochemical model is considerably more complex than can be captured with a parametric model with non-monotonically increasing vertical gradients and includes the possibility of treating gas and dust temperatures separately in order to properly recover the decoupling expected in the upper atmospheres of the disk. However, thermochemical modelling takes considerably more time to calculate and a simple parametric form. Depending on the application, a parametric version may suffice as they qualitatively recover the global structure of the disk but cannot recover the thin region where a molecule is present in the case of a single transition.

Volume Density Structure

Protoplanetary disks are believed to be in hydrostatic equilibrium. Therefore, with a given thermal structure, the density structure must satisfy,

$$\frac{1}{\rho_{\text{gas}}} = \frac{\partial P}{\partial z} = \frac{\partial}{\partial z} \left(\frac{GM_\star}{\sqrt{r^2 + z^2}} \right). \quad (2.5)$$

Then, with a given surface density, we can ‘inflate’ the disk to provide a volume density. Therefore, assuming that the disk is an ideal gas, $P = \rho_{\text{gas}} \cdot c_s^2$, the vertical structure is given by,

$$-\frac{\partial \ln \rho_{\text{gas}}}{\partial z} = \frac{\partial \ln T_{\text{gas}}}{\partial z} + \frac{1}{c_s^2} \left[\frac{GM_\star z}{(r^2 + z^2)^{3/2}} \right]. \quad (2.6)$$

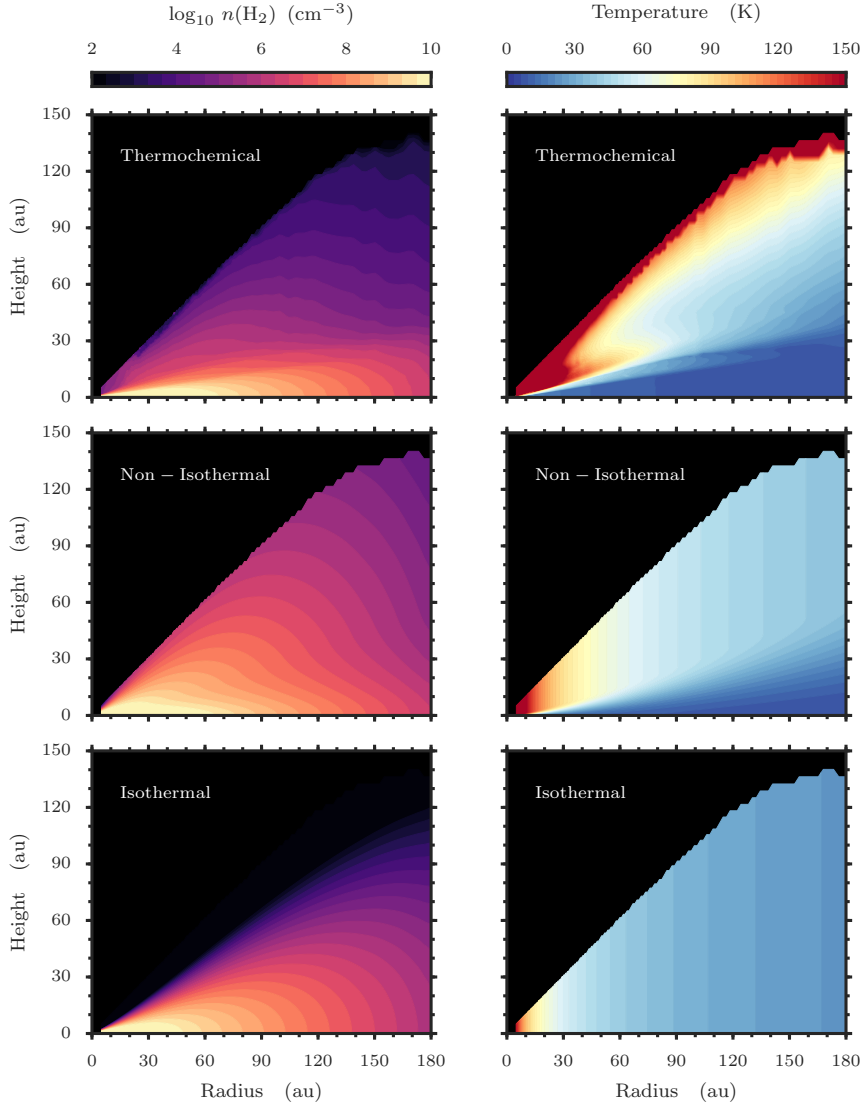


Figure 2.2 Comparison of commonly used density and temperature structures. The left column shows $n(\text{H}_2)$ while the right column shows T_{gas} . The top panel shows a thermochemical model (Gorti et al., 2011). A two region parametric approximation of the temperature structure, as described by Eqn. 2.3 with the values $T_{\text{mid,c}} = 25.8$ K, $T_{\text{atm,c}} = 150$ K, $q_{\text{mid}} = 0.49$, $q_{\text{atm}} = 0.48$, $\delta = 1$, $z_q = 4H_p$, and $r_c = 10$ au, is shown in the middle row. The bottom row shows the most basic structure, a vertically isothermal disk described by Eqn. 2.2 with parameters $T_c = 100$ K, $q = 0.5$ and $r_c = 10$ au. All models have the same surface density.

For a vertically isothermal disk, the resulting density structure is one that falls off with a Gaussian profile:

$$\rho_{\text{gas}}(r, z) = \frac{\Sigma_{\text{gas}}(r)}{\sqrt{2\pi}H_p} \exp\left(-\frac{z^2}{2H_p^2}\right), \quad (2.7)$$

however for the non-isothermal case (and thermochemical case) this has to be solved iteratively³.

The left column of Figure 2.2 compares the resulting $n(\text{H}_2)$ structures, arising from the corresponding temperature structures in the right hand column, normalised such they they all have the save surface density profile. Despite the equivalent surface densities, the volume densities between models can vary strongly, particularly in terms of flaring with the simple isothermal disk being distinctly less extended vertically than the non-isothermal and thermochemical cases. Although the midplane densities are comparable, in the molecular region densities between the models can differ by over two orders of magnitudes which will have a large effect on both the chemistry and excitation of molecular lines.

2.2 Chemical Models

Chemical models, in general, follow the same principles, however the specifics of their methodology may vary. As such, this Section will focus on the broad picture of chemical modelling with details of the treatment provided by ALCHEMIC (Semenov et al., 2010; Semenov & Wiebe, 2011), which was used in this thesis.

To calculate the local abundances of molecules and atoms, chemical models solve the equations of chemical kinetics:

$$\frac{dn_i}{dt} = \sum_{j,k} k_{j,k} n_j n_k - n_i \sum_{i \neq j} k_j n_j + k_i^{\text{des}} n_i^s - k_i^{\text{acc}} n_i, \quad (2.8)$$

$$\frac{dn_i^s}{dt} = \sum_{j,k} k_{j,k}^s n_j^s n_k^s - n_i^s \sum_{i \neq j} k_j^s n_j^s - k_i^{\text{des}} n_i^s + k_i^{\text{acc}} n_i, \quad (2.9)$$

where n_i and n_j^s are the gas and surface concentrations of species i respectively and k , k^{acc} and k^{des} are the reaction rates for gas-phase reactions, accretion and desorption respectively. Chemical networks contain all the reaction rates needed for a large amount of molecular species, including isotopologues (for example, C^{18}O , DCO^+) and isomers (for example, HCN , HOC^+) and contain on the order of 1000 species and up to 100,000 reactions. The Kinetic Database for Astrochemistry (KIDA)⁴ (Wakelam et al., 2012) contains a repository of up-to-date reaction rates which have been ratified by the astrochemical community for use in chemical modelling and allows for others to reproduce results with their own chemical code. Another commonly used repository is the University of Manchester Institute of Science and Technology (UMIST) database⁵. A more comprehensive

³ As noted by Rosenfeld et al. (2013), Eqn. 2.6 fails to include self-gravity which will alter the structure for more massive disks, typically Herbig Ae/Be disks, however for lower mass T Tauri stars, this is negligible.

⁴ <http://kida.obs.u-bordeaux1.fr/>

⁵ <http://udfa.jmarkwick.net/>

overview of the chemical networks used in specific projects for this thesis can be found in the appropriate chapters: 4 and 6.

Gas Phase Chemistry

Gas-phase reactions are the dominant type of reactions in astrophysical contexts and are typically characterised with rates following the Arrhenius representation,

$$k(T) = \alpha \left(\frac{T}{300} \right)^\beta \exp\left(-\frac{\gamma}{T}\right), \quad (2.10)$$

where we identify α as the room temperature reaction rate; β , its temperature dependence and γ the activation barrier in K. With most neutral-neutral reactions requiring activation energy, $\gamma > 0$ K, gas-phase chemistry in a protoplanetary disk is dominated by the predominantly barrier-less ion-neutral reactions (and neutral-neutral reactions between open shell species and/or radicals). The charge-quadrupole interaction between the reactants allows them to approach each other from farther distances, overcoming this barrier. Conversely, neutral-neutral reactions and three body interactions, while present in a disk, occur on much longer time-scales and are less important for the global chemistry.

The efficient of ion-neutral reactions depends on the ionisation structure of the disk. In protoplanetary disks three ionising energy regimes are important: UV to FUV wavelengths, X-rays and CRP. With the physical structure provided, *ALCHEMIC* calculates the local ionisation rate, ζ , for each ionization source. An ionizing rate must be assumed for each source, which is then attenuated along the line of sight to the point in the disk. UV and FUV radiation is taken to be from both stellar and interstellar sources and is attenuated by a factor of $A_v = N(\text{H}) / 1.59 \times 10^{21}$, where $N(\text{H})$ is the line of sight hydrogen column density in cm^{-2} along the line of sight. X-rays are treated as in [Glassgold et al. \(1997a,b\)](#), where the source is considered to be $\approx 10 R_\odot$ above the central star and, like UV radiation, attenuated proportionally to the line of sight hydrogen column density. Short lived radio nuclides (SLRN), consisting primarily of ^{26}Al , ^{60}Fe and ^{41}Ca , are assumed to exist homogeneously within the disk producing a constant ionization rate. [Cleeves et al. \(2013b\)](#) explored a more thorough treatment of SLRNs, but found only a weak dependence of ionization rate with height above the midplane, where the majority of SLRNs are believed to exist, suggesting that a homogeneous ionization value is a reasonable approximation. Finally, CRP are taken to to penetrate the disk vertically from both sides ($\pm z$), and again are attenuated proportional to the column density of gas they travel through with a cross section proportional to the energy of the particle,

$$\zeta_{\text{CR}} = \frac{\zeta_0}{2} \left(\exp\left[-\frac{\Sigma_1(z, r)}{100}\right] + \exp\left[-\frac{\Sigma_2(z, r)}{100}\right] \right), \quad (2.11)$$

where $\zeta_0 = 1.3 \times 10^{-17} \text{ s}^{-1}$ is the unattenuated ionization rate from cosmic rays and $\Sigma_1(z, r)$ and $\Sigma_2(z, r)$ are the column densities above and below the point (r, z) respectively. Thus higher energy particles travel further through the disk. This treatment results in

three distinct regions in the disk where different chemical processes dominate: the neutral midplane, a partially ionized intermediate layer and a highly ionized atmosphere (Aikawa & Herbst, 1999; Semenov et al., 2004).

It is important to note that this lacks proper treatment of Lyman- α photons ($\lambda \approx 1215 \text{ \AA}$) which can contribute up to 20% of the total FUV luminosity of a T Tauri star (Bethell & Bergin, 2011). This energy range of photons is hugely important in the photodissociation of molecules such as HCN, H₂O and H₂CO (Bergin et al., 2003; van Dishoeck et al., 2006), while others, such as HCO⁺ and CN, are insensitive. Bethell & Bergin (2011) showed that a full Monte-Carlo Markov Chain (MCMC) treatment of the radiative transfer of Ly α photons results in a local deviation in the Ly α / FUV ratio relative to the stellar ratio, particularly in the midplane. This discrepancy leads to an underestimation of the FUV flux and hence abundances of photosensitive species which must be considered in analyses.

Gas - Grain Interactions

The interplay between the volatile and refractory components is important in the context of protoplanetary disks. Not only does the freeze-out of volatile species result in depletions of certain species (for example, CO is believed to be severely depleted in TW Hya, e.g. Schwarz et al., 2016; Kama et al., 2016b), but grains can also act as a catalyst providing the activation energy for the formation of molecules, for example the hydrogenation of CO ice to create H₂CO and CH₃OH (Loomis et al., 2015).

In ALCHEMIC the grains are treated as simple spheres with a density representative of amorphous silicates, $\rho_{\text{dust}} = 3 \text{ g cm}^{-3}$. As assuming a grain-size population is a considerably more complex problem, each cell has an effective grain-size which results in an equal grain surface area given by a single sized population (see, for example, Akimkin et al., 2013) with 1.5×10^{15} surface sites cm^{-2} . ALCHEMIC has the ability to consider three independent grain sizes, however this option was not used for the projects in this thesis. Gas-phase neutral molecules physisorb through van der Waals forces onto the grains with a 100% probability, however H₂, HD, D₂ and molecular ions do not interact. Desorption can occur through either thermal desorption, or through through an impact with a CRP which heats the molecule past the thermal desorption energy. In addition, electrons can stick to neutral grains, forming a negatively charged grain with which atomic ions can radiatively recombine. Photoelectric heating is not included.

Surface Chemistry

Surface chemistry is calculated assuming the standard rate equation, Eqn. 2.9, which is justified in the cool, dense regions found in a protoplanetary disk. Surface species move around the grains through thermal hopping. Surface recombination proceeds through the Langmuir-Hinshelwood mechanism (Hasegawa et al., 1992), with excess energy immediately absorbed by the grain, Upon a surface recombination, 1% of products are assumed to leave the grain immediately. Hydrogen tunneling through reaction barriers is allowed.

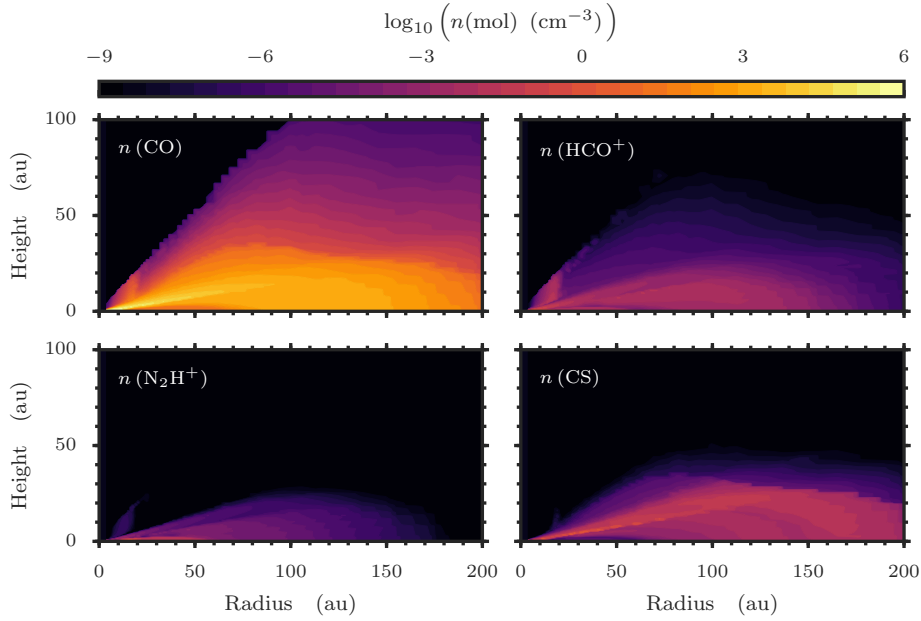


Figure 2.3 Examples of the chemical model outputs, showing $n(\text{CO})$, $n(\text{HCO}^+)$, $n(\text{CS})$ and $n(\text{N}_2\text{H}^+)$ in a clockwise fashion from the top left. All panels have the same colour scaling to demonstrate the vast variety of abundance structures.

As there are few molecules which have both diffusion and desorption energies calculated, a default $T_{\text{diff}}/T_{\text{des}}$ ratio of 0.4 – 0.77 is considered (Ruffle & Herbst, 2000).

Running a Model

Initial conditions are taken from a 0D model of a molecular cloud, indicative of what one would expect to be present at the birth of a protoplanetary disks. A standard ‘TMC-1’ like model uses a temperature of 10 K, $n(\text{H}) = 2 \times 10^4$ and $A_v = 10$ mag. The resulting abundances are dominated by H_2 and C, N and O bearing simple molecular species. A more detailed example can be found in Tables 4.3 and 4.4 in Chapter 4.

The chemical model is run for an amount of time representative of the lifetime of a disk: 1 – 5 Myrs. Over this period the physical structure of the disk does not change which, although unrealistic, allows for the chemistry to reach a chemical steady state. The model produces snapshots at various time steps throughout the simulated disk life time. Molecular abundances as a function of (r, z) throughout the disk are the output of ALCHEMIC. Figure 2.3 shows examples of four molecules distributions assuming the physical model of Gorti et al. (2011), as described in the previous section.

Parametric Chemistry

Calculating a full chemical model takes a non-negligible amount of time. As with the physical structure, it can be advantageous to find a parametrisation of the chemistry which allows for fast calculation.

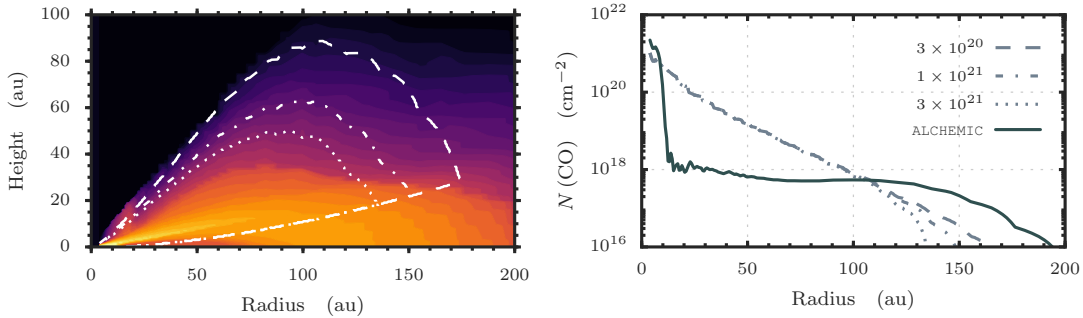


Figure 2.4 CO distributions are shown left. The coloured contours are equal to that in Fig. 2.3 for CO. The white lines show the regions where CO is in the gas-phase according for Eqn. 2.12 assuming $T_{\text{freeze}} = 20$ K and $N_{\text{diss}} = 3 \times 10^{20}$, 10^{21} and 3×10^{21} $\text{H}_2 \text{ cm}^{-2}$ for dashed, dash-dotted and dotted lines respectively. $x_{\text{gas}}(\text{CO})$ and $x_{\text{ice}}(\text{CO})$ were taken to be 3×10^{-5} and 3×10^{-10} in order to conserve the total CO mass in the model with respect to the full chemical model. The right hand panel compares the column densities for the four CO distributions.

One of the most commonly observed molecular species is CO, owing to its large abundance and easily excited rotational transitions which result in bright emission lines. Furthermore, the chemistry of CO is relatively simple with a disk-wide relative abundance⁶ with respect to H_2 of $x(\text{CO}) = n(\text{CO})/n(\text{H}_2) \approx 10^{-4}$. The distribution of CO is almost solely dictated by the depletion of it from the gas phase as CO is produced in abundance. CO can be easily photodissociated by FUV radiation. As this requires the discrete absorption of a line, CO can benefit from self-shielding and mutual-shielding with sufficiently large columns of CO and H_2 , given by N_{diss} . Additionally CO can freeze out at temperatures below T_{freeze} . The exact temperature depends on a range of variables, notably the grain surface, whether it is a raw surface or already contains a mantle of ice, and if the latter, what the composition is of the ice⁷.

As the CO distribution is readily described by three parameters, $x(\text{CO})$, N_{diss} and T_{freeze} , CO chemistry has been included in some parametric models, most notably Qi et al. (2011, 2013, 2015) and Williams & Best (2014). In these $x(\text{CO})$ is described by:

$$x_{\text{CO}}(r, z) = \begin{cases} x_{\text{gas}}(\text{CO}) & \text{if } T(r, z) > T_{\text{freeze}} \text{ and } N(r, z) > N_{\text{diss}}, \\ x_{\text{ice}}(\text{CO}) & \text{otherwise,} \end{cases} \quad (2.12)$$

with $x_{\text{gas}}(\text{CO})$ and $x_{\text{ice}}(\text{CO})$ being typically $\sim 10^{-4}$ and $x_{\text{gas}}(\text{CO}) \times 10^{-5}$ respectively and $N_{\text{diss}} = 10^{21} \text{ cm}^{-2}$ and N being calculated from the top of the disk, vertically downwards.

Figure 2.4 compares the CO distribution for a full chemical model with a thermochemical disk structure to that from a parametric representation with varying values of N_{diss} . Changes in T_{freeze} make little difference in this case as the vertical temperature gradient

⁶ The exact value of this is a topic of much debate. Several groups argue for a much lower value of $x(\text{CO}) \sim 10^{-6}$, invoking a depletion of carbon in the outer disk (Favre et al., 2013; Reboussin et al., 2015; Bergin et al., 2016), while others argue for a depletion in $n(\text{H}_2)$ instead (Ansdell et al., 2016).

⁷ Observational campaigns have aimed to measure the exact temperature, but find T_{freeze} between 17 and 25 K for TW Hya and HD 163296 (Qi et al., 2011, 2013, 2015; Schwarz et al., 2016). Laboratory studies have found a range of desorption energies consistent with this range for a range of ice-mantle compositions.

where $T \approx 20$ K is incredibly strong. As in Section 2.1, the parametric structure provides a qualitatively good fit to the chemical model in a fraction of the calculation time and has been used successfully in several studies of disks (e.g. [Rosenfeld et al., 2013](#); [Flaherty et al., 2015](#), in addition to the aforementioned studies). However, parametric representation is only acceptable for fast-evolving simple species which chemically proceeds entirely through gas-phase processes, and which hence can attain a chemical steady state. More complex molecules at least partly produced on grains cannot be treated in similar manner.

2.3 Radiative Transfer

An important step in making observational predictions from the chemical model is to run radiative transfer. This involves calculating the excitation of the molecule of interest, as well as ray tracing the emission to produce images which can be compared with observations. Correct molecular excitation is important in the study of molecular line emission as the line emission that is observed can emanate from different regions than would be expected by taking an abundance weighted value, leading one to incorrectly infer the disk physical structure. Unfortunately, however, this is ultimately limited by the accuracy of the available collisional rates for the molecule of study.

In this section I will first briefly discuss the radiative transfer problem following [Rybicki & Lightman \(1979\)](#) and [Kamp \(2015\)](#) before discussing the freely available⁸, non-local thermodynamic equilibrium (non-LTE) code LIME ([Brinch & Hogerheijde, 2010](#)), which has been used extensively throughout this thesis for the radiative transfer (see Chapters 5 and 6).

The Radiative Transfer Equation

The radiative transfer equation describes the change in intensity I_ν along a path s ,

$$\frac{dI_\nu(s)}{ds} = j_\nu(s) - \alpha_\nu(s) \cdot I_\nu(s) \quad (2.13)$$

where j_ν is the emissivity and α_ν is the absorption coefficient. Thus, the intensity observed at some point s_2 , is just the integral of Eqn 2.13 along the ray:

$$I_\nu(s_2) = I_\nu(s_1) \cdot e^{-\tau_\nu(s_1, s_2)} + \int_{s_1}^{s_2} j_\nu(s) \cdot e^{-\tau_\nu(s, s_2)} ds, \quad (2.14)$$

with the optical depth defined as,

$$\tau_\nu(s_1, s_2) = \int_{s_1}^{s_2} \alpha_\nu(s) ds. \quad (2.15)$$

Defining the source function as $S_\nu = j_\nu / \alpha_\nu$, we can then rewrite Eqn. 2.13 as,

$$\frac{dI_\nu(s)}{d\tau_\nu} = S_\nu(s) - I_\nu(s). \quad (2.16)$$

⁸ <https://github.com/lime-rt/lime>

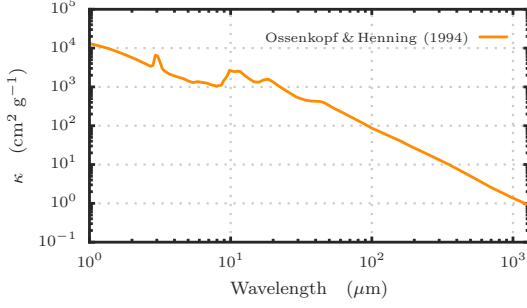


Figure 2.5 Example of the dust opacities used in radiative transfer models.

In the case of local thermodynamic equilibrium (LTE), S_ν is simply the Planck function: $S_\nu = B_\nu(T)$. A more realistic scenario, however, is when the source function is a combination of both line and continuum effects such that,

$$S_\nu = \frac{j_\nu^{\text{dust}} + j_\nu^{\text{line}} \phi_\nu}{\alpha_\nu^{\text{dust}} + \alpha_\nu^{\text{line}} \phi_\nu}, \quad (2.17)$$

where ϕ_ν is the line profile function, normalised such that $\int_{-\infty}^{\infty} \phi_\nu d\nu = 1$. The dust emission is a combination of absorption and scattering,

$$j_\nu^{\text{dust}} = \alpha_\nu^{\text{dust,abs}} B_\nu(T_{\text{dust}}) + \alpha_\nu^{\text{dust,sca}} J_\nu, \quad (2.18)$$

where $J_\nu = \frac{1}{4\pi} \int_{\Omega} I_\nu(s, \mathbf{n}) d\Omega$ and is the local mean intensity assuming isotropic scattering. In the sub-mm regime, $\alpha_\nu^{\text{dust,sca}} \ll 1$, so the second term can be safely ignored. The absorption is dictated by the dust opacity, $\kappa_\nu = \alpha_\nu^{\text{dust,abs}} / \rho_{\text{dust}}$. Dust opacities depend on the dust size distribution, mineralogy and shape. [Ossenkopf & Henning \(1994\)](#) provide a tabulated set of opacities calculated for a typical ISM grain composition, as shown in Fig. 2.5. Mie theory allows one to calculate a more specific set of dust opacities given more exact knowledge of the grain size distribution and composition, however as this is an extensive field, the reader is referred to [Bohren & Huffman \(1998\)](#).

For line emission, we consider a single transition system where a molecule moves from energy level i to energy level j , producing a photon of frequency ν . In this system,

$$j_{ij} = \frac{h\nu_{ij}}{4\pi} n_i A_{ij} \phi_{ij}, \quad (2.19)$$

where the line superscript has been dropped for brevity, n_i is the level population of energy level i and A_{ij} is the Einstein A coefficient for the spontaneous emission of the transition. The absorption for the transition is given by,

$$\alpha_{ij} = \frac{h\nu_{ij}}{4\pi} (n_j B_{ji} - n_i B_{ij}) \phi_{ij}, \quad (2.20)$$

which contains both terms for absorption, B_{ji} and stimulated emission, B_{ij} .

At sub-mm wavelengths in a protoplanetary disk, ϕ_ν is dominated by thermal and turbulent broadening, which has a Gaussian profile and a width of,

$$\Delta V = \sqrt{v_{\text{turb}}^2 + \frac{2kT_{\text{kin}}}{\mu m_p}}, \quad (2.21)$$

where T_{kin} is the kinetic temperature of the gas. Thus, at the central frequency, $\phi_{ij}(v_{ij}) = 1/\Delta V\sqrt{\pi}$. Here we have neglected the natural linewidth, resulting from the uncertainty principle, and collisional broadening which results in a Lorentzian profile.

Solving for a solution where the level populations are in equilibrium with the incident radiation field is highly non-trivial. This is typically achieved through the iterative algorithm: Λ -iteration, where Λ is an operator such that,

$$S_{\nu}^{n+1} = \frac{\alpha_{\nu}^{\text{abs}} \cdot B_{\nu}(T)}{\alpha_{\nu}^{\text{abs}} + \alpha_{\nu}^{\text{scat}}} + \Lambda S_{\nu}^n, \quad (2.22)$$

where here B_{ν} is the Planck function. This will be iterated over for all points in the model until S_{ν} converges, however this may take a prohibitive amount of time. Improvements such as the Accelerated-Lambda-Iteration (Cannon, 1973) and Ng-acceleration (Ng, 1974) have allowed for radiative transfer models to consider ever more complex models in a considerably quicker time.

With these level populations set, images of the line emission can be produced through ray tracing with a desired viewing geometry. In the case of a protoplanetary disk, this is typically an inclination and position angle.

LIME – The Line Modelling Engine

Before starting this section, it would be remiss to not mention that there are other, equally good codes for radiative transfer available, for example Mollie (Keto, 1990), RADMC-3D (Dullemond, 2012) and TORUS (Harries et al., 2004). LIME was chosen particularly because of the widespread adoption in the astrochemistry community and the frequent improvements made through community involvement (see <https://github.com/lime-rt/lime>).

Input

LIME requires, as a function of (x, y, z) , the physical properties of the model, including density, gas and dust temperatures, molecular abundances, gas to dust ratios and velocity profiles. As chemical models are typically only calculated in a 2D plane for $z \geq 0$, symmetry is used to extend this model into a full 3D model. The bulk velocity is often assumed to be dominated by Keplerian rotation neglecting the effects of pressure gradients and self-gravity on the bulk motion (Rosenfeld et al., 2013). The linewidth is set with a Doppler- b value which is a fraction of the local soundspeed. Finally, the molecular data must be included, which contain the level energies, transitions rates and collisional cross sections of the chosen molecules. These can be easily obtained from the Leiden Atomic and Molecular Database (LAMDA) (Schöier et al., 2005), which in general contains the most up-to-date rates for a selection of commonly observed species.

Resolution

It is important that the radiative transfer models are sufficiently resolved such that the resulting emission is accurate. In LIME the grid is randomly generated in spherical coordinates within a sphere of user-specified radius with a weighting based on the local density,

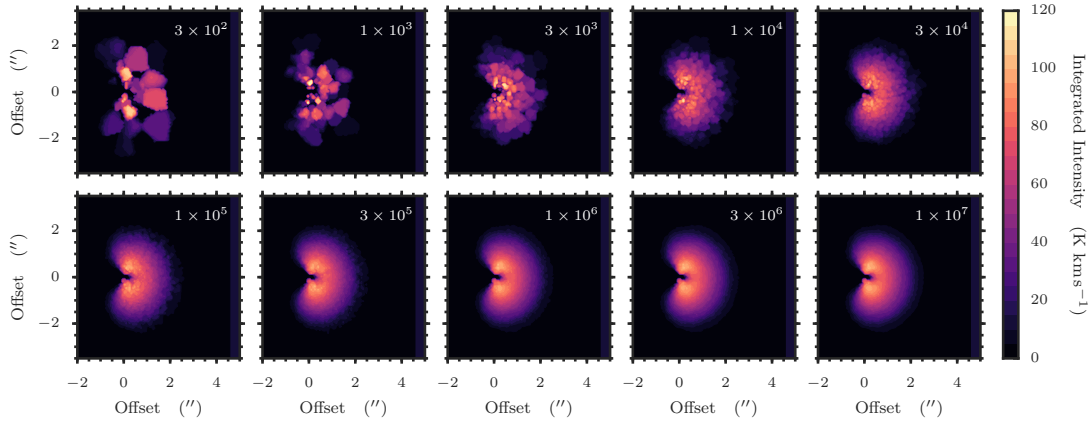


Figure 2.6 Channel maps of CO $J = (3-2)$ showing the impact of changing pIntensity. The value used is shown in the top right corner. Note that the center of the model is shifted to the left.

thereby providing a higher sampling in more dense regions. While this provides a good treatment of the high density inner region, the less dense, outer regions of the disk often suffer from resolution effects. Figure 2.6 demonstrates this by showing the channel maps from a model calculated with various numbers of grid points as shown in the top right of each panel. As can be clearly seen, increasing the number of grid points will provide both more accurate and aesthetically pleasing results.

However, as models with a large number of grid points take considerably longer to calculate, particularly in non-LTE, a trade off between accuracy, reducing grid artefacts and speed must be found. To check the accuracy, one can calculate the integrated intensity of the model and plot it against the number of grid points, given by pIntensity, as done in Fig. 2.7. As the number of points increases, the total flux will converge towards the true value. An adopted value of pIntensity = 10^5 yields a integrated flux within $\lesssim 5\%$ of the ‘true’ value while running in a non-prohibitive amount of time⁹.

However, even with a value of pIntensity = 10^5 , weaker lines, such as CS $J = (5-4)$ which is used extensively in Chapters 5 and 6, suffer from gridding noise (despite recovering the correct integrated intensity). To circumvent this issue, several models are run with the same input parameters then averaged over at the end as this is considerably faster than increasing pIntensity. As the models are assumed to be azimuthally symmetric, the azimuthal dispersion in intensity provides a good estimate of the grid noise. Figure 2.7 compares this for the three emission lines described above for the case of a pIntensity = 10^6 , solid lines, and the average of 10 models with pIntensity = 10^5 , dotted lines. As demonstrated in Fig. 2.6, both methods reproduce the same integrated flux, however the averaged models result in less azimuthal scatter from the grid noise, while running in roughly a third of the time (up to a seventh for non-LTE).

⁹ This is typically around 5 minutes for a model in non-LTE.

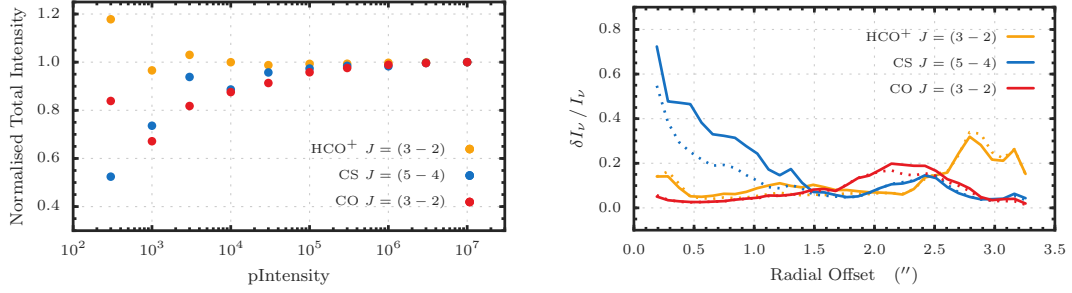


Figure 2.7 Left: Total integrated intensity against the value of pIntensity used for three different molecular emission lines. As pIntensity is increased, the total integrated intensity converges to the ‘true’ value. Right: The azimuthal deviation of the intensity normalised to the average intensity for the three emission lines in the left panel. Solid lines are for the case of pIntensity = 10^6 , while the dotted lines are for 10 models at pIntensity = 10^5 .

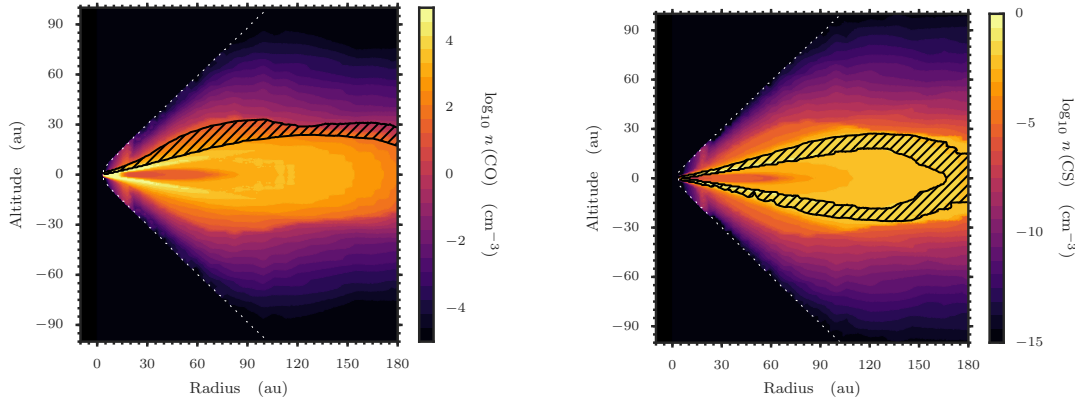


Figure 2.8 Comparison of the emission layers, shown by the hatched area, for CO $J = (2-1)$, left, and CS $J = (5-4)$, right, compared to the molecular abundances shown as the colour scaling. The lower bound of the hatched region is the $\tau \approx 1$ surface, while the upper bound the $n(\text{CO})$ is too small. As CO emission is optically thick, the emission layer is only where $\tau \leq 1$.

Emission Layers

In addition to producing images of line emission, LIME outputs the level populations in each cell which allows for an analysis of the excitation of the molecules. While typically overlooked in many models of protoplanetary disks (Bruderer et al., 2009; Bergin et al., 2013, being notable exceptions), such analyses offer a tremendous amount of information which can be harnessed to allow observations to be designed to make the most of the potential information.

As discussed in Sect.2.2, from a chemical model one can calculate a molecular abundance weighted value of a physical property for a column in a model. One can also consider a similar flux weighted value, which is a more true representation of what one would derive observationally. Figure 2.8 shows the regions of the disk where CO $J = (2-1)$ (left panel) and CS $J = (5-4)$ (right panel) emission emanate from.

Comparison between the CO emission and the CS emission demonstrates the impact

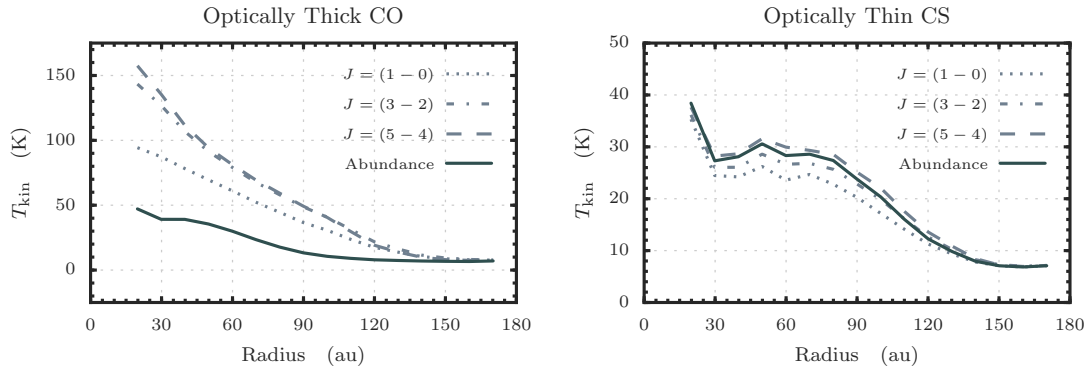


Figure 2.9 $n(\text{CO})$ weighted T_{kin} , black line, compared to those traced with low- J rotational lines, coloured lines. Due to the optical depth of CO, the CO emission will be tracing considerably warmer regions than one would predict from looking at the chemical model.

of optical depth. As CO emission is highly optically thick, the emission will be probing the $\tau \approx 1$ surface, which is elevated with respect to the regions with the highest CO abundance. Conversely, optically thin CS emission will trace predominantly the regions of the highest $n(\text{CS})$. It is important to note, however, that even though CS is optically thin, emission will not be sensitive to the midplane as there is very little gas-phase CS present there.

Differences in the emission layers between molecules, and then between particular transitions for the same molecule, can lead to discrepancies in comparing observations with models. Figure 2.9 compares the flux weighted T_{kin} values for CO, left, and CS, right, for three different rotational transitions, and the equivalent abundance weighted value. Clearly the optically thin CS has values that are similar among transitions and the abundance weighted value, while the CO transitions will trace higher, and therefore hotter, regions in the disk due to the changing optical depths. This will strongly impact derivations which rely on emission lines arising from the same region in the disk and so must be accounted for in analyses of such data.

Local Thermodynamic Equilibrium

There are scenarios where LTE is not an appropriate assumption, therefore requiring a full non-LTE treatment. This is particularly important for studies of turbulence (see Chapter 5) where LTE is assumed in order to recover the thermal broadening component of the line width. Directly from observations it is almost impossible to infer the level of thermalisation of a transition, that is how close it is to LTE, without observing several transitions, or extensive modelling of the disk.

Avoiding large runs of radiative transfer models, the critical density, n_{crit} , is often used to estimate whether a transition will be in LTE. n_{crit} is defined to be the collider density (typically H, H_2 or e^- , but almost always H_2 for protoplanetary disks) which results in an equal rate of radiative decay and collisional decay from an energy level. At densities equal to or greater than n_{crit} , collisional excitation and de-excitation is frequent

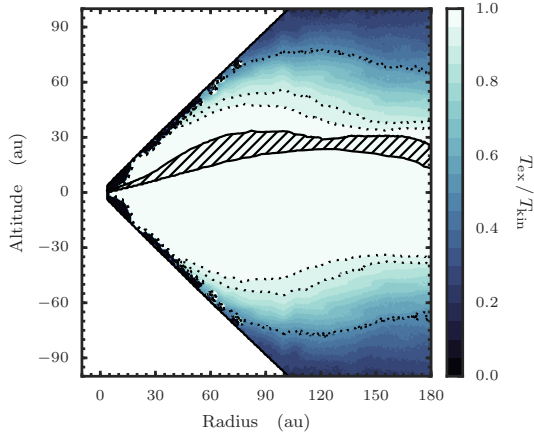


Figure 2.10 Ratio of T_{ex} to T_{kin} for the CO $J = (3 - 2)$ line. The hatched region shows where 95% of the observed flux originates from. The dotted lines show contours of 0.5, 0.9 and 0.95 for $T_{\text{ex}} / T_{\text{kin}}$, moving towards the midplane of the disk.

enough to dominate the level population statistics, yielding a source function which behaves as a blackbody emitter:

$$S_{\nu} = \frac{2h\nu^3}{c^2} \frac{1}{e^{h\nu/kT_{\text{ex}}} - 1} = B_{\nu}(T_{\text{ex}}). \quad (2.23)$$

Therefore, n_{crit} is a reasonable guide for the high densities of a protoplanetary disk; densities in disks are typically $n(\text{H}_2) \gtrsim 10^6$ in the warm molecular layer, see Fig. 2.2. For commonly observed molecules, $n_{\text{crit}} \sim 10^4 - 10^6$, although when radiative trapping is considered, this reduces to $n_{\text{crit}} \sim 10^2 - 10^4$ (Shirley, 2015). However, even at $n(\text{H}_2) = n_{\text{crit}}$, T_{ex} does not necessarily equal T_{kin} and so radiative transfer modelling is essential in understanding the thermalisation.

A commonly used test of the thermalisation of a transition is to compare the two-level excitation temperature, T_{ex} , and the kinetic temperature, T_{kin} . T_{ex} is defined for a two-level system as,

$$T_{\text{ex}} = \frac{\Delta E}{k} \cdot \ln \left(\frac{n_l g_u}{n_u g_l} \right)^{-1}, \quad (2.24)$$

where ΔE is the energy difference between the two energy levels u and l , n_u and n_l are the respective level population densities in cm^{-3} , g_u and g_l the level weight, and k is the Boltzmann constant. Figure 2.10 shows the ratio of T_{ex} to T_{kin} with the coloured shading for CO $J = (3 - 2)$. The dotted contours show, from top towards to midplane, $T_{\text{ex}} / T_{\text{kin}} = 0.5, 0.9$ and 0.95 , and the hatched region shows the emission region. Clearly, assuming CO is in LTE is a good approximation.

2.4 Simulating Observations

A final step in making a model is to simulate an observation. For ALMA, this is particularly easy as a tool is provided in the Common Astronomy Software Applications (CASA) software¹⁰. This allows a user to input a model image and sample it in the uv plane with the appropriate antenna configurations (see Chapter 3 for more details).

¹⁰ https://casaguides.nrao.edu/index.php?title=Simulating_Observations_in_CASA

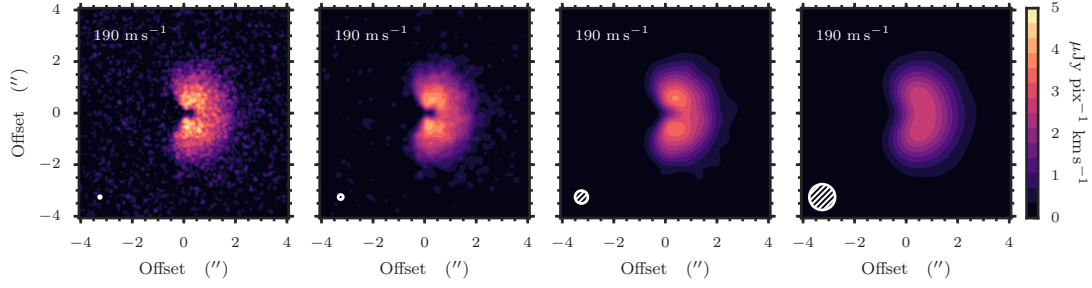


Figure 2.11 Demonstrating the effect of simulated observations. $J = (2 - 1)$ emission imaged with a beamsizes of $0.1''$, $0.2''$, $0.5''$ and $1.0''$, left to right, with the same integration time. This also demonstrates that a longer integration time is required to achieve the same sensitivity with higher spatial resolution observations.

Figure 2.11 demonstrate the impact of simulating an observation for an extended array configuration (yielding a high spatial resolution), left, and a more compact configuration (less spatial resolution but more sensitive for the same integration time), right. These allow for a direct comparison between observations and the theory of protoplanetary disk structure.

Observing Protoplanetary Disks

The first hints of protoplanetary disks were the observation of a ‘nebulosity’ around young stars (Herbig, 1960). Over two decades later in 1983, the Infrared Astronomical Satellite (IRAS) observed strong far-IR excess around pre-main sequence stars due to the reprocessing of the optical stellar light by the dust-rich circumstellar disk, providing further evidence of a circumstellar disk.

It was only with further advances in telescope design that really provided direct evidence for the presence of protoplanetary disks: mm continuum emission was observed around young stellar objects and molecular line emission displayed the double peaked profile indicative of Keplerian rotation (Smith & Terrile, 1984; Sargent & Beckwith, 1987), or the striking silhouette of disks illuminated by the Orion nebula (O’dell & Wen, 1994). These observations kick-started the study of protoplanetary disks and planet formation with waves of new, exciting observations throughout the following years.

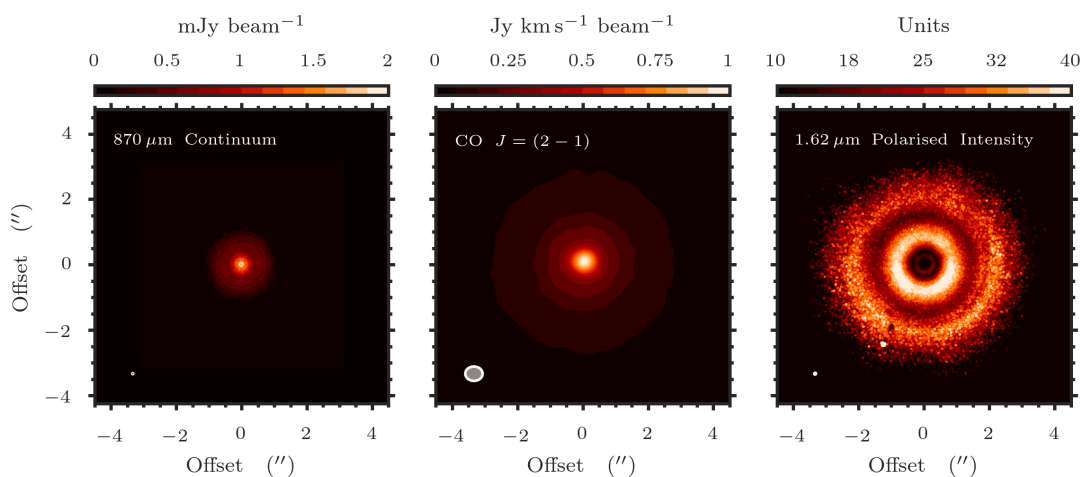


Figure 3.1 TW Hya as seen in 870 μm continuum (Andrews et al., 2016), CO $J = (2-1)$, (Teague et al., 2016) and 1.62 μm polarized intensity with r^2 scaling (van Boekel et al., in press). The spatial scales between the three panels are the same to demonstrate the different sizes observed in emission. The beam sizes are shown in the bottom left corner.

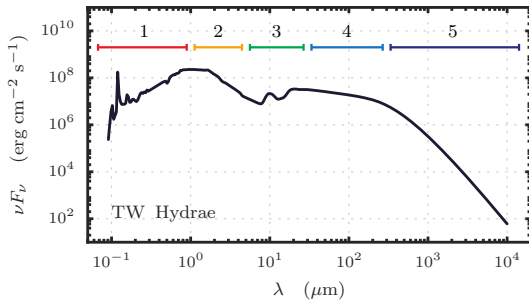


Figure 3.2 A model of the SED of TW Hya from the ProDiMo project (Woitke et al., 2009). The wavelength regions are numbered according to the text.

Even today, facilities such as the ALMA in the Chilean Atacama desert and the VLA near Socorro in New Mexico, USA, are opening up new frontiers in the study of protoplanetary disks. Extreme adaptive optics systems, such as (Hi)CIAO on the Subaru telescope atop Maunakea in Hawaii, Spectro-Polarimetric High-contrast Exoplanet Research (SPHERE) on the Very Large Telescope (VLT) in Paranal, Chile, or the Gemini Planet Imager (GPI) mounted on the Gemini South Telescope in the Chilean Andes, while developed for the discovery of exoplanets, are revealing stunning substructures in disks which could be the first observations of planet-formation caught in the act.

Such a variety of telescopes allows disks to be studied across a huge wavelength range, with each wavelength sensitive to particular components of the disk. Figure 3.1 demonstrates this by showing TW Hya, the closest protoplanetary disk to Earth and one of the most well studied disks, in three wavelengths: 870 μm continuum from Andrews et al. (2016), left panel, CO $J = (2 - 1)$ at 1.3 mm, from Chapters 5 and 6 in the central panel, and 1.62 μm polarized intensity with r^2 scaling from van Boekel et al. (in press) in the rightmost panel. Clear differences in the morphologies of the emission demonstrate that observations across a wavelength range are essential in fully characterising a disk.

As the instruments have advanced, so have the observations and their subsequent analyses. In this Chapter I will briefly review the observational methods employed to study protoplanetary disks and recover properties of the disk by assuming a physical form described in Chapter 2. As in Chapter 2, more focus will be paid to the techniques used in this thesis, namely sub-mm interferometry.

3.1 Spectral Energy Distributions - SEDs

As spatially resolved observations of disk were impossible, a common method to characterise objects was by their SED, essentially how the amount energy emitted at a given wavelength changes. These are typically viewed by plotting νF_ν against λ , as shown in Fig 3.2.

The spectral slope between 2 and 25 μm , α_{IR} , was used by Lada (1987) to define the spectral class of a young stellar object (YSO) into I, II or III, with additions from Andre et al. (1993), who introduced an earlier Class 0 stage, and Greene et al. (1994), who introduced a ‘flat-spectrum source’, fitting in between classes I and II. To further complicate matters, Meeus et al. (2001) introduced a sub-category, Class I and II for Herbig Ae/Be stars depending on whether a black body is required, in addition to a power-law

profile, to recover the continuum emission. In general, a protoplanetary disk falls into a Class II source with $-1.6 < \alpha_{\text{IR}} < -0.3$, and exhibiting strong H α and UV emission due to accretion. Note, however, that this method is incredibly sensitive to the viewing angle, for example a highly inclined Class II source looks like a Class I source, so detailed modelling must be used to distinguish the disk properties (Woitke, 2015).

The wavelength range can broadly be split into five main regions, each of which is sensitive to a particular component of the disk (as shown in Fig. 3.2):

1. $\lambda \lesssim 1\mu\text{m}$, the stellar blackbody emission dominates the energy emission at these short wavelengths, allowing for a constraint of the stellar properties.
2. $1\mu\text{m} \lesssim \lambda \lesssim 5\mu\text{m}$, this near-IR excess with respect to a blackbody curve was the indication of stellar light being reprocessed by the disk. The exact geometry of this region is poorly constrained, however a blackbody of $T \sim 1500$ K generally reproduces the feature well.
3. $5\mu\text{m} \lesssim \lambda \lesssim 30\mu\text{m}$ are filled with silicate dust emission features. Much attention has been paid to this region as the high density of bending and stretching modes of a solid lattice provides the best opportunity to constrain the grain properties, such a size, composition and mineralogy.
4. $30\mu\text{m} \lesssim \lambda \lesssim 300\mu\text{m}$ is well described by a power-law and can be explained as an optically thick blackbody emitter with a radial temperature distribution.
5. $\lambda \gtrsim 300\mu\text{m}$ is a continuation of the blackbody emitter with a radial temperature gradient which dominates the short wavelength ranges, however is now optically thin due to the drop in surface density in the outer regions of the disk.

Thus, with a model of a disk, generally in some parametrised form as described in Chapter 2, an SED can be fit for and the degeneracies in geometries and structures can be understood, although spatially resolved measurements would be need to fully break the degeneracy.

Figure 3.3 demonstrates the utility of SED modelling by showing a the SED of a star and disk system with different inner edges of the disk calculated using the code of Zakhzhay et al. (2015). The stellar blackbody dominates at smaller wavelengths, while the reprocessing of optical light into infra-red and longer wavelengths creates a distinct enhancement at longer wavelengths. To first order, the depth between the two peaks of νF_ν is sensitive to the inner edge, allowing for the detection of inner gaps in the disk and is often used as a criteria for classifying a transition disk.

3.2 Radio Observations

The low energy environments in the outer protoplanetary disk ($r \gtrsim 30$ au) leads to emission at wavelengths in the sub-mm and longer regime, as seen with SEDs. Thus, radio observations are ideally suited to trace the outer disk component. Furthermore, the longer

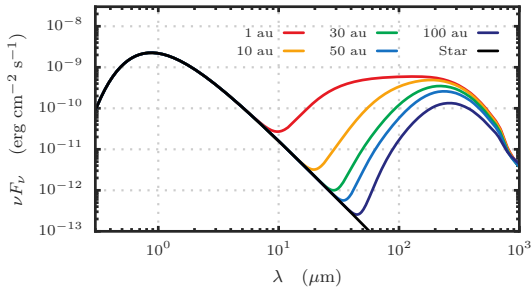


Figure 3.3 Examples of the SEDs of a star and disk system with different inner edges. With less material close to the star, the disk is dominated by the cooler, outer disk regions.

wavelengths allow for much higher spectral resolutions due to use of heterodyne technology which is not available at shorter wavelengths, allowing for detailed examinations of the disk kinematics. Observations can be broadly split into either continuum observations, tracing the \sim mm sized dust grains which reside in the midplane of the disk, or molecular line emission which traces the warmer, molecule rich gas roughly a pressure scale height above the disk midplane (see Fig 2.8).

In the following section I briefly describe the basics of radio observations with both a single dish telescope and an interferometer based on [Wilson et al. \(2010\)](#).

Single Dish

The large beams of single dish telescopes eclipse the projected sizes of protoplanetary disks¹ and so provide spatially integrated spectra over the whole disk. As with SED modelling, much can be gleaned from this if a model of a disk is assumed.

Unresolved continuum emission allowed for the first attempts to measure the mass of the disk, M_{disk} , through

$$M_{\text{disk}} = \frac{F_\nu d^2}{\kappa_\nu B_\nu(\langle T \rangle)}, \quad (3.1)$$

where κ_ν is opacity and $B_\nu(\langle T \rangle)$ is the Planck function at the average disk temperature ([Beckwith et al., 1990](#)). At mm wavelengths, the Planck function is in the Rayleigh-Jeans regime such that $B_\nu \approx 2\nu^2 kT/c^2$, thus scaling linearly with the temperature rather than exponentially, and therefore being less sensitive to uncertainties in T . This technique has been used for several large surveys of disks, most notably [Beckwith et al. \(1990\)](#), [Andrews & Williams \(2007\)](#) and [Andrews et al. \(2013\)](#).

[Horne & Marsh \(1986\)](#) provide the seminal work on line emission in accretion disks and demonstrate that the projected velocity at (r, θ) (in model coordinates), is given by,

$$v_{\text{proj}}(r, \theta) = \sqrt{\frac{GM_\star}{r}} \sin i \cos \theta, \quad (3.2)$$

assuming that the disk is in Keplerian rotation. As this profile is sampled at a finite velocity resolution Δv , then the boundaries of the region of the disk with $v_{\text{proj}} = v_{\text{obs}}$ are given by, following [Guilloteau et al. \(2006\)](#),

¹ The Institut de Radioastronomie Millimétrique (IRAM) 30 m telescope has a beamsize of $\approx 11''$, or a projected size of 1650 au at 150 pc, the distance of Taurus, at 1 mm.

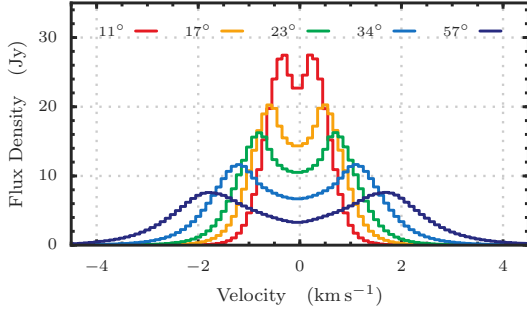


Figure 3.4 The same disk model at different inclinations (shown in the legend in radians). More inclined disks have much broader lines and larger distances between peaks. The line is CO $J = (3 - 2)$.

$$r_{\pm}(\theta) = \frac{GM_{\star}}{(v_{\text{obs}} \pm \Delta v / 2)^2} \sin^2 i \cos^2 \theta, \quad (3.3)$$

with r_{\pm} being the inner and outer radius of the emitting regions. The outer radius of the disk is the limit for r_{-} . This pattern is the one seen in the first moment map, as displayed in Fig. 3.5. The emitting area is therefore a function of velocity with the maximum emitting area when $r_{-} = r_{\text{out}}$, yielding the typical double peaked profile, as demonstrated in Fig. 3.4. While this double peaked profile is sometimes indicative of self-absorption, for the case of protoplanetary disks it is primarily due to this geometrical effect.

Figure 3.4 demonstrates that for the same disk viewed at different inclinations with yield different flux density profiles. With the assumption of a disk undergoing Keplerian rotation, one can model this flux density profile to constrain some geometrical parameters of the disk.

Futhermore, [Guilloteau et al. \(2013\)](#) show that, under the assumption of a disk with a uniform temperature T , the outer radius can be estimated from the line width ΔV ,

$$r_{\text{out}} = d \times \left(\frac{\int S_{\nu} dv}{B_{\nu}(T) \rho \Delta V \pi \cos i} \right)^{\frac{1}{2}}, \quad (3.4)$$

for an object at a distance d pc, where ρ is an order of unit constant to account for the optical depth of the line ([Guilloteau & Dutrey, 1998](#)).

In addition to geometrical parameters of the disk, the large bandwidths and large collecting areas of single dish telescopes allows for spectral scans of objects in order to identify the molecular content. As described in Chapter 1, the molecular inventory of protoplanetary disks is poorly known, but holds great potential in helping trace the physical properties of the disk. With measurements of the total flux of particular lines from a disk allows one to better design a high-resolution observation with an interferometer in order to spatially resolve the emission.

Interferometry

For the study of protoplanetary disks, the limiting feature of single dish telescopes is their spatial resolution. Interferometry combines several dishes to synthesise a large aperture, allowing one to achieve spatial resolutions which would typically require dishes tens of kilometres wide. Combining the signals of the two antennas, or more precisely correlating them, allows one to measure the spatial coherence function,

$$V_\nu(\mathbf{r}_1, \mathbf{r}_2) \approx \int I_\nu(\mathbf{s}) \exp(-2\pi i \nu \mathbf{s} \cdot (\mathbf{r}_1 - \mathbf{r}_2) / c) d\Omega, \quad (3.5)$$

where \mathbf{r}_i is the position of the i^{th} antenna and \mathbf{s} is the direction to the source.

Due to the dot product in Eqn. 3.5, a two dish interferometer would have the greatest spatial resolution along the baseline direction, $(\mathbf{r}_1 - \mathbf{r}_2)$. Increasing the number of baselines by including more antennas provides two main improvements: firstly, with baselines in different directions, the interferometer gains a spatial resolution which tends towards a more isotropic sensitivity. Secondly, more dishes mean a larger collecting area and increase the sensitivity of the telescope.

The visibilities, V_ν are the Fourier transform of the intensities I_ν . With a large number of baselines and many frequencies this transformation can be computationally expensive in addition to introducing artefacts into the resulting image. Early interferometers had only a few antennas, SMA and PdBI having 8 and 6 antennas respectively. This meant a poorly sampled uv plane² leading to images with many artefacts. Many analyses work in the visibility plane to avoid this complication. For example, [Menu et al. \(2014\)](#) used the visibility profiles to understand the inner radial structure of TW Hya while [Zhang et al. \(2016\)](#) analysed the visibilities to tease out radial structure which is not apparent in the image, but were later confirmed with high-resolution imaging.

To produce an image, the visibilities must first be *imaged* and then *cleaned*. The *imaging* process is simply taking the Fourier transform of the visibilities. A ‘dirty beam’ is the Fourier transform of the antenna configuration, or uv -coverage, and the interferometric equivalent to a point spread function (PSF) in optical astronomy. A Fourier transform of the visibilities produces the ‘dirty image’, a convolution of the ‘dirty beam’ and the observation. To deconvolve the ‘dirty beam’ from the ‘dirty image’, *cleaning* is required.

The original CLEAN algorithm was developed by [Högbom \(1974\)](#) and works on the assumption that the true sky distribution is made up of many point sources³. The algorithm is iterative, at each step locating the brightest pixel in the ‘dirty image’ and adding this is to a ‘clean component’ list. At this position in the ‘dirty image’, a ‘dirty beam’ is removed resulting in a ‘residual image’. This cycle continues until the ‘residual image’ has a uniform noise of some predetermined value. The ‘clean component’ list is convolved with a synthesized ‘clean beam’, a fit to main component of the ‘dirty beam’, and added to the residual map. This is known as the ‘clean image’.

Despite the additional effort required to image interferometric data, analysis in the image plane provides a much more intuitive look at the disk. The imaging of a set of observations results in data cubes with two spatial axes (right ascension and declination) and a spectral axes (typically converted to a velocity relative to the systemic velocity of the object). At each position in the cube an intensity $I(v, x, y)$, where (x, y) is the sky position relative to the centre of the object, is measured. Given the spatial resolution of

² The uv plane is the plane on which the antenna stands. In Eqn. 3.5, $\mathbf{r}_i = (u, v)$.

³ Although this is not true for the case of disks, it is one of the most robust methods. Other deconvolution methods are used, such as the maximum entropy method ([Casassus et al., 2006](#)).

the instrument, this can mean one spectrum for an entire object, or many across the area of the object.

Continuum observations provide the highest angular resolution observations possible. Due to the extensive bandwidths over which continuum measurements are taken, high sensitivities are achievable for angular resolutions on the order $\theta_{\text{beam}} \approx 0.03''$, in times which are not prohibitively long.

As continuum emission is dominated by grains which are approximately the wavelength size, observing continuum over a range of wavelengths allows for analysis of the grain size distribution (Testi et al., 2014, and references therein). Tazzari et al. (2016) have recently demonstrated that by using a model of a disk which contains a distribution of grain sizes, observations spanning $\lambda = 0.88$ to 9.83 mm can be simultaneously fit to constrain grain populations. Such work provides the foundation for additional studies which aim to fit a much larger range of grain sizes. A similar method was performed for HL Tau by Carrasco-González et al. (2016) who used the more optically thin 7 mm emission, observed with the Extended Very Large Array (eVLA) to measure the mass of the dust and identified a clump in emission, potentially the start of planet formation.

For molecular line emission, the emission is not integrated over the entire bandwidth as the spectral information provides kinematical information. A powerful, and frequently used, first step in exploring such a spectral data cube is to look at the moment maps. The moments of a distribution condense properties of that distribution to a single, easy to represent, number. In studies of protoplanetary disks, the first three moments are the most commonly used. The zeroth moment is the integrated intensity along a pixel,

$$\mu_{x,y}^0 = \int I(v, x, y) dv, \quad (3.6)$$

which shows the total flux that arises from a particular pixel. The first moment is the intensity weighted average velocity,

$$\mu_{x,y}^1 = \frac{1}{\mu_{x,y}^0} \int I(v, x, y) \cdot v dv, \quad (3.7)$$

and describes the average line of sight velocity of a pixel. Finally the second moment, which is the intensity weighted velocity dispersion,

$$\mu_{x,y}^2 = \frac{1}{\mu_{x,y}^0} \cdot \sqrt{\int (v \cdot I(v, x, y) - \mu_{x,y}^1)^2 dv}, \quad (3.8)$$

is the velocity dispersion around the line centre, proportional to the local line width. Figure 3.5 shows examples of zeroth, first and second moments for CO $J = 3 - 2$ emission from a model of TW Hya.

The zeroth moment is typically used to understand the spatial distribution of the emission and basic geometrical properties of the disk. Assuming an azimuthally symmetric disk, the ratio of the semi-major and semi-minor axes allows for an inclination i to be calculated, while the angle between the semi-minor axis (the rotation axis) and North is the position angle, PA. For the example in Fig. 3.5, $i = 7^\circ$ which means the semi-major and

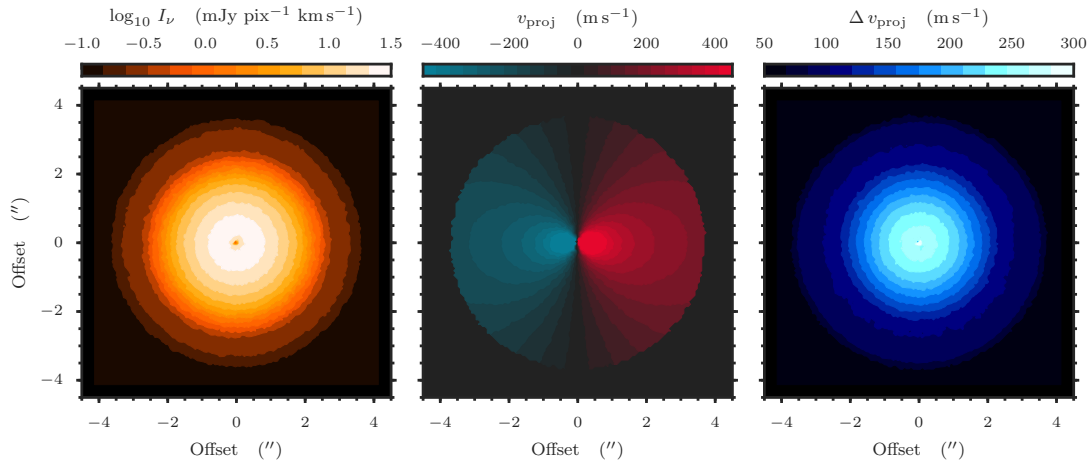


Figure 3.5 Zeroth, first and second moment maps for CO $J = (3 - 2)$ from a model of TW Hya which is inclined at 7° . No sampling effects or noise are considered.

minor axes are incredibly hard to distinguish and thus an observational measurement of i and PA are challenging.

Furthermore, this can be collapsed into a radial flux profile which more clearly shows radial features, such as at the double rings of DCO⁺ emission in IM Lup (Öberg et al., 2015), a secondary desorption ring of CO in AS 209 (Huang et al., 2016), or the surface density depression traced by CS in TW Hya (Chapter 6). Azimuthally averaging also provide a large increase in the signal-to-noise ratio (SNR). As the noise in interferometric images is dominated by uncorrelated noise (note that side-lobes may produced correlated noise in particularly strong sources), the statistics are set by Poisson counting statistics. Thus, for an annuli of a disk with circumference c , the SNR will be improved by a factor of $\sim \sqrt{c/\theta_{\text{beam}}}$, where θ_{beam} is the projected FWHM of the beam (see also Yen et al., 2016).

The first moment is often used as a verification of Keplerian rotation and provides a tight constraint on the dynamical mass of the system, $M_\star \sin i$. This is often far more precise than measurements of the individual values. For example, in Chapter 5 the dynamical mass of TW Hya is constrained to a precision of $\sim 1\%$, while independent measurements of M_\star and i have uncertainties of $\sim 50\%$ each. Furthermore, the direction of zero projected velocity displays the orientation of rotation axis of the disk (parallel to the y -axis for Fig. 3.5) which can be compared with the values calculated from the zeroth moment.

The second moment is used less often used as higher moments are much more sensitive to the noise in the distribution. Nonetheless, insights into the line width as a function of position can be useful. Due to the velocity gradient ($V_{\text{Keplerian}} \propto r^{-0.5}$), inner regions of the disk will have much broader lines, as demonstrated by the right most panel of Fig. 3.5, making the isolation of the turbulent component extremely hard.

While single dish telescopes provide spectra about the disk as a whole, the spatial resolution of interferometers allow one to measure *local* spectra. These spectra hold a great deal of information about the local properties, such as the line width in studies of turbulence (see Chapter 5). The high spectral resolutions and increased sensitivity

achieved by ALMA promise for much more precisely measured values.

An important first step is to understand how well one can extract the true values from a spectra with a finite sampling rate and corrupted with noise. Following a similar methodology to that of [Lenz & Ayres \(1992\)](#), we explore how well we can recover the properties of a Gaussian curve when fitting a noisy, poorly sampled version of it. The true line profile, \mathcal{L} , is assumed to be entirely a Gaussian,

$$\mathcal{L}(v, v_0, \Delta v, A) = A \cdot \exp\left(-\frac{1}{2} \left[\frac{v - v_0}{\Delta v}\right]^2\right), \quad (3.9)$$

where v_0 is the line centre, Δv is the line width, where the FWHM = $4 \ln 2 \cdot \Delta v$, and A , the amplitude of the line. To simulate observations, a sampling rate is chosen where the spectral resolution is defined as the number of samples per Δv . The noise per channel is a fraction of the peak intensity per channel⁴ such that for a 5σ detection of $A = 1$ would require $\sigma_{\text{noise}} = 0.2$.

Line profiles are generated by drawing random values of $\{v_0, \Delta v, A\}$ from a Normal distribution. Each of these profiles are ‘observed’ by corrupting with noise and sampling appropriately. The ‘observed’ line profiles are fit with a Gaussian using `scipy`’s⁵ `curve_fit` routine which make use of the Levenberg-Marquardt algorithm to make a non-linear least squares fit. Only results where the peak is found to be above 5 times the noise level (equivalent to a 5σ detection) and the deviation of the derived line centre is less than 20% from the true value (as it is expected that the line centre should be known to relative high precision a priori) are considered to be good fits and kept. The best-fit values are compared with the true values to provide an understanding of how sensitive the recovery of the parameter is to noise and sampling effects.

Figure 3.6 shows how well $\{v_0, \Delta v, A\}$ can be recovered given $\sigma_{\text{noise}} = \{10^{-3}, 10^{-2}, 10^{-1}\}$ and for a range of sampling rates. As expected, all parameters are recovered more accurately with better sampling and lower noise. With ALMA, we can achieve roughly a velocity spacing of $\sim 20 \text{ m s}^{-1}$ with protoplanetary disks having local linewidths on the order of FWHM $\sim 500 \text{ m s}^{-1}$, thus achieving a resolution of ~ 10 . If the line is measured at a level of 10σ (typical of something like CS, however brighter lines such as CO will be an order of magnitude greater) at this sampling rate, we would expect to derive $\{v_0, \Delta v, A\}$ accurate within 20, 30 and 5% respectively. These values scale linearly with σ_{noise} , so to first order thus an improvement in sensitivity per channel of 10 would improve the accuracy of the parameters by a similar factor.

3.3 Model Fitting

In addition to understanding the local properties of emission, it is important to make a connection between the observed emission and the global picture of the protoplanetary disk. To this end, model fitting has proved to be an essential tool in the astronomer’s

⁴ I have chosen to quantify the spectral resolution and channel in this way as these are typically the inputs used to estimate the integration time when proposing for ALMA.

⁵ <http://scipy.org/>

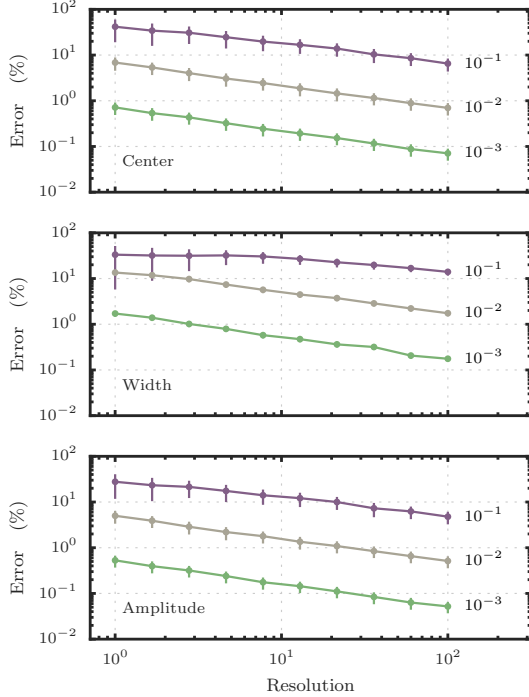


Figure 3.6 How well can Gaussian parameters be recovered with noisy spectra. The resolution is the number of samples per $\Delta\nu$ and the noise levels, represented by the different coloured lines, are specified as a fraction of A per sample. The error bars represent the 16th (lower) and 84th (upper) percentiles of a sample of 1000 measurements.

toolbox. With parametric descriptions of disk providing quantitatively comparable structures to what we observe (see Chapter 2) and the availability of packages such as *emcee* (Foreman-Mackey et al., 2013), it is easy to compare a huge sample of models with observations to find best fitting parameters.

In essence, one describes the disk structure through a set of equations with free parameters. These free parameters are then varied and the resulting model compared with the observations by some ‘goodness of fit’ value, typically χ^2 . By minimising χ^2 , the model which best described the observations can be found. Although all attempts in the literature follow the same general scheme, each version is unique in terms of the model used, the goodness-of-fit statistics used and so on. As such, I will focus on *Diskfit* which is used in Chapters 4 and 5 to recover a model disk structure.

Diskfit was introduced by Dutrey et al. (1994) and Guilloteau & Dutrey (1998) and has been continually improved upon since. Dartois et al. (2003) and Piétu et al. (2007) detail the major workings and intricacies of the code, however here I provide a short overview of the methodology.

First, geometrical properties of the disk are fit for, namely: the central position of the star, x_0 (″), and y_0 (″); the systemic velocity, V_{LSR} (km s^{-1}); the position angle, PA ($^\circ$), and inclination, i ($^\circ$), of the disk. The inclination and position angle are forced to be in the range $0^\circ \leq \text{PA} < 360^\circ$ and $-90^\circ \leq i \leq 90^\circ$ such that the reference value for the velocity profile is always positive and that position angle refers to the rotation axis.

Then, the physical properties which affect line emission are assumed to vary as a radial power law:

$$a(r) = a_0 \left(\frac{r}{r_0} \right)^{-e_a}, \quad (3.10)$$

where a_0 is the parameter value at the reference radius r_0 . A power-law is used as it is scale-invariant and simple to work with. The standard is such that positive exponents, e_a , imply a decrease of the physical quantity with radius. The disk is assumed to be azimuthally symmetric so only a radial profile needs to be supplied.

Physical parameters which are fit for include the projected velocity, kinetic temperature, column density of the molecule, line width, inner and outer radii, and the pressure scale height. With this molecular distribution, ray tracing is performed assuming an escape probability, yielding model visibilities. These model visibilities are compared to the observations in the uv -plane in order to minimise artefacts from the Fourier transforms. The goodness of fit was determined with a χ^2 value and MCMC methods were used to efficiently sample the parameter space, yielding posteriors for all the free parameters.

Unlike some of the parametric models discussed in Chapter 2, Diskfit assumes a vertically isothermal disk and a radially varying pressure scale height to account for the flaring of the disk. This provides a good representation of the molecular layer as where the emission arises from can be well approximated as a thin, vertically isothermal layer (see Fig. 2.8 in Chapter 2). Other attempts at fitting observations use considerably more complex models, for example [Flaherty et al. \(2015\)](#) who include a two-zone vertical temperature structure, a radially dependent pressure scale height and changing values of $x(\text{CO})$.

The final product of observational analyses should be as accessible as possible for the community. With such a huge variety of modelling options available, it is more beneficial to provide a clear measure of what has been detected and allow others to perform their own forward-modelling. With data archives filling up fast, more and more projects will be able to use the same data for different science goals. Such an abundance of data will quickly bring studies of protoplanetary disks forwards, challenging us to revise our current understanding of planet formation.

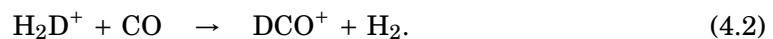
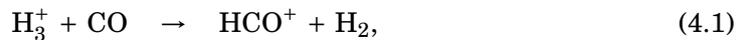
Deuterium Fractionation and Ionisation in DM Tau

Based on [Teague et al. \(2015\)](#), published in *Astronomy & Astrophysics*.

4.1 Motivation

A fundamental aspect of the physical structure of protoplanetary disks is the thermal and ionization structure. As discussed in Chapter 1, the thermal structure has strong implications for the chemistry and excitation conditions of molecular line emission while the ionization structure dictates the active chemical pathways and the possibility of MRI turbulence.

The key molecular ion HCO^+ and its deuterated isotopologue DCO^+ are powerful probes of these two properties. This can be easily seen from their main formation pathways:



Given the high abundance of CO within the disk, the abundance of these molecules will strongly depend on the available ions, H_3^+ and isotopologues, which is set by the ionization structure of the disk.

Additionally, deuterium fractionation is frequently used as a probe of thermal history. The main deuterium reservoir in the ISM is in HD, which, through reactions with H_3^+ , can transfer the deuterium into ever more complex species. The ratio of deuterated species to non-deuterated species is treated as a thermometer as the main liberation pathway for deuterium in cold environments ($T \lesssim 50$ K) is the exothermic reaction

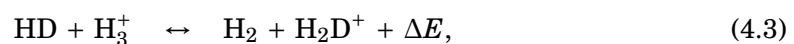


Table 4.1

DM TAU STELLAR AND DISK PROPERTIES		
Right Ascension	(J2000)	04 ^h 33 ^m 48 ^s .733
Declination	(J2000)	+18°10′09″.89
Spectral Type		M1
Effective Temperature	(K)	3720
Stellar Luminosity	(L _⊙)	0.25
Accretion Rate	(M _⊙ yr ⁻¹)	2 × 10 ⁻⁹
Disk Mass	(M _⊙)	0.05
R _{out}	(au)	800

Note: Values compiled from [Dutrey et al. \(2007\)](#) and [Henning et al. \(2010\)](#).

where $\Delta E = 232$ K, or $T_{\text{kin}} \approx 30$ K ([Roberts & Millar, 2000](#)). Thus, at temperatures lower than 30 K, one would expect to see an enhancement of deuterated molecules relative to the ISM [D]/[H] ratio of $\sim 10^{-5}$.

By tracing the level of deuteration through the evolutionary stages, from molecular clouds, through star forming cores and into protoplanetary disks, we can begin to trace the material which ultimately ends up forming planets and forging a link to our Solar System ([Cleeves et al., 2014b](#)). Observations spanning a range of evolutionary stages are essential in understanding the level of chemical processing which occurs from one stage to another.

In this project, PdBI observations of HCO⁺ $J = (3 - 2)$, $(1 - 0)$ and DCO⁺ $J = (3 - 2)$ in DM Tau were used in conjunction with extensive chemical modelling to understand the thermal and ionization structure of DM Tau. Section 4.2 describes the observations, data reduction and fitting of a parametric model. Section 4.3 discusses the chemical model set-up and the suite of models run to fit the observed data. The results are discussed and summarised in Sections 4.4 and 4.5.

4.2 Observations

Observations were carried out with the IRAM PdBI. Table 4.1 presents basic stellar properties and disk parameters of DM Tau taken from previous studies. We observed two transitions of HCO⁺, the $J = (1 - 0)$ line at 89.18852 GHz and the $J = (3 - 2)$ line at 267.55762 GHz, and the $J = (3 - 2)$ transition of DCO⁺ at 221.611258 GHz. The HCO⁺ $J = (1 - 0)$ data included those described in [Piétu et al. \(2007\)](#) and were augmented with longer baseline data (with baselines up to 760 m) obtained in late February and early March 2008. The DCO⁺ data were obtained between August and December 2007, with baselines ranging from 15 to 175 m, yielding an angular resolution around 1.3″. The HCO⁺ $J = (3 - 2)$ data were obtained in Dec 2008, with a similar baseline coverage to the DCO⁺ data.

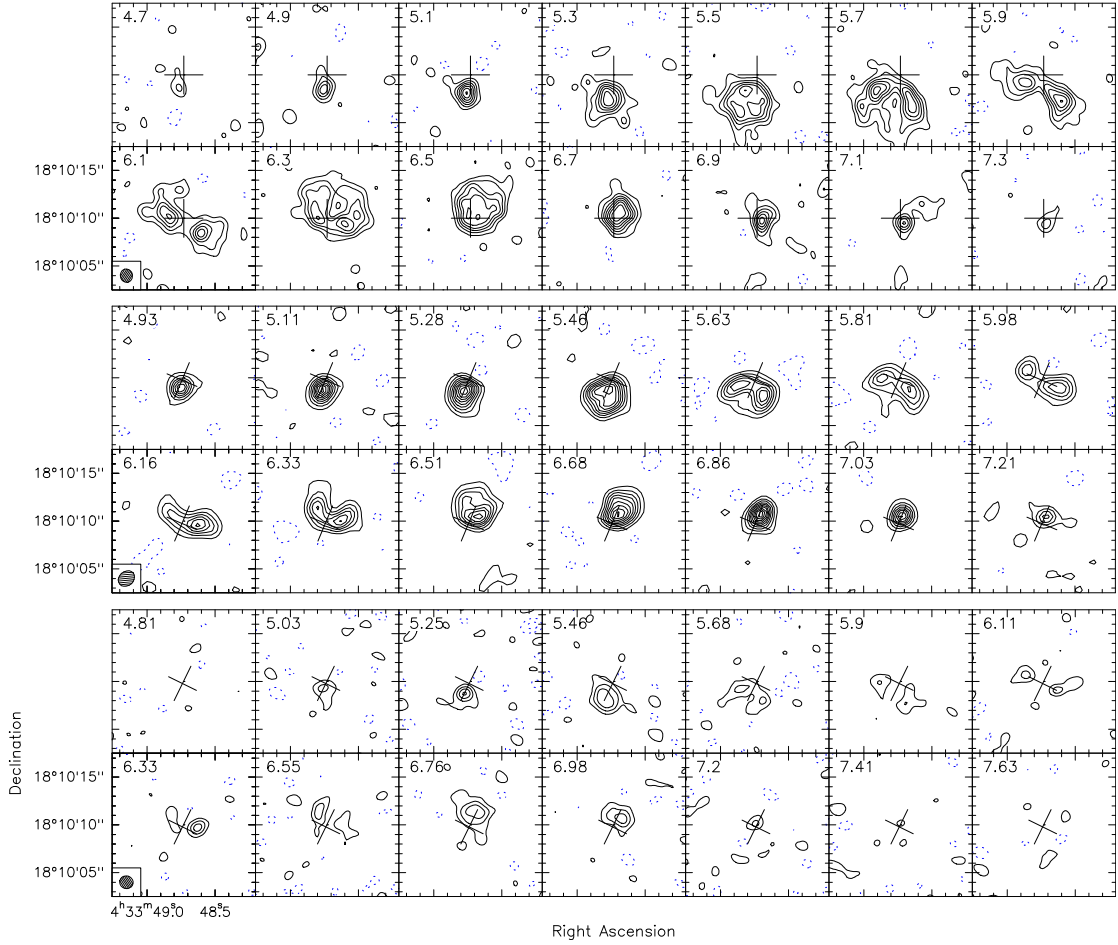


Figure 4.1 Channel maps of: $\text{HCO}^+ J = (1-0)$, top, with $\sigma = 3.7 \text{ mJy beam}^{-1}$ (0.32 K) and contour spacing of 2.5σ ; $\text{HCO}^+ J = (3-2)$, middle, with $\sigma = 100 \text{ mJy beam}^{-1}$ (0.64 K) and contour spacing of 2.5σ ; and $\text{DCO}^+ J = 3-2$, bottom, with $\sigma = 30 \text{ mJy beam}^{-1}$ (0.42 K) and contour spacing of 2σ emission from DM Tau. The beam size, shown by the filled ellipse, for each line is $1.4'' \times 1.26''$, $1.85'' \times 1.49''$ and $1.4'' \times 1.33''$ respectively. The velocity of each channel shown in the top left corner in km s^{-1} while the cross in the centre shows the position of the host star and the position angle of the major and minor axes of the disk. Dashed contours show negative values.

Data Reduction

The IRAM package GILDAS¹ was used for data reduction and imaging. All data were smoothed to similar spectral resolutions, 0.17 to 0.20 km s^{-1} , for comparison. Self-calibration was applied to all three lines and the dust thermal continuum was subtracted from the line spectra as done in [Dutrey et al. \(2007\)](#).

Channel maps of the emission lines are shown in Fig. 4.1, with contours in levels of 2.5σ for the HCO^+ data and 2σ for DCO^+ . The rms noise values were calculated in a line free channel and are 3.7, 100 and 30 mJy beam^{-1} respectively. The need to plot tighter 2σ contours for $\text{DCO}^+ J = (3-2)$ highlights the lower intensity of this line relative to the HCO^+ emission, which is to be expected for a deuterated isotopologue.

¹<http://www.iram.fr/IRAMFR/GILDAS>

Observational Results

The DISKFIT package, described in Section 3.3, was used to model the observations and extract column densities for the two molecules. Continuum emission was used to derive the geometrical parameters, such as inclination and position angle, while the molecular emission lines were used to fit physical properties of the disk.

The derived best-fit parameters for the three emission lines and the continuum are shown in Table 4.2. Geometrical properties of the disk (systemic velocity, inclination, position angle and Keplerian velocity at 100 au) were found to be in good agreement with previous studies on DM Tau using the DISKFIT approach (Guilloteau & Dutrey, 1998; Piétu et al., 2007; Dutrey et al., 2007).

Due to the uncertainty in optical depth of the HCO^+ rotational lines, the HCO^+ images were analysed in three different ways. In case A, the $J = (1-0)$ and $(3-2)$ images were fit for independently. The derived parameters are presented in Col. 1-2 of Table 4.2. The HCO^+ $J = (3-2)$ line is largely optically thick, and thus provides a good estimate of the kinetic temperature, however, the surface density cannot be well constrained from this data. A best fit outer radius of around 500 au was found for this line. On the other hand, HCO^+ $J = (1-0)$ extends radially further (to at least 750 au), and is mostly optically thin. Thus, the derived temperature heavily relies on the power law extrapolation at low radii. We also note that the $J = (3-2)$ line requires an inner radius around 50 au. A lack of emission from the inner 50 au may bias the temperature derived from the $J = (1-0)$ line towards low values.

In case B, the $J = (1-0)$ and $(3-2)$ lines were assumed to have the same excitation temperature. Both transitions were fit for simultaneously with an outer radii set to 750 au. Results are given in Col. 3. The derived temperature law is now much steeper, $q = 1.00 \pm 0.04$, and the surface density law much flatter. The derived surface densities are also lower roughly a factor of 2 to 5 between 200 and 400 au compared to the separate fits.

Finally, in case C, the power law assumption was relaxed and the temperature and surface densities were fitted at 5 different radii, extrapolating by power laws in between. The solution is within the errors consistent with case B, and thus case B was considered the best description of the disk and used implicitly in the following discussion.

However, neither approach is perfect: in case A, the extrapolation required to derive the temperature profile from the $J = (1-0)$ line is hazardous. On the other hand, in case B the vertical temperature gradients, which are expected in disks, are neglected, despite the higher opacity of the $J = (3-2)$ line naturally leading to higher excitation temperature compared to the $J = (1-0)$ line (see Section 2.3). Alternatively, if the density is insufficient to thermalise the $J = (3-2)$ transition, one may expect its excitation temperature to be lower than that of the $J = (1-0)$. The very low temperatures derived in the outer part suggest some sub-thermal excitation, at least for the $J = (3-2)$ transition beyond 400 au or so. Note that the apparent ‘ring-like’ distribution of HCO^+ $J = (3-2)$ is not due to simple excitation effect, as suggested by Cleeves et al. (2014a); a central hole of 50 au radius, almost fully devoid of HCO^+ , is required to reproduce the $J = (3-2)$ emission.

Table 4.2 Best-fit parameters for DM Tau.

PARAMETERS	HCO ⁺			DCO ⁺	
	$J = (1-0)$	$J = (3-2)$	SIMULTANEOUSLY	$J = (3-2)$	CONTINUUM
V_{LSR} (km s ⁻¹)	6.05 ± 0.01	6.01 ± 0.02	[6.01]	6.00 ± 0.21	[6.01]
i (°)	34.0 ± 2.7	33.8 ± 0.5	[34]	34.5 ± 2.1	[34]
PA (°)	64.31 ± 0.57	65.7 ± 3	[65]	65.9 ± 1.3	[65]
V_{100} (km s ⁻¹)	2.06 ± 0.10	2.16 ± 0.05	[2.1]	[2.1]	[2.1]
R_{int} (au)	-	53 ± 7	49 ⁺⁴ ₋₃	70 ± 20	-
R_{out} (au)	[750]	510 ± 5	[800]	427 ± 10	173.5 ± 0.3
dV (km s ⁻¹)	0.17 ± 0.01	0.14 ± 0.02	-	0.22 ± 0.44	[0.15]
h_{100} (au)	[16.5]	[16.5]	[16.5]	[16.5]	[16.5]
T_{100} (K)	11.3 ± 0.2	19.0 ± 0.2	33.6 ^{+1.5} _{-1.4}	[17]	19.07 ± 0.04
q -	0.34 ± 0.04	0.46 ± 0.04	1.00 ± 0.04	[0.43]	0.44 ± 0.03
Σ_{100} (cm ⁻²)	(1.9 ± 0.8) × 10 ¹⁴	[2.00 × 10 ¹⁴]	(9.8 ^{+0.3} _{-0.6}) × 10 ¹²	(1.2 ± 0.7) × 10 ¹²	(2.2 ± 0.66) × 10 ²³
p -	2.6 ± 0.8	[2.5]	0.82 ± 0.06	0.44 ± 0.11	0.61 ± 0.05

Note: Best fit parameters from the DiskFit modelling. Values in square brackets were fixed during the fitting.

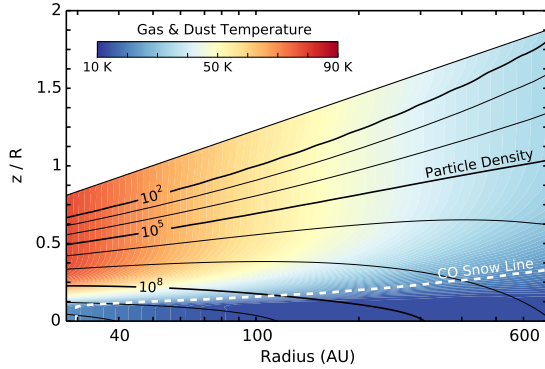


Figure 4.2 Disk physical structure scaled vertically as z/R . Colouring shows the coupled gas and dust temperature and solid lines show the particle number densities in particles per cubic centimetre. The dashed white line shows the 21 K isotherm, below which half of CO has frozen out.

As the DCO^+ line is weaker, a surface density can only be fit for by fixing all other parameters, guided by those found for HCO^+ . Given the molecules are chemically similar, it is a reasonable assumption to assume they are co-spatial in the disk. Note, however, that the derived values are quite insensitive to the assumed temperature law.

To provide a better comparison with the modelled results in the following sections, the power laws describing column densities and temperatures will be extrapolated across the range 10 to 700 au. However it must be noted that, due to the inner hole in HCO^+ and smaller outer radius in DCO^+ , the power laws only provide a good description of the observational data in the region between 50 and 430 au.

4.3 Chemical Modelling

To provide a comparison for the model found through the parametric model fitting, a suite of chemical models was run using the *ALCHEMIC* code, as described in Section 2.2.

Physical Structure

This section describes the methodology of creating a computational chemical disk model for DM Tau, including a description of the physical and chemical parameters used.

The DM Tau system, at a distance of 140 pc, consists of a single isolated pre-main-sequence M 0.5-1.5 dwarf ($T_{\text{eff}} = 3720$ K), with a mass of $0.5 - 0.65 M_{\odot}$, a radius of $1.2 R_{\odot}$, and an accretion rate of $2 - 3 \times 10^{-9} M_{\odot} \text{ yr}^{-1}$ (Mazzitelli, 1989; Simon et al., 2000; McJunkin et al., 2014). It is enshrouded by an extended (~ 800 au), cold ($T \gtrsim 10$ K) Keplerian disk (Piétu et al., 2007). According to the *Spitzer* IRS observations (Calvet et al., 2005), the inner DM Tau disk is cleared of small dust ($\lesssim 3 - 4$ au) and is in a pre-transitional phase. As our interferometric observations have the highest sensitivity in disk regions ≥ 30 au from the central star, we only consider the chemical evolution outside of this radius in our analysis.

The DM Tau physical disk model is based on a 1+1D steady-state α -model similar to that of D’Alessio et al. (1999), where equal gas and dust temperatures are assumed. This model has been extensively used in previous studies of DM Tau-like disk chemistry (e.g., Henning et al., 2010; Semenov & Wiebe, 2011; Albertsson et al., 2014). The disk model has an outer radius of 800 au, an accretion rate of $2 \times 10^{-9} M_{\odot} \text{ yr}^{-1}$, a viscosity parameter

$\alpha = 0.01$, and a total gas mass of $0.066 M_{\odot}$ (Dutrey et al., 2007; Henning et al., 2010; Semenov & Wiebe, 2011). The dissociating UV radiation of DM Tau is represented by the scaled-up interstellar UV radiation field of Draine (1978). The unattenuated stellar UV intensity at the radius of 100 au is $\chi_*(100) = 410$ (e.g., Bergin et al., 2003). The X-ray luminosity of DM Tau is taken to be $2 \times 10^{29} \text{ erg s}^{-1}$ (see Semenov & Wiebe, 2011). The calculated disk thermal and density structure is shown in Fig. 4.2.

Chemistry

The chemical model utilizes the high-temperature, gas-grain deuterium chemistry network of Albertsson et al. (2013), with the addition of nuclear spin-state processes for H_2 , H_2^+ , and H_3^+ isotopologues from Albertsson et al. (2014). The chemical network, without deuterated species, is based on the osu.2007 ratefile², with the recent updates to the reaction rates from KIDA (Wakelam et al., 2012). For all H-bearing reactions in this network, the corresponding D-bearing reactions were derived following the algorithm of Rodgers & Millar (1996). The cloning was not allowed for any species with the -OH end-group.

Primal isotope exchange reactions for H_3^+ as well as CH_3^+ and C_2H_2^+ from Roberts & Millar (2000); Gerlich et al. (2002); Roberts et al. (2004); Roueff et al. (2005) were included. In cases where the position of the deuterium atom in a reactant or in a product was ambiguous, a statistical branching approach was used. This deuterium network was further extended by adding ortho- and para-forms of H_2 , H_2^+ and H_3^+ isotopologues and the related nuclear spin-state exchange processes from several experimental and theoretical studies (Gerlich, 1990; Gerlich et al., 2002; Flower et al., 2004, 2006; Walmsley et al., 2004; Pagani et al., 2009; Hugo et al., 2009; Honvault et al., 2011; Sipilä et al., 2013).

To calculate UV ionization and dissociation rates, the mean FUV intensity at a given disk location is obtained by summing up the stellar $\chi_*(r) = 410 \times (r/100)^{-2}$, where r is in au, and interstellar UV fluxes scaled down by the visual extinction in the radial and vertical directions, respectively. Several tens of newer photoreaction rates are adopted from van Dishoeck et al. (2006)³. The self-shielding of H_2 from photodissociation is calculated by Eq. (37) from Draine & Bertoldi (1996). The shielding of CO by dust grains, H_2 , and the CO self-shielding is calculated using a precomputed table of Lee et al. (1996, Table 11).

The stellar X-ray radiation is modeled using observational results of Glassgold et al. (2005) and the approximate expressions (7–9) from the 2D Monte Carlo simulations of Glassgold et al. (1997a,b). Implementing Eqn. (8) from Glassgold et al. (1997b), we use an exponent of $n = 2.81$, a cross section at 1 keV of $\sigma_{-22} = 0.85 \times 10^{-22} \text{ cm}^2$ and total X-ray luminosity of $L_{\text{XR}} = 3 \times 10^{29} \text{ erg s}^{-1}$, yielding a typical X-ray photon energy of 3 keV. Attenuation of X-rays is calculated from Eqn. (4) in Glassgold et al. (1997a). The X-ray emitting source is located at 12 stellar radii above the midplane with rates exceeding that of the CRPs in the disk regions above the midplane, particularly, at radii $\sim 100 - 200 \text{ au}$ (see also Henning et al., 2010)

²<http://www.physics.ohio-state.edu/~eric/research.html>

³<http://www.strw.leidenuniv.nl/~ewine/photo>

Table 4.3

INITIAL ABUNDANCES FOR TMC1 CLOUD MODELLING									
ortho-H ₂	3.75(-1)	He	9.75(-2)	O	1.80(-4)	Na	2.25(-9)	P	2.16(-10)
para-H ₂	1125(-1)	C	7.86(-5)	S	9.14(-8)	Mg	1.09(-8)	Cl	1.00(-9)
HD	1.55(-5)	N	2.47(-5)	Si	9.74(-9)	Fe	2.74(-9)		

Note: Read $a(b)$ as $a \times 10^b$.

Table 4.4

MOST ABUNDANT SPECIES AFTER TMC1 CLOUD MODELLING									
para-H ₂	3.77(-01)	CO*	4.05(-05)	NH ₃ *	5.64(-06)	H*	6.03(-07)	NO	2.22(-07)
ortho-H ₂	1.23(-01)	CO	3.26(-05)	O	5.59(-06)	C ₃ H ₂ *	4.48(-07)	N	1.36(-07)
He	9.75(-02)	O ₂	1.79(-05)	O ₂ *	4.12(-06)	OH	3.43(-07)	HDO*	1.35(-07)
H	5.25(-04)	HD	1.52(-05)	CH ₄ *	3.64(-06)	H ₂ O	2.79(-07)	CO ₂	1.32(-07)
H ₂ O*	5.53(-05)	N ₂	7.39(-06)	N ₂ *	1.76(-06)	HNO*	2.40(-07)	CO ₂ *	1.19(-07)

Note: Read $a(b)$ as $a \times 10^b$. Molecules marked with * are ices.

A standard CRP ionization rate of $\zeta_{\text{CR}} = 1.3 \times 10^{-17} \text{ s}^{-1}$ was assumed with the attenuation modelled using Eq. (3) from [Semenov et al. \(2004\)](#). Note that the scattering of low energy CRPs by the heliosphere of DM Tau was not considered, as done in [Cleeves et al. \(2013a\)](#). Ionization due to the decay of SLRN is taken into account, $\zeta_{\text{RN}} = 6.5 \times 10^{-19} \text{ s}^{-1}$ ([Finocchi et al., 1997](#)), see also [Cleeves et al. \(2013b\)](#).

The grain ensemble used to calculate disk physical structure was represented by uniform amorphous silicate particles of olivine stoichiometry with density of 3 g cm^{-3} and radius of $0.1 \mu\text{m}$. Each grain provides $\approx 1.88 \times 10^6$ surface sites ([Biham et al., 2001](#)) for surface recombination that proceeds solely through the classical Langmuir-Hinshelwood mechanism (e.g. [Hasegawa et al., 1992](#)). The gas-grain interactions include sticking of neutral species and electrons to dust grains with 100% probability and desorption of ices by thermal, CRP-, and UV-driven processes. We do not allow H₂ to stick to grains as it requires temperatures of $\lesssim 4 \text{ K}$. The UV photodesorption yield of 3×10^{-3} was adopted (e.g., [Öberg et al., 2009a,b](#); [Fayolle et al., 2011, 2013](#)). Photodissociation processes of solid species are taken from [Garrod & Herbst \(2006\)](#); [Semenov & Wiebe \(2011\)](#).

In addition, dissociative recombination and radiative neutralization of molecular ions on charged grains and grain re-charging are taken into account. Upon a surface recombination, we assume there is a 1% probability for the products to leave the grain due to the partial conversion of the reaction exothermicity into breaking the surface-adsorbate bond ([Garrod et al., 2007](#); [Vasyunin & Herbst, 2013](#)). Following experimental studies on the formation of molecular hydrogen on amorphous dust grains by [Katz et al. \(1999\)](#), the standard rate equation approach to the surface chemistry was utilized. Overall, the disk chemical network consists of 1268 species made of 13 elements and 38,812 reactions.

The age of the DM Tau system is poorly constrained, $\sim 3\text{--}7 \text{ Myr}$ ([Simon et al., 2000](#)). In the chemical modeling the age of 5 Myr was considered. To set initial abundances,

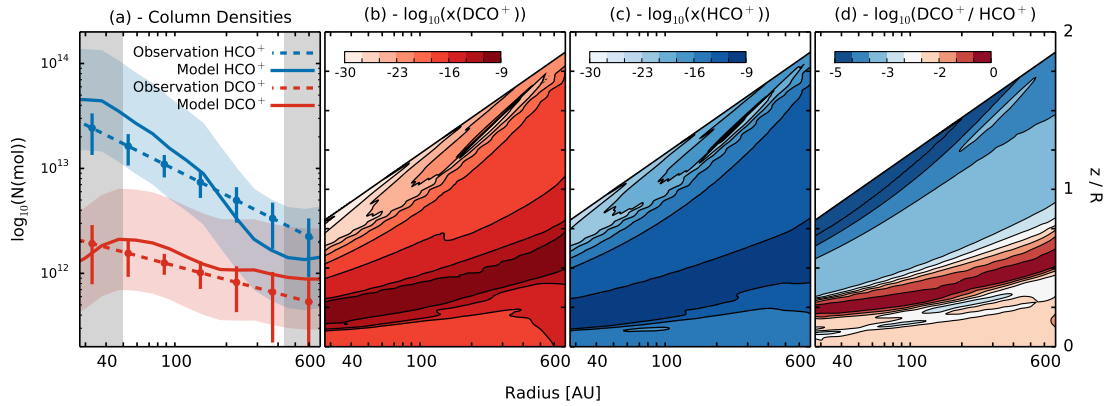


Figure 4.3 Deuterium fractionation in the disk. (a) Comparisons of HCO^+ , blue, and DCO^+ , red, from observations, dashed with 3σ errors, and the best fit model, solid with associated error of a factor of 3. They grey vertical bars show where the observationally derived column densities are extrapolated beyond the inner and outer edges found in parameterisation. (b) and (c) show the relative abundances of DCO^+ and HCO^+ in the best fit disk chemical model respectively. (d) shows the local $R_{\text{D}}(\text{HCO}^+)$ value in the disk model.

the chemical evolution in a TMC1-like molecular cloud ($n_{\text{H}} = 2 \times 10^4 \text{ cm}^{-3}$, $T = 10 \text{ K}$, $A_{\text{V}} = 10 \text{ mag}$) was calculated for 1 Myr. For that, the ‘low metals’ elemental abundances of [Graedel et al. \(1982\)](#); [Lee et al. \(1998\)](#); [Agúndez & Wakelam \(2013\)](#) were used, with the equilibrium 3:1 ortho/para H_2 ratio (hydrogen being fully in molecular form) and deuterium locked in HD molecule. The pre- and post-molecular cloud abundances are shown in Tables 4.3 and 4.4, with the later being used as initial abundances for the disk model.

Modelled Results

Figure 4.3a presents the modelled column densities for HCO^+ and DCO^+ in DM Tau (dashed lines) and associated 3σ errors with the observationally derived values (solid lines) overlain. Both column densities agree well within their errors. The grey boxes in Fig. 4.3 show where the power-law column densities are extrapolated beyond the radii where they were observed as to provide a better comparison with the chemical model which does not reproduce the inner hole.

Figures 4.3b and c show the relative abundance with respect to H_2 of DCO^+ and HCO^+ throughout the disk. These clearly demonstrate the stratification of the disk with a distinct molecular layer lying ~ 0.5 pressure scale heights above the midplane. Both molecular layers are relatively co-spatial, in general tracing regions of high gas phase CO abundance. They are bounded by the CO snowline towards the midplane, and the photodissociation region of CO towards the disk atmosphere. DCO^+ occupies a slightly tighter vertical range than HCO^+ due to it also requiring efficient deuteration. The molecular layer is truncated upwards due to the higher gas temperatures, reducing the efficiency of deuterium fractionation, while the lower bound is due to reduced HD abundances with which to readily transform deuterium into DCO^+ .

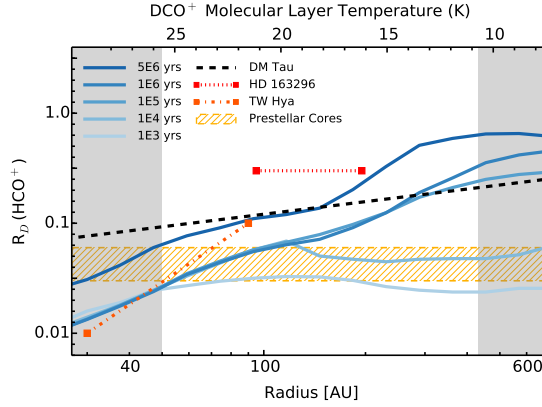


Figure 4.4 Comparisons of $R_D(\text{HCO}^+)$ values. The dashed black line shows the observationally derived value in DM Tau and the blue solid lines show the chemical model values at different time steps. Typical errors are a factor of 3. The grey vertical bars show where the observationally derived column densities of HCO^+ and DCO^+ are extrapolated beyond the inner and outer edges found in parameterisation. The orange dash-dotted line shows the value observed in TW Hya (Qi et al., 2008), the red dotted line, $R_D(\text{HCO}^+)$ in HD 163296 (Mathews et al., 2013), and the yellow dashed region, values from a survey of prestellar cores (Butner et al., 1995). The top y-axis shows the temperature of the DCO^+ layer derived from our parametric fitting.

$R_D(\text{HCO}^+)$, the ratio of the density, either column or volume, of a deuterated isotopologue to the undeuterated isotopologue, is shown in Fig. 4.3d with local values reaching as high as ~ 1 . Within this region we see pronounced increases of HD and H_2D^+ abundances facilitating a fast transfer of deuterium from HD to DCO^+ . Despite these locally high values, the vertically integrated column density is more sensitive to the denser regions closer to the midplane, thereby exhibiting a lower value of $R_D(\text{HCO}^+) \sim 0.1$.

Figure 4.4 shows the modelled values of R_D at various time steps in the model (blue lines). The observationally derived value, shown by the black dashed line, agrees qualitatively well with the $t = 5 \times 10^6$ yrs value.

4.4 Discussion

In this section the observationally-derived and best-fit modelled column densities are compared, complemented with a further suite of chemical models, to explore both deuterium fractionation and the ionization fraction in the disk.

Deuterium Fractionation of HCO^+

Although deuterium fractionation is typically used as a probe of the thermal history of an environment, other chemical processes could alter $R_D(\text{HCO}^+)$, biasing the understanding of the thermal history. In this section a range of physical parameters, other than temperature, are varied to understand their impact on the observed $R_D(\text{HCO}^+)$ values.

Figure 4.4 shows the radial profile of R_D found for DM Tau observationally (dashed black line) and at various time steps in the model, $t = \{10^3, 10^4, 10^5, 10^6, 5 \times 10^6\}$ yrs (solid

blue lines). Also marked are values for TW Hya (orange dash-dotted line; Qi et al. (2008)), HD 163296 (red dotted line; Mathews et al. (2013)) and an average of prestellar cores (yellow hatched region; Butner et al. (1995); Caselli et al. (2002)). Enhanced values relative to the cosmic abundance of $[D]/[H] \sim 10^{-5}$ are indicative of continued gaseous processing in a cold, $T \lesssim 20 - 30$ K, environment; a none too surprising conclusion given the kinetic temperature probed by the line emission, $T \sim 10 - 20$ K (see Table 4.2). Furthermore, the radial increase is to be expected due to the radial temperature gradient in a disk. That is, the pace of deuterium fractionation and synthesis of the H_3^+ isotopologues hastens in colder outer disk regions. In turn, higher abundances of the H_3^+ isotopologues imply more efficient formation of DCO^+ in ion-molecule reactions with gaseous CO, increasing R_D .

Our R_D values, ranging from $\approx 0.1 - 0.2$ between 50 au and 430 au, are almost two orders of magnitude higher than the disk average value of $(4.0 \pm 0.9) \times 10^{-3}$ found by Guilleloteau et al. (2006), who used HCO^+ $J = (1 - 0)$ interferomic data and DCO^+ $J = (3 - 2)$ single dish data. This discrepancy can be explained by the assumptions made in the calculation of HCO^+ and DCO^+ column densities. Firstly, it was assumed that DCO^+ was radially co-spatial with the HCO^+ emission which extends out to ~ 800 au, an outer radii similar to that of CO. This increased emitting region would result in a lower, disk average value for DCO^+ , reducing R_D . Secondly, we have shown that HCO^+ likely exhibits a complex molecular distribution including an inner hole in emission. When fitting a single transition this complexity was found to drive the parameterisation to favour steeper power laws describing column densities, consistent the HCO^+ $J = (1 - 0)$ data from Piétu et al. (2007), yielding a much smaller R_D value in the inner disk than found with our data.

In TW Hydrae, another well studied protoplanetary disk, the value of R_D has been measured both as a disk average (0.035 ± 0.015 , van Dishoeck et al. (2003)), and with spatially resolved interferomic observations yielding a value from 0.01 to 0.1 between 30 and 90 au (Qi et al., 2008). The increase found in the outer regions of the disk when moving to spatially resolved data is consistent with our findings in DM Tau. Similarly, while the TW Hya disk is smaller and less massive than DM Tau, it appears to hold comparable values for R_D at similar distances to the star, namely around ~ 0.1 at 100 au. More recently, Mathews et al. (2013) used ALMA science verification data of HD 163296, an A1 spectral type Herbig Ae star and comprehensive modeling to ascertain local values of $R_D \sim 0.3$ and a disk average of 0.02. Typically disks around Herbig Ae stars are warmer and more massive than those around classical T-Tauri stars, thus a reduced disk average value of R_D is to be expected.

Figure 4.4 also clearly shows continued enhancement of R_D up to ~ 1 Myr, indicative of continued processing of the gaseous CO during a disk lifetime. Thus, it is of no surprise that the observed value of R_D in DM Tau, thought to be between 3 – 7 Myr, is higher than that found in low-mass prestellar cores (0.045 ± 0.015 , Butner et al., 1995).

Molecular layers in a protoplanetary disk are far beyond closed systems. Measurements of R_D through the ratio of column densities are sensitive to more than just the deuterium fractionation efficiency, but are compounded by physical parameters which can

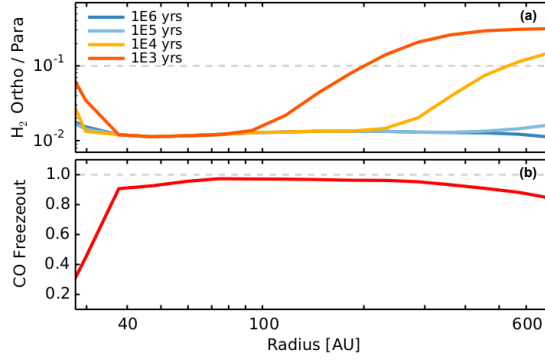


Figure 4.5 Shown in the top panel is the ratio of column densities of ortho- H_2 and para- H_2 from the best fit model. After $\sim 10^5$ yrs the ratio reaches a steady state. (b) Showing the degree of CO freeze out in our model quantified as the ratio of column densities of CO ice and gaseous CO. This clearly demonstrating the CO ice line at $r \approx 30$ au.

alter the abundances of HCO^+ and DCO^+ . In the remainder of this section it is explored how else the physical environment can change the observed value of R_D by running a suite of chemical models and varying a single parameter. This will aid in analysis when comparing values of R_D from different astrophysical environments.

H_2 ortho-to-para ratio (OPR)

As discussed previously, deuterium fractionation occurs due to the energy difference between deuterium and hydrogen atoms, thereby resulting in the deuteration of H_3^+ by HD to be exothermic. Low energy environments are therefore conducive to enhanced abundances of deuterated isotopologues resulting from successive deuteration of H_3^+ . For H_2 , ΔE corresponds to $T_{\text{kin}} \approx 30$ K resulting in inefficient fractionation above this temperature. This is clearly evident in both observational and modelled results (see Fig. 4.4) which show an increase in R_D at larger radii where the disk is cooler.

Furthermore, the larger internal energy of ortho- H_2 relative to para- H_2 results in a higher frequency of back reactions in Eqn. 4.3 if H_2 is predominantly ortho-. It has been shown that $\text{OPR} \gtrsim 0.1$ can limit the overall fractionation efficiency, even when the kinetic temperatures are low. Proton exchange due to collisions will reduce the canonical H_2 OPR of ~ 0.75 . A reduced OPR will increase the efficiency of deuterium fractionation, see Fig 4.5a (Pagani et al., 1992, 2009, 2013; Crabtree et al., 2011; Albertsson et al., 2014). However, the relatively high densities of the molecular layer in a disk ensure that this is a relative quick process, taking $\sim 10^5$ yrs.

Gas-Phase CO Abundance

As a parental molecule of both HCO^+ and DCO^+ , the CO abundance is intimately linked to the abundances of HCO^+ and DCO^+ . Gaseous CO must be sufficiently abundant to efficiently convert the H_3^+ and H_2D^+ into HCO^+ and DCO^+ respectively. However, CO readily freezes out at $T \approx 21$ K, vastly reducing the available reaction partners, see Fig 4.5b. Therefore, DCO^+ is most efficiently produced where temperatures are high enough to

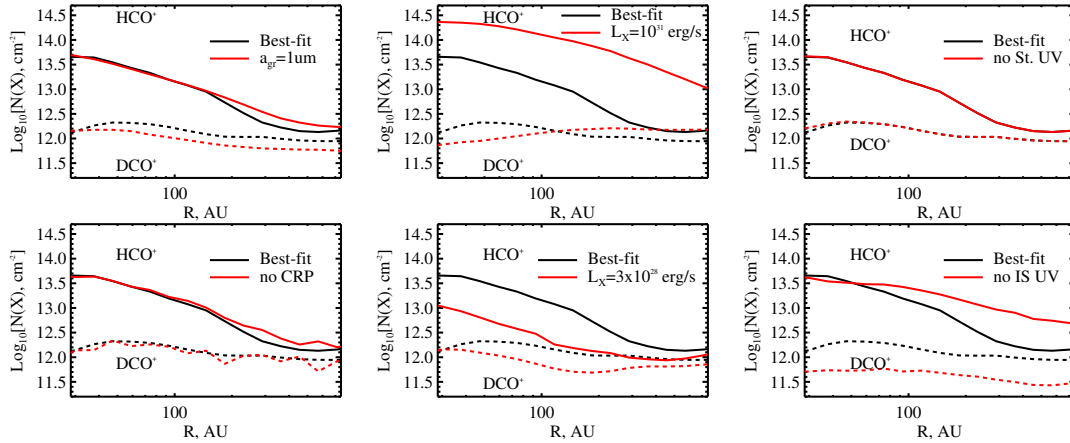


Figure 4.6 Computed molecular column densities for DCO^+ (dashed line) and HCO^+ (solid line). Black lines show the columns obtained with the best-fit model described in Section 4.3, red lines show the columns when the specified physical parameter is changed in the best fit model while the others are held constant. From the top left panel, in a clockwise fashion, these are: increased grain size, increased X-Ray luminosity, no interstellar UV flux, no CRPs and no stellar UV flux. For reference, the canonical model has a single grain population of $a = 0.1 \mu\text{m}$, $L_X = 3 \times 10^{29} \text{ erg s}^{-1}$, $\chi_*(100 \text{ au}) = 410$ and a CRP ionization rate of $\zeta = 1.3 \times 10^{-17} \text{ s}^{-1}$.

maintain a relatively low level of CO depletion, yet cool enough to allow efficient fractionation. This is visible in Fig. 4.3a where $N(\text{DCO}^+)$ peaks around 50 au.

For the same mass of dust, larger grains have a reduced surface area onto which CO can freeze out, reducing the depletion of CO and hence expanding its molecular layer towards the disk midplane. Fig. 4.6 shows the change in $N(\text{HCO}^+)$ and $N(\text{DCO}^+)$ when the grain size in our best fit model is increased to $1 \mu\text{m}$. Outside the CO snowline $N(\text{HCO}^+)$ is enhanced due to the greater availability of CO to react with H_3^+ resulting in a shallower gradient. On the other hand, $N(\text{DCO}^+)$ is uniformly decreased. The decrease of DCO^+ abundances is associated with less efficient fractionation of H_3^+ in its molecular layer. Rapid ion-molecule reactions of H_3^+ with volatile molecules such as CO, which are less depleted from the gas phase, compete with fractionation processes and hence lower production of deuterated H_3^+ isotopologues. This results in a reduced R_D as a disk average and a weaker radial gradient.

Ionization

The other parental molecules of HCO^+ and DCO^+ are H_3^+ and H_2D^+ respectively, both of which require the ionization of H_2 . Fig. 4.6 shows how the column densities are affected when ionization sources in the best fit model are altered.

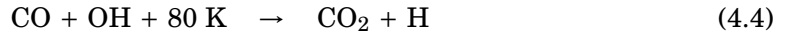
Clearly shown in the top left and top right panels of Fig. 4.6, stellar UV and CRPs play little role in the abundance of these two species. In the disk model, UV scattering is neglected therefore the stellar UV radiation becomes quickly absorbed in radial direction by the dust, thus making little impact on the abundance of HCO^+ and DCO^+ . Additionally, high energy CRPs can penetrate to the molecular layers, however they have such a low flux that they are of little consequence in the life-cycle of HCO^+ and DCO^+ .

Conversely, the abundances of HCO^+ and DCO^+ are sensitive to the stellar X-rays, the dominant ionization source in the molecular layer. Increased values of L_X lead to an enhanced abundance of HCO^+ across the entire disk. DCO^+ production is suppressed in the inner disk, $r \lesssim 100$ au, while outer regions display an enhancement. The DCO^+ production is suppressed in the inner disk despite an increase in overall H_3^+ isotopologue abundances within the inner molecular layer due to an increased H_2 -OPR arising from the increased X-ray luminosity injecting sufficient energy into the disk for re-equilibration through ion-molecule and nuclear spin-state processes. The increased OPR of the H_3^+ isotopologues slows the overall pace of the deuterium fractionation. In addition, an increase of DCO^+ abundances in the outer disk is smaller than for HCO^+ because the DCO^+ layer is located deeper into the disk, where temperatures favour deuterium enrichment and are better shielded from impinging stellar X-ray photons than the more extended HCO^+ molecular layer.

Reducing the stellar X-ray luminosity reduced both the HCO^+ and DCO^+ abundances. This is a more pronounced effect in the inner disk due to the oblique angles of incident X-rays, as found in [Henning et al. \(2010\)](#). The higher sensitivity of HCO^+ to changing X-ray luminosities, again due to the difference in vertical extents of the molecular layers, is reflected in the gradient of R_D ; a lower L_X leads to a less radially dependent R_D . Additionally, HCO^+ production is suppressed to such a low level that R_D can reach ~ 1 in the outer disk.

A more puzzling result is the strong influence of interstellar UV radiation on R_D . In the disk model without an IS UV field, R_D becomes lower by up to an order of magnitude compared to the best-fit model. This is mainly due to a uniform decrease of the DCO^+ column density throughout the disk by a factor of ~ 3 , and an increase of the HCO^+ column density at $r \gtrsim 50 - 60$ au by a similar factor of about 3, producing a near constant R_D across the radius of the disk.

The IS UV photons play two main roles for disk chemical evolution. Firstly, they partly contribute to the ionization and dissociation of disk matter in the molecular layer, particularly beyond $r \gtrsim 100$ au. Secondly, and more importantly for R_D , they bring heavy ices back to the gas phase by photodesorption and thus partly regulate surface processes. We found that in the DM Tau model without IS UV radiation, CO gets more easily converted into CO_2 ice in the molecular layer at $T \lesssim 30 - 40$ K through the slightly endothermic reaction of,



CO_2 is unable to be photodesorbed and therefore partly dissociated in the gas. In addition, abundances of water ices increase, whereas abundances of atomic and molecular oxygen decrease. This leads to a drop in gas-phase CO abundances locally by a factor of 2–4 at all disk radii.

Furthermore, in the absence of photodesorption due to the absence of UV ionization, ions of alkali metals such as Na^+ and Mg^+ , along with atomic ions such as S^+ and C^+ , become less abundant and do not contribute considerably to the fractional ionization of the

entire molecular layer. As a result, polyatomic ions like HCO^+ and H_3O^+ dominate the ionization structure, resulting in a decrease by a factor of a few in ionization fraction due to their more efficient recombination with electrons. These two factors, lower ionization degree and lower CO abundances, lead to both lower DCO^+ abundances in the molecular layer and also reduced DCO^+ column densities.

Contrary to DCO^+ , HCO^+ abundances and column densities show an increase at $r \gtrsim 50$ au in the DM Tau model without IS UV. This is related to the fact that the DCO^+ molecular layer is narrower and located more deeply in the disk compared to the HCO^+ molecular layer. The lack of photodesorption and photodissociation in the upper part of the HCO^+ molecular layer increases abundances of CO and H_3^+ isotopologues, hence boosting production of HCO^+ . This compensates for the decrease of gaseous CO due to its surface conversion into the CO_2 ice in the lower part of the HCO^+ molecular layer.

Comparisons with previously published models highlight the importance of considering these additional processes which alter the abundance of HCO^+ and DCO^+ . Despite the relatively well understood deuterium fractionation mechanism there are orders-of-magnitude disparity between models. [Aikawa et al. \(2002\)](#) modelled a smaller disk with gas extending on to 373 au which exhibited a radial dependence of R_D varying between 0.003 to 0.06, values more in accord with the smaller TW Hya disk. Whereas a newer model of [Willacy \(2007\)](#) found considerably higher values ranging from $R_D = 0.1$ at 50 au to reaching unity outside 100 au, suggesting high R_D values are to be expected.

Hence, while $R_D(\text{HCO}^+)$ provides an easily accessible measure of deuterium fractionation, a link through several environments in the cycle of molecular gas, other parameters, particularly the X-ray luminosity of the central star, the interstellar UV field and the grain evolution, are folded into this measurement. In the case of protoplanetary disks, the X-ray luminosity of the host star must be well constrained in order to fully characterise the deuterium fractionation present in the disk.

Ionization Fraction, $x(e^-)$

HCO^+ is often touted as the most dominant ion in the warm molecular layer of a protoplanetary disk. As such, it is frequently used as a proxy of the ionization in this region ([Semenov et al., 2004](#); [Dutrey et al., 2007](#); [Qi et al., 2008](#); [Öberg et al., 2011b](#)). However, the large radial and vertical gradients in physical parameters characteristic of a protoplanetary disk introduce several complications in deriving knowledge of the ionization fraction from a single charged species. Common practice therefore is to make a steady state approximation, a methodology that has been applied to a range of astrophysical scales: from protoplanetary disks to molecular clouds and supernova remnants ([Guelin et al., 1977](#); [Caselli et al., 2002, 2008](#); [Vaupré et al., 2014](#)).

Introduced by [Guelin et al. \(1977\)](#), this assumes a heavily reduced chemical network in a steady state of ionization. As discussed previously, the abundance of HCO^+ is largely governed by two main processes: creation through ion-neutral reactions between H_3^+ and CO and destruction via electronic recombination. Similar pathways hold for DCO^+ but

Table 4.5 Reaction Rates

REACTION	RATES	α (CM ³ S ⁻¹)	β	γ (K)
DEUTERATION				
$\text{H}_3^+ + \text{HD} \leftrightarrow \text{H}_2\text{D}^+ + \text{H}_2$	$k_{1,k-1}$	1.7×10^{-9}	0	220
$\text{H}_2\text{D}^+ + \text{HD} \leftrightarrow \text{D}_2\text{H}^+ + \text{H}_2$	$k_{2,k-2}$	8.1×10^{-10}	0	187
$\text{D}_2\text{H}^+ + \text{HD} \leftrightarrow \text{D}_3^+ + \text{H}_2$	$k_{3,k-3}$	6.4×10^{-10}	0	234
ION-MOLECULE				
$\text{H}_3^+ + \text{CO} \rightarrow \text{HCO}^+ + \text{H}_2$	k_{CO}	1.61×10^{-9}	0	-
$\text{H}_2\text{D}^+ + \text{CO} \rightarrow \text{HCO}^+ + \text{HD}$	k_{CO}	1.61×10^{-9}	0	-
$\text{H}_2\text{D}^+ + \text{CO} \rightarrow \text{DCO}^+ + \text{H}_2$	k_{CO}	1.61×10^{-9}	0	-
$\text{D}_2\text{H}^+ + \text{CO} \rightarrow \text{HCO}^+ + \text{D}_2$	k_{CO}	1.61×10^{-9}	0	-
$\text{D}_2\text{H}^+ + \text{CO} \rightarrow \text{DCO}^+ + \text{HD}$	k_{CO}	1.61×10^{-9}	0	-
$\text{D}_3^+ + \text{CO} \rightarrow \text{DCO}^+ + \text{D}_2$	k_{CO}	1.61×10^{-9}	0	-
RECOMBINATION				
$\text{H}_3^+ + e^- \rightarrow \text{various}$	k_{rec0}	6.8×10^{-8}	-0.5	-
$\text{H}_2\text{D}^+ + e^- \rightarrow \text{various}$	k_{rec1}	6.0×10^{-8}	-0.5	-
$\text{D}_2\text{H}^+ + e^- \rightarrow \text{various}$	k_{rec2}	6.0×10^{-8}	-0.5	-
$\text{D}_3^+ + e^- \rightarrow \text{various}$	k_{rec0}	2.7×10^{-8}	-0.5	-

Note: Reactions involved in the considered steady state system and the rates used in our modelling. Forward rates should be read as $\alpha(T/300)^\beta$ and backwards as $\alpha(T/300)^\beta \exp(-\gamma/T)$. Adapted from [Caselli et al. \(2008\)](#).

with the deuterated H_2D^+ in place of H_3^+ . [Caselli et al. \(2002\)](#) showed the chemical kinetics of such a network in steady state can be reduced to:

$$x(e^-) = \frac{1}{k_{\text{rec1}}} \left(\frac{k_1 x(\text{HD})}{3R_{\text{D}}} - k_3 x(\text{CO}) \right), \quad (4.5)$$

where the rates and associated reactions are found in Table 4.5.

Performing a steady-state analysis requires knowledge of both $x(\text{HD})$, a molecule which has only 4 observation of in a protoplanetary disk ([Bergin et al., 2013](#); [McClure et al., 2016](#)), and the total gas column, from which to convert from column density to relative abundances, a value that cannot be well constrained observationally without several assumptions ([Thi et al., 2010](#)). Application to DM Tau is thus limited to the case where one must assume values of $x(\text{CO})$ and $x(\text{HD})$. This methodology has since been expanded to include all multiply-deuterated isotopologues of H_3^+ and charged grains, however the lack of observational constraints on these would further compound the issues detailed above in the case of a protoplanetary disk ([Caselli et al., 2008](#)). Finally, it must be noted that physical parameters derived from line emission will be indicative of the molecular region and not applicable to the disk as a whole as discussed in Section 2.3.

Using the observationally derived R_{D} values with $x(\text{HD}) = 2.40 \times 10^{-5}$ and $x(\text{CO}) = 7.24 \times 10^{-5}$, taken from the best fit model and consistent with previous observations of DM Tau ([Piétu et al., 2007](#)), an ionization fraction of $x(e^-) \sim 10^{-7}$ if found. This is shown by the dashed black line in Fig. 4.7. This value is consistent with the lower limits placed

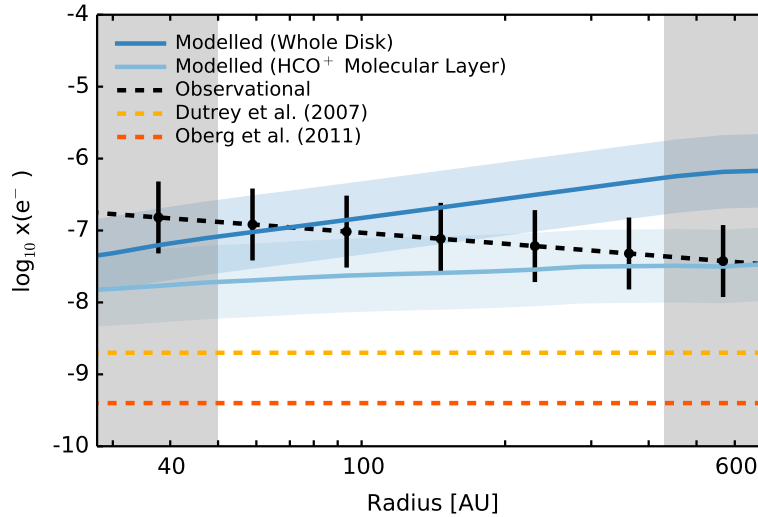


Figure 4.7 Constraints on the ionization fraction in DM Tau. Results from the steady state approximation are shown with: observational values, black dashed; modelled values from the entire disk, dark blue solid; modelled values from the HCO^+ molecular layer, light blue solid; lower limit from Dutrey et al. (2007), light orange solid and lower limit from Öberg et al. (2011b), dark orange solid. All errors, dominated by the values from the chemical modelling, are a factor of 3.

by Dutrey et al. (2007) (light orange) and Öberg et al. (2011b) (dark orange). Blue lines show $x(e^-)$ from the best fit model, the light blue considering molecular column densities integrated over the warm molecular layer probed by our HCO^+ and DCO^+ observations⁴, and those integrated over the whole disk in dark blue. Both of which qualitatively agree with the steady state values. Qi et al. (2008) found a similar ionization fraction of $x(e^-) \sim 10^{-7}$ in TW Hya, when using the same steady state approximation.

However, disk ionization is controlled by a myriad of atomic and molecular species, as shown by Fig 4.8. Panels *b* and *c* show the relative contribution of the top eight most abundant ions as a function of radius for the whole disk, *b*, and only in the HCO^+ molecular layer, *c*. It is clear that ionization as a whole is dominated by the atomic ions C^+ and H^+ which contribute $\gtrsim 99\%$ of the charge. Even within the molecular layer, atomic ions are the dominant charge carriers with S^+ , H^+ and C^+ contributing between 50% and 90% of the total charge. While HCO^+ is the dominant molecular ion, it contributes at most $\sim 20\%$ of the charge in the inner regions and is severely depleted in the outer disk, $r \gtrsim 200$ au. Thus, while HCO^+ is the most dominant *molecular* ion in the disk its contribution to total charge is dwarfed by that of atomic ions such as C^+ , H^+ and S^+ , even in the molecular layer.

This additional source of ionization not considered in the steady state approximation can contribute to the difference in observed values of $x(e^-)$. Furthermore, it is surprising that observations sensitive to only a small region in the disk are able to recover disk average values relatively well. This is due to the density gradient towards the midplane;

⁴Here the molecular layer of a molecule such that the column density of that molecule contained in it is equal to 90% of that molecule's total column density. It is centred at the position which has a largest fractional contribution to the total column density.

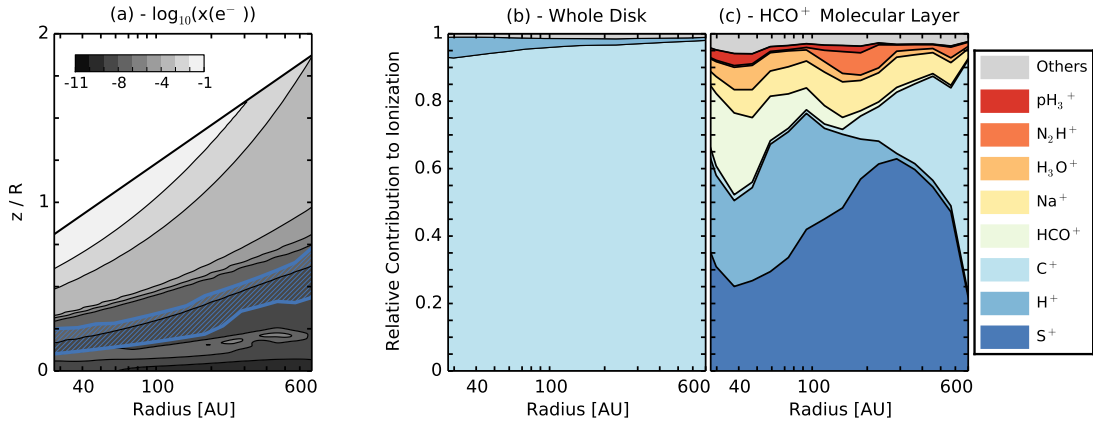


Figure 4.8 (a) Ionization structure of the DM Tau disk model. The region bounded by blue lines is what we have defined as the HCO^+ molecular layer. (b) and (c) Relative contributions of charged species to the ionization level over the whole disk and the HCO^+ molecular layer. As a disk average, panel (b), it is clear the charge is dominated by C^+ and H^+ , the gray region representing all other charged species. In the HCO^+ molecular layer, panel (c), defined as the region that contributes 90% of the total HCO^+ column density, HCO^+ supplies a majority of the charge with large contributions from H^+ , C^+ and S^+ .

the disk average will draw heavily from values closer to the midplane to the larger density weighting.

4.5 Summary

In this Chapter, PdBI observations of the abundant molecular ions HCO^+ , $J = (3 - 2)$, $(1 - 0)$ and DCO^+ , $J = (3 - 2)$ of DM Tau and a suite of chemical models were presented. These datasets provide the framework to study deuterium fractionation and the ionization fraction in DM Tau.

Using combined χ^2 -minimization and MCMC fitting techniques, a parametric model was fitted to the observations. HCO^+ was found to exhibit a complex emission structure. $J = (3 - 2)$ emission had a peak intensity at $r \approx 50$ au and was considerably less extended than the $J = (1 - 0)$ emission. HCO^+ $J = (1 - 0)$ emission was found to be co-spatial with CO emission (Piétu et al., 2007). An inner hole of $r \approx 50$ au in HCO^+ is needed to recreate the observations. By simultaneously fitting the $J = (3 - 2)$ and $(1 - 0)$ lines required the assumption that both lines had the same excitation temperature. DCO^+ emission was also tentatively found to peak at $r \approx 70$ au, consistent with the CO snowline, however higher resolution observations are required to confirm this.

DM Tau was found to have a $R_D(HCO^+)$ which varies from 0.1 to 0.2 between 50 and 430 au, values considerably higher than both the cosmic abundance $\sim 10^{-5}$ and those found in prestellar cores, 0.035 ± 0.015 . Such an enhancement is indicative of continued fractionation throughout the disk lifetime. Both TW Hya and HD 163296 exhibit similar high levels of deuteration, the later peaking at $R_D \sim 0.3$ (Qi et al., 2008; Mathews et al., 2013).

Through chemical modelling, the sensitivity of R_D on other physical parameters was

explored. The most influential parameters are the level of interstellar UV and the X-ray luminosity of the central star which are dominant ionization sources in the molecular layer (see also [Cleeves et al., 2015a](#)). X-rays impact R_D in a relatively straight forward manner: higher luminosities result in increased abundances of HCO^+ and DCO^+ and conversely for reduced luminosities. On the other hand, interstellar UV impacts R_D in a more complex manner as it does not directly affect HCO^+ and DCO^+ , but rather the CO abundances. This results in an enhancement of DCO^+ abundances across the entire disk, while suppressing the formation of HCO^+ in the outer, $r \gtrsim 50$ au, disk. These effects can be disentangled through the dependence of R_D on radius with the later producing a more radially constant value of R_D .

Assuming a steady state system one can estimate the electron fraction of the HCO^+ molecular layer to be $x(e^-) \sim 10^{-7}$, consistent with lower limits from [Dutrey et al. \(2007\)](#) and [Öberg et al. \(2011b\)](#). This values is high enough to induce MRI turbulence. An analysis of the dominant charge carries in the molecular layer show that HCO^+ is the most dominant *molecular* ion, however atomic ions are considerably more dominant in all regions of the disk. Thus constraints on ionization from the abundance of HCO^+ must take this into account.

Measuring Turbulence in TW Hya

Based on [Teague et al. \(2016\)](#), published in *Astronomy & Astrophysics*.

5.1 Motivation

Turbulent motions underpin the entire evolution of a protoplanetary disk. Foremost, turbulence determines the bulk gas viscosity and hence regulates the angular momentum transport and accretion in disks ([Shakura & Sunyaev, 1973](#); [Pringle, 1981](#)). Secondly, turbulence is a key factor for dust evolution and transport in disks ([Testi et al., 2014](#); [Henning & Meeus, 2011](#)). However, until recently, observational constraints on the level of disk turbulence were extremely challenging to obtain and hence scarce. With the advent of the ALMA, we have access for the first time to observations with the high sensitivity and spectral and angular resolutions that are needed to directly measure turbulent velocities in disks.

Accurate determination of the turbulent velocity dispersion from line broadening requires a good understanding of the other components that contribute to the line width, namely bulk motions of the gas, thermal broadening and, in the case of a highly optically thick line, broadening due to the line opacity. All previous measurements of v_{turb} have revolved around the fitting of a parametric model to extract a disk-averaged turbulent broadening value. The derived values ranged from very low values of $\lesssim 10 - 100 \text{ m s}^{-1}$ ($\lesssim 0.02 - 0.2 c_s$) derived for the TW Hya and HD 163296 disks, to higher velocities of $\lesssim 100 - 200 \text{ m s}^{-1}$ ($\lesssim 0.3 - 0.5 c_s$) for the disks of DM Tau, MWC 480 and LkCa 15 ([Dartois et al., 2003](#); [Piétu et al., 2007](#); [Hughes et al., 2011](#); [Rosenfeld et al., 2012](#); [Flaherty et al., 2015](#)). With the exception of TW Hya and HD 163296 ([Hughes et al., 2011](#); [Flaherty et al., 2015](#)), the spectral resolution of the data used to determine these values, of the order $\sim 200 \text{ m s}^{-1}$, is too coarse to resolve the small expected contribution from turbulent broadening, although [Guilloteau et al. \(2012\)](#) did correct for this effect when using CS to measure turbulence in DM Tau.

High-quality ALMA Cycle 2 observations of TW Hya allow us for the first time to obtain a direct measure of the line widths and thus of the spatially resolved turbulent

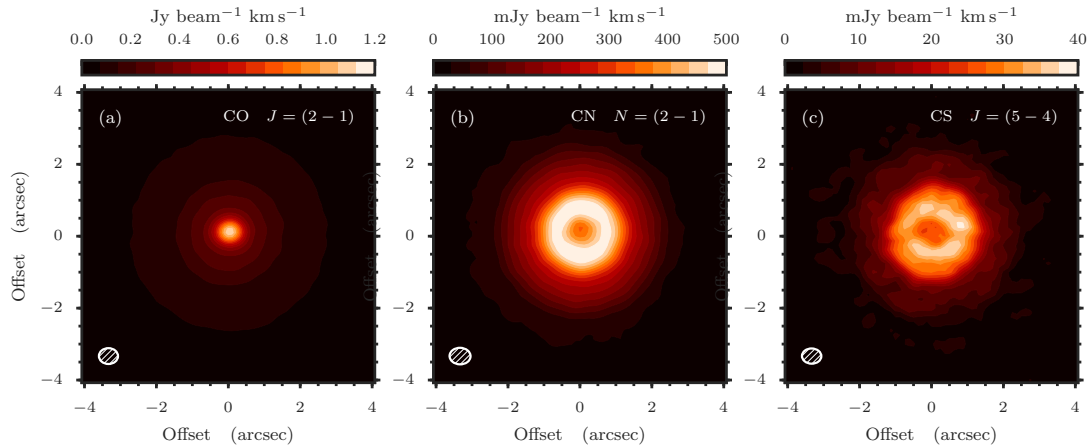


Figure 5.1 Zeroth moment maps of the observations.

velocity structure. With a nearly face-on inclination of only $i \approx 7^\circ$ (Qi et al., 2004) and as the nearest protoplanetary disk at $d \approx 54$ pc, TW Hya provides the best opportunity to directly detect turbulent broadening as the effect of Keplerian shear for such face-on disks is minimized compared to more inclined systems.

This Chapter presents first direct measurements of v_{turb} in a protoplanetary disk using line emission of CO, CN and CS. In Section 5.2, I describe the ALMA observations and the data reduction. Section 5.3 describes the methods used to extract v_{turb} , two direct methods, relying on a measure of the line widths, and a more commonly used method, the fitting of a parametric model as discussed in Section 3.3. Discussion of the results follow in Section 5.4.

5.2 Observations

The observations were performed using ALMA on May 13, 2015 under excellent weather conditions (Cycle 2, 2013.1.00387.S). The receivers were tuned to cover CO $J = (2 - 1)$, CS $J = (5 - 4)$ and all strong hyperfine components of CN $N = (2 - 1)$ simultaneously. The correlator was configured to deliver very high spectral resolution, with a channel spacing of 15 kHz (and an effective velocity resolution of 40 m s^{-1}) for the CO $J = (2 - 1)$ and CS $J = (5 - 4)$ lines, and 30 kHz (80 m s^{-1}) for the CN $N = (2 - 1)$ transition.

Data were calibrated using the standard ALMA calibration script in the CASA software package¹. The calibrated data were re-gridded in velocity to the LSR frame, and exported through UVFITS format to the GILDAS² package for imaging and data analysis. Self-calibration was performed on the continuum data, and the phase solution was applied to all spectral line data. With robust weighting, the uv -coverage, which has baselines between 21 and 550 m, provided by ~ 34 antennas, yields a beam size of $0.50'' \times 0.42''$ at a position angle of 80° . The absolute flux calibration was made with reference to Ganymede. The derived flux for our amplitude and phase calibrator, J1037-2934, was

¹<http://casa.nrao.edu/>

²<http://www.iram.fr/IRAMFR/GILDAS>

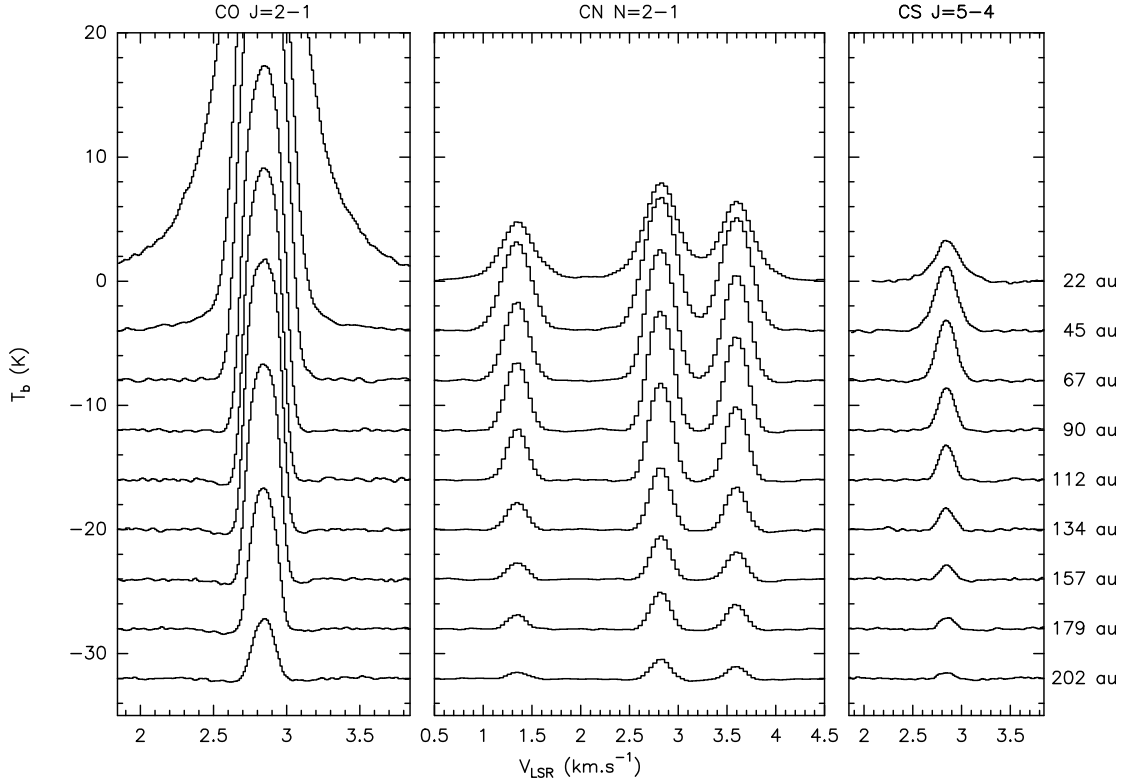


Figure 5.2 Examples of the azimuthally averaged spectra for CO, *left*, CN, *centre* and CS, *right*. The radial offsets show different radial positions in the disk, separated by roughly a beam width. For the full compliment of CN hyperfine components, see Appendix A.

0.72 Jy at 228 GHz at the time of the observations, with a spectral index $\alpha = -0.54$, while the ALMA flux archive indicated a flux of 0.72 ± 0.05 Jy between April 14 and April 25. It is therefore estimated that the calibration uncertainty is about 7%.

After deconvolution and primary beam correction, the data cubes were imported into the GILDAS package CLASS for further analysis, in particular line profile fits including the hyperfine structure for CN lines. For the azimuthal averaging, each spectrum was shifted in velocity from its local projected Keplerian velocity to the local systemic velocity before averaging. For this the best-fit Keplerian model, assuming a stellar mass of $0.69 M_{\odot}$ and $i = 7^{\circ}$, was used, see Sect. 5.3.

All three emission lines show azimuthal symmetry within the noise justifying our choice to azimuthally average the data (see Chapter 6 for a thorough analysis of the imaged data). Examples of the resulting spectra are displayed in Fig. 5.2 for the three molecules, the vertical offsets showing different radial positions, separated by a beam width.

5.3 Separating Turbulent Velocity Dispersions

Turbulent motions within a gas manifest themselves as a velocity dispersion along the line of sight, broadening the width of the emission (or absorption) line. This broadening term acts in tandem with thermal broadening, a contribution typically an order of

magnitude larger than the turbulent width. Additionally, the Keplerian shear across the beam will broaden the observed emission lines. This effect is the most dominant in the inner disk and for highly inclined disks, making TW Hya an ideal source as this effect is minimized.

In the following section three methods are discussed for disentangling v_{turb} , the turbulent velocity dispersion, from the total linewidth. These contain two direct methods, assuming as little as possible about the disk physical structure, and one parametric approach, where the physical structure of the disk is assumed to be well described by radial power-law profiles.

Line Width Measurement

Physical parameters were extracted from the line profiles at each pixel in the image and for an azimuthal average. As described in Section 3.2, with typical local linewidths of $\approx 400 \text{ m s}^{-1}$ sampled at a spectral resolution of $\approx 40 \text{ m s}^{-1}$ and a noise level of $\sigma_{\text{noise}} \lesssim 0.01$, a fit to a Gaussian profile would recover a linewidth accurate to $\lesssim 3\%$, or $\sim 10 \text{ m s}^{-1}$. Following [Lenz & Ayres \(1992\)](#), the uncertainties on the fit are estimate and considered in the following analyses. The low uncertainties expected demonstrates the exceptional quality of the ALMA data. However, the flux calibration introduces an intrinsic 7% uncertainty on the peak values of the spectra, thus the T_{ex} values derived for CO and CN have uncertainties of at least 7%. The effect of this is discussed in Sect. 5.4.

As CO is highly optically thick, the line profile displays a saturated core meaning the profile deviates strongly from an optically thin Gaussian (compare the CO spectra in Fig. 5.2 to those for CN). The line profile is therefore assumed to contain additional opacity broadening and therefore follows the form,

$$I_v = \left(J_v(T_{\text{ex}}) - J_v(T_{\text{bg}}) \right) \cdot \left(1 - \exp \left[-\tau \exp \left\{ -\frac{(v - v_0)^2}{\Delta V^2} \right\} \right] \right), \quad (5.1)$$

where $T_{\text{bg}} = 2.75 \text{ K}$, v_0 is the line centre and ΔV is the linewidth. If the line is sufficiently optically thick, T_{ex} and τ can both be constrained, otherwise it is only possible to constrain the product of the two. With this method, both T_{ex} and ΔV were found for all positions in TW Hya.

Under the assumption that all hyperfine components arise from the same region in the disk and that the main component is optically thick, the relative intensities of the CN hyperfine components yield an optical depth and T_{ex} . Using the hyperfine mode in CLASS, the hyperfine components were simultaneously fit with Gaussian profiles, yielding T_{ex} and ΔV for all locations in the disk. It was found that the recommended spacing of hyperfine components was systematically biased across the disk, suggesting that the recommended offset values were incorrect. Fitting for the relative positions of each component allowed for a better determination of their spacing to $\approx 1 \text{ m s}^{-1}$. The adopted frequencies and examples of the whole hyperfine ensemble can be found in Appendix A.

Finally, the CS emission was well fit by an optically thin Gaussian, from which we were able to accurately extract the line width and line centre. However, with only a

single transition observed, the degeneracy between T_{ex} and τ could not be broken so that we remain ignorant of the local temperature and can only measure ΔV .

Keplerian Shear Correction

In the following direct methods only the disk outside 40 au was considered. Within this radius the spectra start to strongly deviate from the assumed Gaussian line profiles because parts of the disk rotating in opposite directions are smeared in the beam. In this section, the contribution to the linewidth from beam smear is modelled.

To estimate the effect of the artificial broadening that is due to the beam smear, the physical model of TW Hya from Gorti et al. (2011) was used. The model was run through the LIME radiative transfer code (Brinch & Hogerheijde, 2010) for a range of inclinations, $i = \{0^\circ, 5^\circ, 6^\circ, 7^\circ, 8^\circ, 9^\circ\}$, assuming no turbulent broadening. As the projected velocity is a product of both stellar mass and inclination, by varying only the inclination, one can therefore consider uncertainties in both quantities³.

Following Rosenfeld et al. (2013), the height above the midplane was accounted for in the calculation of the velocity field as discussed in Section 2.3. Both CO J=(2-1) and C¹⁸O (2-1) lines were modelled, allowing us to sample an optically thick and thin case. Using CASA, the model observations were converted into synthetic observations with the same array configuration as the true observations. Differences in the resulting line width at each pixel between an inclined disk and a face-on disk were attributed to Keplerian broadening.

At our linear resolution (~ 25 au), the radial distribution of differences in line widths was well fit by a power law outside of 40 au,

$$\Delta V_{\text{Kep}} = (2.6 \pm 0.5) \times \left(\frac{r}{100} \right)^{-3.2 \pm 0.1} \text{ ms}^{-1}, \quad (5.2)$$

with r the radial distance in au. Quoted uncertainties are 1σ and are dominated by an uncertainty in inclination of $\pm 2^\circ$. The differences between the ¹²CO and C¹⁸O cases were smaller than these quoted uncertainties.

This component was subtracted from all line widths prior to further analysis. Figure 5.3 shows the measured line widths (black lines) and the line widths after the correction for Keplerian shear (blue lines).

Single Molecule Approach

After correcting for the Keplerian shear, it is assumed that the line width is only a combination of thermal and turbulent broadening. Hence the remaining line width can be described as

$$\Delta V = \sqrt{v_{\text{turb}}^2 + \frac{2kT_{\text{kin}}}{\mu m_{\text{H}}}}, \quad (5.3)$$

³The relative error $\delta i/i \approx 0.29$ assumed is equivalent to assuming $\delta M_{\star}/M_{\star} = 0.58$. Alternatively, this could be considered as $M_{\star} = 0.6 \pm 0.15 M_{\odot}$ and $i = 7 \pm 1.9^\circ$, values well representative of TW Hya.

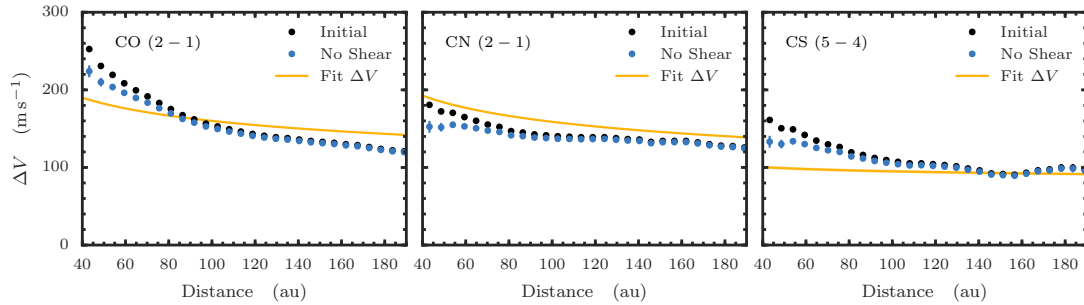


Figure 5.3 Measured line widths (black) and those corrected for the Keplerian shear component (blue) for CO, *left*, CN, *centre* and CS, *right*. All three lines are subject to the same Keplerian shear component. The yellow lines show the best-fit parametric model.

where μ is the molecular mass of the tracer molecule, m_{H} the mass of a hydrogen atom, the kinetic temperature of the molecule T_{kin} , and the line width $\Delta V = \text{FWHM}/\sqrt{4\ln 2}$.

For both CO and CN, the line profiles provided T_{ex} , therefore a conversion to T_{kin} must be made. Guided by the particle densities in the model of Gorti et al. (2011), the region of expected emission for CO and CN had densities of $\gtrsim 10^6 - 10^7 \text{ cm}^{-3}$, sufficiently high enough to assume that CO and CN lines are both thermalised and that $T_{\text{ex}} = T_{\text{kin}} = T$. The validity of this assumption is discussed in Sect. 5.4. The derived T_{kin} values for CO and CN are shown by the blue lines in the left two panels of Fig. 5.4. The black lines show $T_{\text{kin}}^{\text{max}}$, the highest kinetic temperature in the absence of any turbulence:

$$T_{\text{kin}}^{\text{max}} = \frac{\mu m_{\text{H}}}{2k} (\Delta V)^2. \quad (5.4)$$

In essence, the residual between these two lines must be accounted for either by turbulent broadening, or sub-thermal excitation, that is, $T_{\text{kin}} > T$. The (weak) effect of unresolved turbulence and or temperature gradients on the finite beam size is discussed in Sect. 5.4.

Outside of $r \sim 140 \text{ au}$, CN shows signs of non-LTE effects as the derived T_{ex} is considerably higher than $T_{\text{kin}}^{\text{max}}$, indicating weak pumping of the line (see Fig. 5.4). These ‘supra-thermal’ regions are neglected in the remainder of the analysis as an accurate T_{kin} is unable to be calculated.

With a known T_{kin} a simple subtraction of the thermal broadening component leaves v_{turb} . The left two columns of Fig. 5.5 show the derived v_{turb} in units of m s^{-1} in the top panel and as a function of local soundspeed c_s in the bottom panel for CO and CN, respectively. Fig. 5.6 shows the spatial distribution of v_{turb} (we here neglected the primary beam correction, which only reaches 7% at the map edge). For CS the line is essentially optically thin, and we cannot derive an excitation temperature.

Co-spatial Approach

Instead of relying on the temperature derived from a single molecule, one can take advantage of molecules with different molecular weights to separate the thermal and turbulent broadening, assuming the lines from these molecules emit from the same location in the disk. Under this assumption the total line widths would be tracing the same v_{turb} and

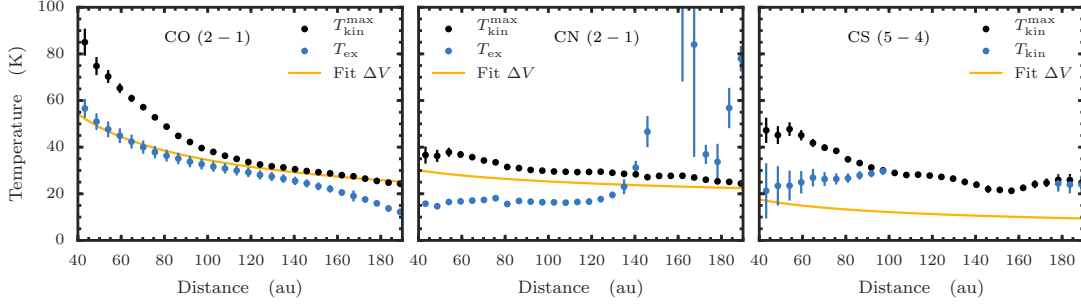


Figure 5.4 Radial profile of the derived T values (in blue) used for calculating the thermal broadening component of the line width for CO (left), CN (centre) and CS and CN assuming co-spatiality (right). For CO and CN this is T_{ex} while for CS this is T_{kin} . The black line shows the upper limit $T_{\text{kin}}^{\text{max}}$ that would fully account for the total line width in the absence of turbulent broadening. Outside 140 au, the derived T_{kin} exceeds $T_{\text{kin}}^{\text{max}}$ for CN and is thus not considered in further analysis. The black dots in the rightmost panel come from the CS line widths. Error bars show 1σ uncertainties on the mean.

T_{kin} . Solving Eq. 5.3 simultaneously for two molecules, A and B with respective molecular masses, μ_A and μ_B where $\mu_A < \mu_B$, and total line widths, ΔV_A and ΔV_B , we find

$$T_{\text{kin}} = \frac{m_{\text{H}}}{2k} \frac{\mu_A \mu_B}{\mu_B - \mu_A} \left(\Delta V_A^2 - \Delta V_B^2 \right), \quad (5.5)$$

$$v_{\text{turb}} = \sqrt{\frac{\mu_B \Delta V_B^2 - \mu_A \Delta V_A^2}{\mu_B - \mu_A}}. \quad (5.6)$$

This method does not make any assumption about the excitation temperature of the observed transitions, but relies entirely on the measured line widths and the co-spatiality of the emitting regions.

Of the observed molecules, CO may only trace a narrow layer because of its high optical depth. However one would expect the optically thin CN and CS to trace a larger vertical region. Both CN and CS would freeze-out at a similar temperature so that the bottom of their respective molecular layers would be relatively coincident and thus might potentially trace the same region in the disk. Hence this method is applied to the two lines of CN and CS.

The rightmost panel of Fig. 5.4 shows the T_{kin} (blue line) derived from CN and CS, in comparison to $T_{\text{kin}}^{\text{max}}$, the maximum T_{kin} derived from the CS line width (black). Radial profiles of v_{turb} derived from CN and CS are shown in the right column of Fig. 5.5, in m s^{-1} (top) and as a function of c_s (bottom).

Gaps in T_{kin} and v_{turb} correspond to the location where the μ -scaled line width of CS is smaller than the μ -scaled line width of CN (see Fig. 5.8). In this situation there is no solution to Eqs. 5.5 and 5.6, thus the assumption of CN and CS being co-spatial fails.

Parametric Model Fitting

The above direct methods require a proper correction of the Keplerian shear, which scales as $\sqrt{M_{\star}} \sin(i)$. For edge-on disks, or when the angular resolution is insufficient to remove

Table 5.1 Diskfit results for the three transitions.

Line	$V_{100} \sin(i)$ (m s^{-1})	e_v (-)	ΔV (m s^{-1})	$e_{\Delta V}$ (-)	T_{100} (K)	e_T (-)	v_{turb} (m s^{-1})	$e_{v_{\text{turb}}}$ (-)
FITTING FOR A TURBULENT LINEWIDTH COMPONENT								
CO J=2-1	262.7 ± 0.2	0.530 ± 0.001	-	-	35.4 ± 0.2	0.464 ± 0.001	71 ± 2	-0.22 ± 0.01
CN N=2-1	258.9 ± 0.6	0.564 ± 0.002	-	-	33.0 ± 0.2	0.02 ± 0.04	56.5 ± 0.5	-0.08 ± 0.02
CS J=5-4	261.0 ± 0.8	0.53 ± 0.01	-	-	12.1 ± 0.2	0.38 ± 0.07	66 ± 6	-0.10 ± 0.03
FITTING FOR A TOTAL LINEWIDTH								
CO J=2-1	262.7 ± 0.2	0.535 ± 0.001	160.0 ± 0.5	0.187 ± 0.001	35.51 ± 0.09	0.492 ± 0.001	-	-
CN N=2-1	252.9 ± 0.4	0.532 ± 0.007	158.8 ± 0.8	0.210 ± 0.003	25.3 ± 0.2	0.19 ± 0.04	-	-
CS J=5-4	261.0 ± 0.8	0.53 ± 0.02	95 ± 2	0.06 ± 0.01	12.16 ± 0.08	0.40 ± 0.07	-	-

Note: Results of the parametric model fitting. $V_{100} \sin(i)$ is the projected rotation velocity, ΔV is the total line width, T_{100} is the excitation temperature, and v_{turb} the turbulent velocity dispersion, all at 100 au and each with their corresponding exponent. The parameters not fit for were calculated using Eq. 5.3. For $M_{\star} = 0.69 M_{\odot}$, the measured $V_{100} \sin(i)$ indicates $i = 5.96 \pm 0.03$.

the Keplerian shear, these direct techniques are not applicable, and the only available method is to use a parametric model assuming T_{kin} and the total local line width ΔV . A parametric model fit can recover ΔV with high accuracy independently of the absolute flux calibration error. However, the fraction of this width that is due to turbulence depends on the absolute calibration since the thermal line width scales as the square root of the kinetic temperature.

In the following section, the Diskfit parametric model is used to fit the observations, as described in Section 3.3. With this method two models were fit, firstly one used previously in the literature where v_{turb} is described as a radial power-law, and secondly a model where the total line width was fitted for, ΔV , and then calculated the value of v_{turb} from Eq. 5.3. This method means that fitting for ΔV results in a non-power-law description of v_{turb} .

An inclination, position angle and systemic velocity were found that were comparable to literature values: $i \approx 6^\circ$, $\text{PA} \approx 240^\circ$ and $V_{\text{LSR}} \approx 2.82 \text{ km s}^{-1}$. Physical parameters relevant to v_{turb} are listed in Table 5.1 along with their formal errors. All three molecules yielded a steeper dependence of e_v than a Keplerian profile with $e_v \approx 0.53$. This change in projected velocity might either be a projection effect, such as a warp in the disk (Roberge et al., 2005; Rosenfeld et al., 2012), or gas pressure resulting in non-Keplerian rotational velocities for the gas (Rosenfeld et al., 2013). To account for such an exponent with a warp, i needs only to change by $\approx 1^\circ$ between 40 and 180 au, consistent with the findings of (Rosenfeld et al., 2013). Thus, while this non-Keplerian bulk motion was not considered explicitly in the removal of the Keplerian shear, the range of inclinations considered, $7 \pm 2^\circ$, sufficiently account for such a deviation.

As with the two direct methods, it was assumed that all lines were fully thermalised so that the excitation temperature recovered the full thermal width of the line. A comparison of the total line widths, temperature profiles and turbulent components are shown as yellow solid lines in Figs. 5.3, 5.4, and 5.5, respectively.

5.4 Results and Discussion

In the following section, the methodologies are discussed with a view to their uncertainties and ways of improving these for future studies of turbulence.

Temperature Structure

Thermal and turbulent broadening are hugely degenerate, and therefore a precise determination of the temperature structure is pre-requisite to deriving the level of turbulent broadening. Direct and parametric methods both yield comparable temperatures for CO and CN, as shown in Fig. 5.4, however very different values for v_{turb} were found, demonstrating the sensitivity of v_{turb} to the assumed temperature structure.

Excitation temperatures derived from the parametric modelling approach yielded warmer temperatures for CO than for CN, and in turn warmer than CS with $T_{100} = 35.4 \pm 0.2 \text{ K}$, $25.3 \pm 0.2 \text{ K}$, and $12.2 \pm 0.1 \text{ K}$ respectively, when fitting for a total line width

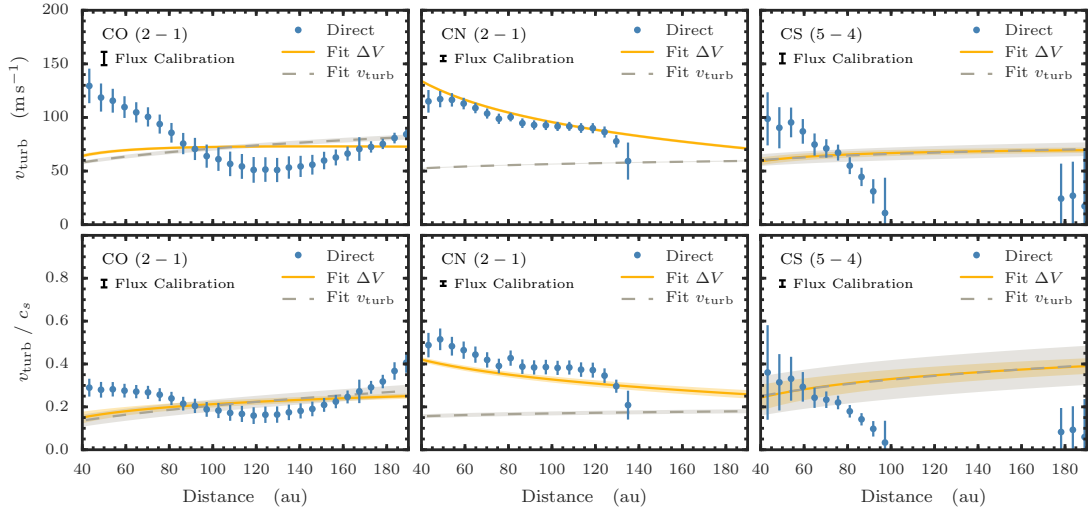


Figure 5.5 Radial profiles of the turbulent width in m s^{-1} , top row, and as a function of local sound speed, bottom row. The blue dots show the results of the direct method, where the CO and CN lines were assumed to be fully thermalised, and CS to be co-spatial with CN to derive a T_{kin} value. Yellow solid lines show the results from the global fit where the total line width was fit for, while dashed grey lines show the global fit where v_{turb} was fit for individually. The 1σ uncertainties are shown as bars for the direct method and as shaded regions for the lines. A representative error associated with the flux calibration of 7% at 80 au is shown in the top left corner of all panels.

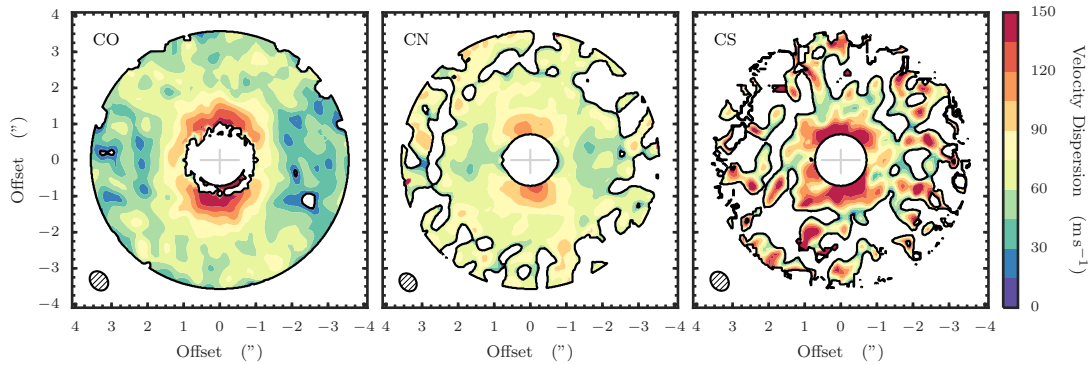


Figure 5.6 2D distribution of v_{turb} for all three lines: CO, *left*, CN, *centre*, and the combination of CN and CS assuming co-spatiality, therefore sharing the same T_{ex} and v_{turb} values, *right*. The values are masked outside 180 au and within 40 au. The beam size is shown in the bottom left corner for each line, and the major and minor axes are denoted by the central cross, aligned with the x- and y-axes, respectively. At the distance of TW Hya, $1'' \approx 54$ au. The azimuthal asymmetry seen in the inner disk is an artefact of a purely radial subtraction of the beam-smearing component discussed in Sect. 5.3.

(see Table 5.1). This trend was also seen in the direct methods. These values suggest that the emission from each molecule arises from a different height above the midplane in the disk and therefore could be used to trace the vertical structure of v_{turb} , as suggested with radiative transfer modelling.

In the single-molecule analysis, either direct or parametric, it was assumed that $T_{\text{ex}} = T_{\text{kin}}$ for both CO and CN, that is they are both in LTE. This assumption was guided by the model of [Gorti et al. \(2011\)](#), which has particle densities of $\gtrsim 10^6 - 10^7 \text{ cm}^{-3}$ from which molecular emission of CO and CN are believed to arise (see Fig. 2.8). This is sufficient to thermalise the CO line. Given that $T_{\text{kin}} \geq T_{\text{ex}}$, except from the extremely rare case of supra-thermal excitation, this analysis yielded a lower limit to T_{kin} , therefore an upper limit to v_{turb} . However, for CN, there is clear evidence for supra-thermal excitation beyond 130 au. A detailed discussion of this issue is beyond the scope of this project. In the future, it will be possible with multiple transitions to use the relative intensities of the transitions to guide modelling of the excitation conditions traced by the molecule, thereby yielding a more accurate scaling of T_{ex} to T_{kin} , as discussed in Chapter 7.

The co-spatial assumption for CN and CS clearly fails in certain regions of the disk where there is no simultaneous solution to Eqs. 5.5 and 5.6. The temperatures derived from the parametric modelling yield considerably different temperatures for CN and CS (see Table 5.1), suggesting that this co-spatial assumption fails across the entire disk. Chemical models suggest that CN is present mostly in the photon-dominated layer, higher above the disk plane than CS (although S-bearing molecules are poorly predicted by chemical models, see [Dutrey et al. \(2011\)](#)). The non-thermalisation of the CN $N = 2 - 1$ line that is observed beyond 130 au also supports the presence of CN relatively high above the disk plane. The accuracy of this assumption can be tested, as well as searching for other co-spatial molecular tracers, with the observation of edge-on disks where the molecular layers can be spatially resolved.

Measurements of temperature will be sensitive to temperature gradients along the line of sight due to both vertical and radial temperature gradients in the disk. Radial gradients will prove more of a problem than vertical gradients because molecular emission will arise predominantly from a relatively thin vertical region, therefore one would expect only a weak vertical dispersion in temperature. With the temperature profiles discussed in Sect. 5.3, one can estimate that the radial average dispersion across the beam is $\delta T_{\text{beam}} \lesssim 5 \%$ outside 40 au for all three lines with a maximum of $\sim 10 \%$ for the very inner regions.

To understand the effect of this on the subsequent derivation of v_{turb} , a two-zone model is considered. This consists of two regions with different temperatures, but the same turbulent velocity described by a Mach number, $\mathcal{M}_{\text{true}} = v_{\text{turb}}/\sqrt{2}c_s$ and the same optical depth. The temperature and line width were measured by fitting a Gaussian line profile of the resulting combined line profile and derived a Mach number, \mathcal{M}_{obs} . With this method one can explore how accurately \mathcal{M}_{obs} can recover $\mathcal{M}_{\text{true}}$ with a given temperature dispersion. Figure 5.7 shows the relative error on \mathcal{M} , $\delta\mathcal{M}$, as a function of $\mathcal{M}_{\text{true}}$ and temperature dispersion δT , assuming that the main temperature is 30 K. Taking the

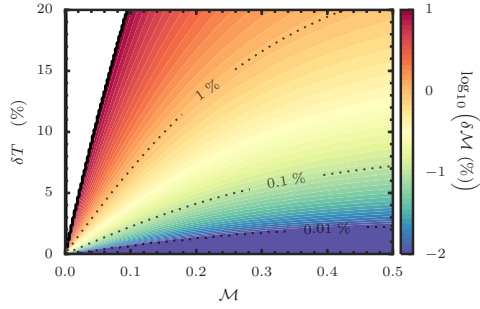


Figure 5.7 Effect of a temperature dispersion on the accuracy of the measurement of \mathcal{M} . The colouring shows how well an input \mathcal{M} value can be recovered from a line profile that is the summation of lines at differing temperatures described by δT .

temperature dispersions across the beam of 10 %, an uncertainty of $\lesssim 1\%$ for \mathcal{M} if found. This suggests that the determination of v_{turb} is not strongly biased by the expected line-of-sight gradients in temperature and turbulent width.

Turbulent Velocity Dispersions

With an assumed thermal structure, the turbulent broadening component was considered to be the residual linewidth which is not accounted for by thermal broadening nor beam smear. Resulting values of v_{turb} are compared in Figs. 5.5 and 5.6. All three methods yielded values of v_{turb} which ranged from $\sim 50 - 150 \text{ m s}^{-1}$ corresponding to the range $\sim 0.2 - 0.4 c_s$, but exhibited different radial profiles. The azimuthal structure seen near the centre of the disk in all panels of Fig. 5.6 is due to the azimuthal-independent subtraction of beam smearing used in Sect. 5.3.

Single Molecule Approach CO and CN emission allowed for a single-molecule approach as described in Sect. 5.3. CO yielded values of v_{turb} for $40 \lesssim r \lesssim 190$ au while CN was limited to $40 < r \lesssim 130$ au because of the potential non-LTE effects described in the previous section. Both molecules displayed a decreasing v_{turb} with radius, although CO has a slight increase in the other edges. As a fraction of c_s , both molecules ranged within $\sim 0.2 - 0.4 c_s$, but for CO this was found to increase with radius while CN decreased.

Co-spatial Approach Assuming CN and CS are co-spatial, v_{turb} values were calculated ranging from $v_{\text{turb}} \leq 100 \text{ m s}^{-1}$ or $v_{\text{turb}} \leq 0.4 c_s$, comparable to the range found for CO and CN individually. This method, however, is limited by the validity that CN and CS are co-spatial. The assumption drastically fails between $100 \lesssim r \lesssim 180$ au where the linewidth measurements do not allow for a solution of Eqs. 5.5 and 5.6 to be found. This is more clearly seen in Fig. 5.8 which shows the line widths of CN and CS scaled by $\sqrt{\mu}$ where $\mu = 26$ for CN and $\mu = 44$ for CS. In the region where no solution is found, the scaled line width for CS is smaller than that of CN. Despite failing for this molecular pair, this method provides an alternative method to derive T_{kin} and v_{turb} in another source with a different pair of molecules.

Parametric Model Fitting All previous measurements of v_{turb} have relied on fitting a power law model of a disk to the observations (Dartois et al., 2003; Piétu et al., 2007; Hughes et al., 2011; Guilloteau et al., 2012; Rosenfeld et al., 2012; Flaherty et al., 2015),

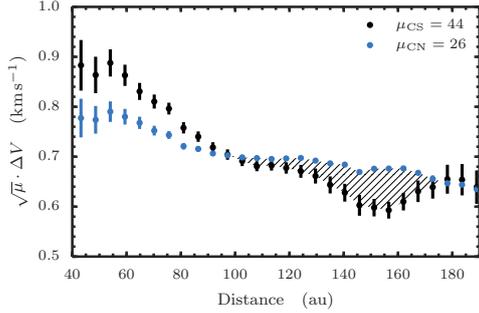


Figure 5.8 Comparing the $\sqrt{\mu}$ scaled line widths for CN (blue) and CS (black). The region where the scaled line width of CS drops below the values for CN, $100 \lesssim r \lesssim 170$ au, shown by the dashes, is where the co-spatial assumption can not be true. Error bars show 1σ uncertainties on the mean.

which allows for a direct comparison of the results in Section 5.3 to be compared with the literature. Furthermore, as data with reduced spatial and spectral resolution cannot be analysed by the direct methods, it is important to validate the parametric modelling approach by comparing those results with the direct methods.

The results of the Diskfit modelling process are shown in Table 5.1. Both models include the excitation temperature as a radial power law, but for one it was assumed that the total line width is a power law, while for the other we assumed that v_{turb} is a power law. A comparison between the parametric models and the direct methods is shown in Fig. 5.5, where the yellow solid line shows the case where ΔV , the total line width, was assumed to be a power law, and the dashed grey lines show where v_{turb} was assumed to be a power law. All three molecules display similar ranges of v_{turb} , $\sim 50 - 150 \text{ ms}^{-1}$ ($\sim 0.1 - 0.4 c_s$) to the direct methods.

For CO and CS the two parametric models yield similar results, but the second, where v_{turb} is fit for, has larger uncertainties. Both molecules have a slightly increasing v_{turb} with radius $e_{v_{\text{turb}}} \approx -0.22$ and -0.1 , respectively, around 60 m s^{-1} . CN, on the other hand, shows a distinct dichotomy between the two that is due to the different temperature profiles derived for the two methods (see Table 5.1). As mentioned in the previous section, CN displays non-LTE effects that the LTE parametric model may struggle to fit.

A limiting feature of this parametric model fitting is showcased by the results of CO (left column of Fig. 5.5). If the physical properties of the disk vary from a power-law description, the model will fail to fit this and may be driven to the best average description. For example, while the power-law method recovers v_{turb} for CO for $r \gtrsim 100$ au, inside of this radius the two derived v_{turb} values, one directly and one from model fitting, can deviate by up to a factor of 2.

Limits on the Detectability of v_{turb}

The single-molecule methods, either direct or parametric, are limited by the ability to recover the kinetic temperature with precision. Uncertainties on the kinetic temperature come from different origins: thermal noise, incomplete thermalisation of the observed spectral lines, absolute calibration accuracy, and in the parametric model, inadequacy of the model. Thermal noise can be overcome by increasing integration time. Incomplete thermalisation is a complex problem, and will in general require multi-line transition to be evaluated. However, in the case of CO, the critical densities are low, and we expect the

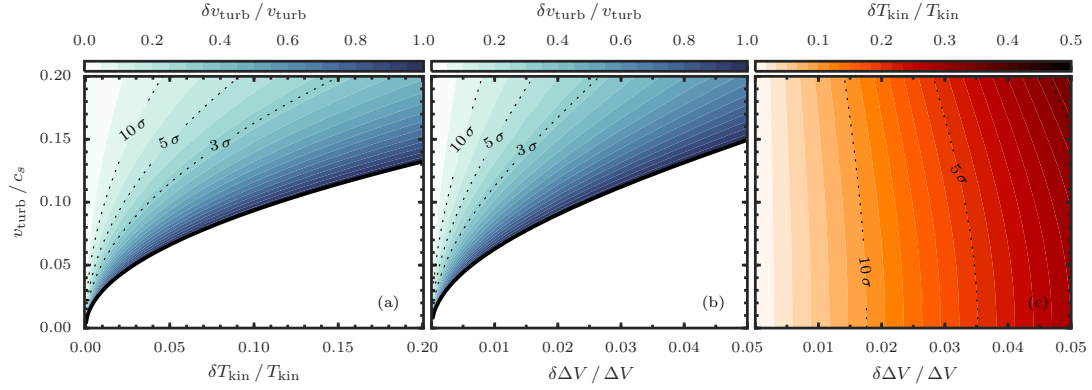


Figure 5.9 Limitations in determining v_{turb} and T_{kin} from the two direct methods. Panels (a) and (b) show the relative error in v_{turb} for a given (v_{turb}/c_s) as a function of the temperature (a) and line width (b) corresponding to the direct method with a known excitation temperature and the co-spatial method, respectively. Panel (c) shows the relative error in T_{kin} from the co-spatial method as a function of relative error in line width. The left panel does not take into account errors in the line width. The dashed contour lines show 10, 5, and 3 σ limits.

CO lines to be very close to thermalisation. Absolute calibration will place an ultimate limit on our capabilities of measuring the turbulence.

The sensitivity of the measure of v_{turb} as a function of the precision of the measurement of T is given by,

$$\frac{\delta v_{\text{turb}}}{v_{\text{turb}}} = \frac{\mu_{\text{H}}}{2\mu\mathcal{M}^2} \frac{\delta T}{T}, \quad (5.7)$$

where \mathcal{M} is the Mach number of the turbulent broadening and the derivation found in Appendix B. The left panel of Fig. 5.9 shows, in the absence of any error in the measurement of the line width, the relative error in v_{turb} as a function of relative error in T_{kin} for CO (assuming $\mu = 28$). It must be noted that as errors in ΔV have been neglected, Fig. 5.9a underestimates the precision in T_{kin} necessary to detect v_{turb} .

Previous measurements from the PdBI and the SMA have typical flux calibrations of $\sim 10\%$ and $\sim 20\%$ respectively (Hughes et al., 2011; Guilloteau et al., 2012). This suggests therefore that these can directly detect v_{turb} at 3σ only when $v_{\text{turb}} \gtrsim 0.16 c_s$ and $\gtrsim 0.26 c_s$, respectively. The ALMA data used for this project has a calibration accuracy of 7–10%, thus is sensitive to $v_{\text{turb}} \gtrsim 0.2 c_s$ for the turbulence not to be consistent with 0 m s^{-1} to 5 σ . Ultimately, ALMA is expected to reach a flux calibration of $\approx 3\%$, which will translate into a limit of $v_{\text{turb}} \gtrsim 0.07 c_s$ for a $\geq 3\sigma$ detection.

However, the flux calibration does not affect the precision to which widths can be measured. The resulting errors on turbulence and temperature derived in the co-spatial method are given by,

$$\frac{\delta v_{\text{turb}}}{v_{\text{turb}}} = \frac{1}{\mu_{\text{B}} - \mu_{\text{A}}} \frac{\delta \Delta V}{\Delta V} \sqrt{\left(\mu_{\text{A}} + \frac{\mu_{\text{H}}}{\mathcal{M}^2}\right)^2 + \frac{1}{x^2} \left(\mu_{\text{B}} + \frac{\mu_{\text{H}}}{\mathcal{M}^2}\right)^2}, \quad (5.8)$$

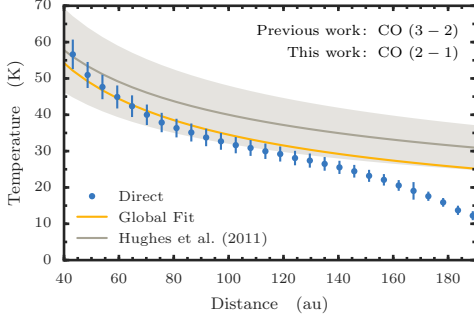


Figure 5.10 Comparing the temperature structure from this work and that of Hughes et al. (2011). The grey shading shows a flux calibration of $\sim 20\%$ typical of the SMA.

$$\frac{\delta T}{T} = \frac{2\mu_A\mu_B}{\mu_B - \mu_A} \frac{\delta\Delta V}{\Delta V} \sqrt{\left(\frac{\mathcal{M}^2}{\mu_H} + \frac{1}{\mu_A}\right)^2 + \frac{1}{x^2} \left(\frac{\mathcal{M}^2}{\mu_H} + \frac{1}{\mu_B}\right)^2}, \quad (5.9)$$

where x is a scaling factor between the relative errors on the two line widths,

$$\frac{\delta\Delta V_A}{\Delta V_A} = x \cdot \frac{\delta\Delta V_B}{\Delta V_B} = \frac{\delta\Delta V}{\Delta V}. \quad (5.10)$$

See Appendix B for the complete derivation.

Figure 5.9b shows the relative error on v_{turb} assuming the molecular masses of CN and CS (26 and 44 respectively) and that the relative errors on both lines are the same, $x = 1$. Figure 5.9c shows the limits of this method in determining T_{kin} . For the observations presented in this chapter, a precision in the measurement of the line width of $\approx 0.3\%$ was attained for both CO and CN, and $\approx 1\%$ for CS (therefore $x \approx 0.33$).

Parametric models typically return much lower formal errors on v_{turb} than direct methods (for example, the relative errors in Sect. 5.3 of about 5%). However, this is only a result of the imposed prior on the shape of the radial dependency of the temperature and turbulent width, which can lead to a significant bias which is not accounted for in the analysis. In any case, these parametric models suffer from the same fundamental limits due to thermalisation and absolute calibration as the single-molecule direct method.

Comparison with Other Measures

Turbulence in TW Hya was modelled previously by Hughes et al. (2011) using 40 m s^{-1} resolution SMA observations of CO (3-2). Using a model-fitting approach the authors found an upper limit of $v_{\text{turb}} \lesssim 40 \text{ m s}^{-1}$ corresponding to $\lesssim 0.1c_s$, considerably lower than the values plotted in Fig. 5.5. The temperature profile assumed for their parametric model was warmer than found in this work, with the authors quoting $T_{100} = 40 \text{ K}$ and $e_T = 0.4$, compared to the values used here of $T_{100} = 34.5 \pm 0.1 \text{ K}$ and $e_T = 0.492 \pm 0.002$ (see Fig. 5.10). This warmer profile is sufficient to account for any difference in the resulting v_{turb} . Nonetheless, both measurements are fundamentally limited by the absolute calibration uncertainty, and only imply $v_{\text{turb}} < 0.23c_s$ (SMA data) or $< 0.16c_s$ (ALMA data).

Other disks have also been the subject of investigations of v_{turb} . DM Tau, MWC 480 and LkCa 15 have yielded higher velocities of $\lesssim 100 - 200 \text{ m s}^{-1}$ ($\lesssim 0.3 - 0.5 c_s$) (Dartois et al., 2003; Piétu et al., 2007) which are sufficiently high to be detected by the PdBI.

However, the velocity resolution of the observations was about 200 m s^{-1} resulting in a poorly constrained total line width that may result in overestimating v_{turb} . The effect of the spectral resolution was accounted for in the more recent measurement of DM Tau by [Guilloteau et al. \(2012\)](#) using the heavier molecule CS, who found $v_{\text{turb}} \approx 0.3 - 0.4 c_s$. More recently [Flaherty et al. \(2015\)](#) used parametric modelling of multiple CO isotopologue transitions to infer $v_{\text{turb}} \lesssim 0.04 c_s$ in HD 163296.

One must also consider the effect of flux calibration on all methods involving a single line measurement, however. Every method will constrain the local line width using some combination of diagnostics, such as the broadening of channel images or the peak-to-trough ratio of the integrated spectra ([Simon et al., 2015](#)). Each method will recover this line width to its own precision, depending particularly on the functional form imposed on the spatial dependency of this line width. However, when the uncertainty on the local line width is known, Eq. 5.7 can be applied to propagate the error that is due to this uncertainty and to the absolute calibration precision to the turbulent component of the line width. Application to the results of [Hughes et al. \(2011\)](#) and [Flaherty et al. \(2015\)](#) yields upper limits of $v_{\text{turb}} < 0.23 c_s$ and $< 0.16 c_s$ respectively, more similar to what was measure in this work. The v_{turb} value found for DM Tau is considerably higher than limits imposed by the flux calibration ($\approx 10\%$), suggesting that the disk of DM Tau is more turbulent than those of TW Hya and HD 163296.

Comparisons with numerical simulations also provide a chance to distinguish between turbulent mechanisms. [Simon et al. \(2015\)](#) used an ensemble of shearing-box MHD simulations coupled with radiative transfer modelling to predict the velocity dispersion traced by CO emission in a proto-typical T-Tauri disk pervaded by MRI. The authors found that molecular emission would trace a transition region between the dead-zone and the turbulent atmosphere, showing velocity dispersions of between 0.1 and $0.3 c_s$, almost identical to the range found in TW Hya. [Flock et al. \(2015\)](#) ran similar, but global, models of a MRI active disk, finding velocity dispersions of $v_{\text{turb}} \approx 40 - 60 \text{ m s}^{-1}$ near the midplane, rising to $80 - 120 \text{ m s}^{-1}$ higher above the midplane, again consistent with the values found in TW Hya. A comparison with the α viscosity models is more complex because the relation between v_{turb} and α depends on the nature of the viscosity, with v_{turb} ranging between a few αc_s and $\sqrt{\alpha} c_s$ ([Cuzzi et al., 2001](#)).

A vertical dependence of v_{turb} , as found in [Flock et al. \(2015\)](#), is a typical feature of MRI-driven turbulence and may provide a discriminant between other models of turbulent mixing. In addition to the parametric model that found different temperatures for all three molecules, CO and CN yielded different T_{ex} values from the line profile fitting and the simultaneous method failed under the assumption that CN and CS are co-spatial. These pieces of evidence suggest that CO, CN, and CS each trace distinct vertical regions in the disk, potentially providing a possibility of tracing a vertical gradient in v_{turb} . With the current uncertainties on the temperatures for the three molecules we are unable to distinguish any difference in v_{turb} with height above the midplane.

[Cleeves et al. \(2015b\)](#) have modelled the ionisation structure of TW Hya using observations of key molecular ions HCO^+ and N_2H^+ , concluding that the disk may have a large

MRI-dead zone extending to $\sim 50\text{--}65$ au. An observable feature of such a dead zone would be a sharp decrease in the velocity dispersion at this radius. Our data lack the spatial resolution and sensitivity to reliably trace the gas turbulent motions in the inner ~ 40 au where this feature may be more prominent. However, the power-law analysis indicates that the v_{turb} values increase with radius (exponent $e_{\delta v} < 0$), in contrast with the direct measurements. This difference may be due to the effect of such a less turbulent inner region that is ignored in the direct method, but must be fitted in the power-law analysis.

Future observations will improve this analysis: to improve the accuracy of the v_{turb} determination with this direct method, a well-constrained thermal structure is crucial. This can be attained with observations of multiple transitions of the same molecule. Furthermore, for more highly inclined systems, a better understanding of the effect of beam smearing on the velocity dispersion is paramount. This can be achieved with smaller beamsizes that resolve a smaller shear component. Of the observed species, CS currently provides the best opportunity to probe velocity dispersions closer to the midplane, while we have demonstrated that the ensemble of CO, CN and CS can allow additionally for the determination of the vertical dependence of v_{turb} . Despite all these improvements, direct measures of turbulence will ultimately be limited by the flux calibration of the interferometers with a sensitivity of $\approx 0.1c_s$ for ALMA's quoted 3% accuracy.

5.5 Summary

In this chapter I have discussed two new methods of obtaining the turbulent velocity dispersion in the disk of TW Hya using CO, CN and CS rotational emission with a view to complementing the commonly used parametric modelling approach. Guided by previous models of TW Hya, the direct method yields v_{turb} values that strongly depend on the radius of the disk, reaching $\approx 150 \text{ m s}^{-1}$ at 40 au, dropping to a nearly constant $\approx 50 \text{ m s}^{-1}$ outside 100 au for all three tracers. As a function of local soundspeed, CO and CN displayed a near constant $v_{\text{turb}} \sim 0.2 c_s$. However, the analysis of the possible sources of errors shows that these numbers should most likely be interpreted as upper limits.

Direct or parametric methods using a single molecule are limited by a poor knowledge of the thermal structure of the disk. Additional transition lines will provide a more accurate determination of the temperature, but this is ultimately limited by the flux calibration of ALMA. With an expected error of at least 3% on the flux calibration, we estimate that a firm detection of turbulent broadening is only possible if $v_{\text{turb}}/c_s \gtrsim 0.1$ through this direct method. The co-spatial method can potentially overcome this absolute calibration problem, but it requires two co-spatial tracers of sufficient abundance to have strong emission. Tracing v_{turb} close to the midplane will be considerably more challenging because it requires a strong detection of o- H_2D^+ and another molecule residing in the midplane, such as N_2D^+ . Further outlook will be discussed in Chapter 7

A Surface Density Perturbation Traced by Molecular Emission

This chapter is based on work submitted to *The Astrophysical Journal*.

6.1 Motivation

Protoplanetary disks are sites of active planet formation and it is in the dense midplane of these disks where grain growth seeds planetesimal formation. Once a planet has grown to certain mass, it will begin interacting with the disk and sculpt the density structure (Kley & Nelson, 2012; Turner et al., 2014). The hall marks of ongoing planet formation and planet-disk interactions are frequently observed such as spirals and gaps in scattered light (Debes et al., 2013; Benisty et al., 2015; Wagner et al., 2015) or rings and dust traps seen in thermal mm-dust continuum (van der Marel et al., 2013; ALMA Partnership et al., 2015; Andrews et al., 2016).

While embedded planets are an attractive mechanism for producing these features, other physical mechanisms unrelated to planets have been shown to produce similar features, such as gravitational instabilities, dead zones of the magneto-rotational instability (MRI), snowlines of volatile species or dust evolution (Flock et al., 2015; Pohl et al., 2015; Zhang et al., 2015; Birnstiel et al., 2015). To connect these disparate regions requires studies of molecular line emission which traces the gas between the areas probed by thermal continuum or scattered light.

TW Hya, as the nearest protoplanetary disk to us at 59 ± 1 pc (Gaia Collaboration et al., 2016), is the most well studied disk across a huge wavelength range and is the ideal target for such a study. The disk displays a variety of substructures and radial morphologies in scattered light (Debes et al., 2013; Akiyama et al., 2015; Rapson et al., 2015; van Boekel et al., in press), mm-dust continuum (Andrews et al., 2012; Menu et al., 2014; Andrews et al., 2016; Tsukagoshi et al., 2016) and molecular line emission (Qi et al., 2013; Kastner et al., 2015; Nomura et al., 2016; Schwarz et al., 2016; Bergin et al., 2016), with many physical and chemical processes being invoked to explain these striking features.

Table 6.1 Summary of observations.

Transition	Rest Frequency GHz	Beam " × "	Beam PA °	Integrated Flux Jy km s ⁻¹	Channel RMS mJy beam ⁻¹
CO $J = (2 - 1)$	230.538	0.44 × 0.53	89.39	16.24	5.96
CN $N = (2 - 1)$	226.875	0.46 × 0.58	88.57	15.83	2.95
CS $J = (5 - 4)$	244.936	0.42 × 0.54	88.79	1.24	4.42

Note: The integrated fluxes were calculated using a $8'' \times 8''$ box centred on the source. For a full compliment of CN hyperfine transitions, see Table A.1 in Appendix A.

In this Chapter I present ALMA Cycle 2 observations of CS $J = (5 - 4)$ line emission whose radial profile shows a shallow dip coincident with the ~ 90 au dust gap seen in the scattered light (Debes et al., 2013; Rapson et al., 2015; van Boekel et al., in press). Section 6.2 describes the observations and the observed features while in Section 6.3 the modelling methodology carried out by van Boekel et al. (in press) is followed and I argue that these features are the result of a depression in the surface density of the gas rather than a chemical effect. The findings are discussed in more detail, including the potential power of molecular line emission as complimentary studies for disks studied at high resolution in scattered light and thermal continuum, in Section 6.5. A summary follows in Section 6.6.

6.2 Observations

The observations used in this Chapter are the same as used those in Chapter 5. For clarity, I briefly review the data analysis performed for these data.

Data Reduction

The observations of project 2013.1.00387.S (PI S. Guilloteau), were performed on May 13, 2015 under excellent weather conditions. Data were calibrated using the standard ALMA calibration script in the CASA software package¹. The absolute flux calibration was estimated using Ganymede. The derived flux for our amplitude and phase calibrator, J1037-2934, was 0.72 Jy at 228 GHz at the time of the observations, with a spectral index $\alpha = -0.54$, while the ALMA flux archive indicated a flux of 0.72 ± 0.05 Jy between April 14th and April 25th. We hence estimate that the calibration uncertainty is about 7%.

A summary of the observations can be found in Table 6.1. Figure 6.1 shows the continuum subtracted zeroth moment for all three lines. No molecular line shows azimuthal structure significant considering the noise. The integrated fluxes of the three lines are 16.24, 1.583 and 1.24 Jy beam⁻¹ km s⁻¹, calculated from an $8'' \times 8''$ box centred on the source, for CO $J = (2 - 1)$, CN $N = (2 - 1)$ and CS $J = (5 - 4)$ respectively.

As no azimuthal structure is seen in any of zeroth moment maps, nor suggested in previous observations, these data were azimuthally averaged assuming an inclination of

¹<http://casa.nrao.edu/>

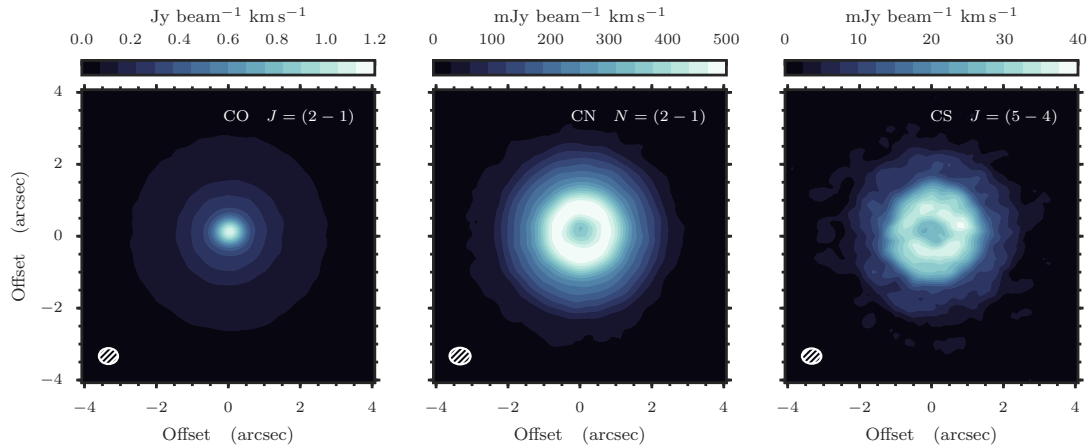


Figure 6.1 Zeroth moment maps of the CO, left, CN, centre, and CS, right, line emission used in Chapters 5 and 6. The CN moment contains emission from all 9 hyperfine components. The synthesised beam is shown in the bottom left hand corner of each panel.

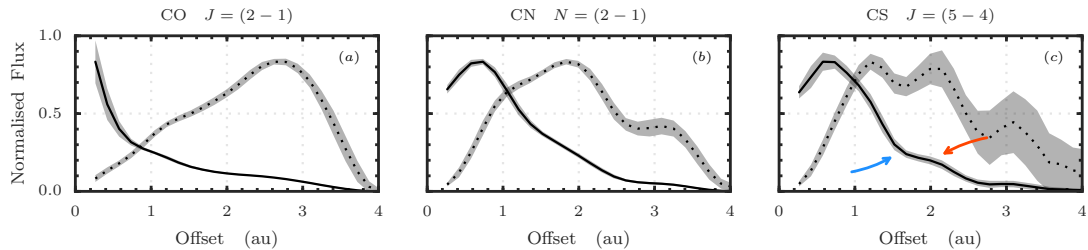


Figure 6.2 Normalised radial profiles of the line intensities. Solid lines show the direct values, while the dotted lines are with an r^2 scaling in order to bring out detail in the outer regions of the disk. The gray shading shows the azimuthal variation at each radial offset. The blue and red arrows in panel (c) highlight to the potential deficit and enhancement of CS emission respectively.

7° (Qi et al., 2004) to yield a radial intensity profiles, as shown in Fig. 6.2. The solid line shows the zeroth moment profiles, while the dotted line shows the r^2 scaling (panels (a) and (b) from Fig. 6.1 respectively). Gray shading around the lines demonstrate the 1σ variance of the radial bin. Note that r^2 scaling is commonly applied to scattered light observations to account for the drop in stellar flux at a given radial position, while for molecular line emission, such as here, this scaling is not physically motivated and applied purely to highlight the outer regions of the disk.

Radial Features

For both CN $N = (2-1)$ and CS $J = (5-4)$ radial profiles, the peak of emission is offset from the centre at $\approx 1.2''$. Distinguishing between a true inner depletion of the molecule and an artefact from continuum subtraction is impossible and so one can not make any comment on the presence of an inner hole. Outside of this, the emission falls off and is detected to $\sim 3.7''$ for all three molecules, comparable to that of the outer radius for

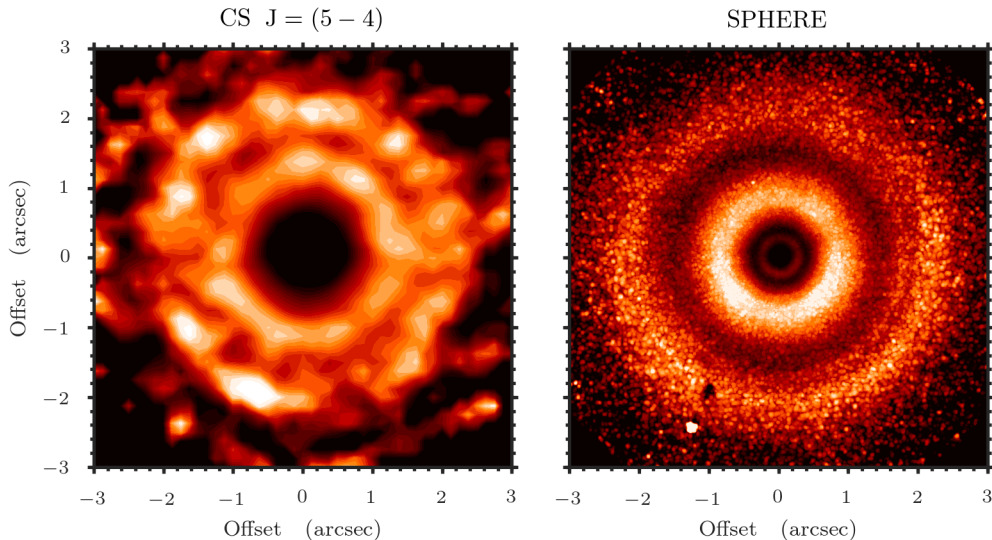


Figure 6.3 Comparing the r^2 scaled CS $J = 5 - 4$ emission, left, with the SPHERE scattered light observations from [van Boekel et al. \(in press\)](#), right. The concordance between profiles suggests a possible common origin.

scattered light ([Andrews et al., 2012](#)).

For CS $J = (5 - 4)$, the linear emission profile shows features between $1''$ and $2''$, as noted in panel (c) of Fig. 6.2, more clearly seen in the r^2 scaled profile shown by the dotted line. As there is no baseline to make a comparison with, the feature could be considered a dip in emission at $1.6''$, blue arrow, or an enhancement at $2.1''$, red arrow, corresponding projected distances of 95 au and 124 au respectively, assuming a distance of 59 pc ([Gaia Collaboration et al., 2016](#))². No similar feature is seen in CO $J = (2 - 1)$ profile, but may tentatively be detected in the CN $N = (2 - 1)$ emission. Given the extremely tentative nature of the detection in CN, focus is left on the CS emission.

Working on the assumption that the feature observed at $1.6''$ is a dip, the centre is coincident with that observed in scattered light intensity, initially observed with NICMOS on the Hubble Space Telescope ([Debes et al., 2013](#)) and later confirmed with ground-based observations ([Akiyama et al., 2015](#); [Rapson et al., 2015](#); [van Boekel et al., in press](#)). Figure 6.3 compares the r^2 zeroth moment in the left panel with the SPHERE scattered light observations from [van Boekel et al. \(in press\)](#) in the right panel which trace predominantly the gas surface density and small sub- μm sized grains in the atmosphere. Such a striking resemblance between the two radial emission profiles suggests a common physical origin. Unfortunately, the mm continuum has a sharp truncation at ~ 60 au ([Hogerheijde et al., 2016](#); [Andrews et al., 2016](#)), making a comparison with the large, mm-sized dust population impossible.

Conversely, an outer enhancement in molecular emission is also a possibility and a feature which has also been observed in several disks. The most striking example is the secondary ring of DCO⁺ in IM Lup ([Öberg et al., 2015](#)), while CO isotopologue emission in both AS 209 TW Hya have displayed similar radial emission profiles ([Huang et al., 2016](#);

²At the pre-Gaia distance of 54 pc ([van Leeuwen, 2007](#)), these would be 86 au and 113 au, respectively.

Schwarz et al., 2016). These three works have all invoked a secondary desorption front, either photo or thermal, which releases volatiles from the ices, resulting in enhanced emission locally. This scenario, however, requires a change in the local grain properties to incite a change in either the local UV rate or thermal structure of the disk (see, for example, Cleaves, 2016). This prerequisite is satisfied for all these three cases where the enhancement is observed near the edge of the mm-continuum, a proxy for the edge of the mm grains. However, for the case of the CS feature at $2.1''$, evidence of such a transition is lacking.

The absence of an obvious change in the grain properties at $2.1''$ and the concordance between the scattered light radial emission profile and that of the CS suggest a common, physical origin of the features observed in both the molecular emission and scattered light, rather than a chemical origin for the CS emission. This hypothesis will be explored in the following Section.

6.3 Modelling Surface Density Perturbations

A commonly invoked mechanism to account for dips in scattered light emission is a perturbation in the total surface density, a method used by both Debes et al. (2013) and van Boekel et al. (in press) to model the TW Hya scattered light emission. In this section, we explore the impact of such a surface density perturbation on the molecular emission of CS.

As molecular emission is a product of both excitation and abundance effects, it is important to perform self-consistent modelling taking into account the impact on the physical structure of the surface density perturbations and the resulting change in chemical abundances. To do this, we use an advanced thermochemical model in conjunction with chemical modelling and non-LTE radiative transfer to demonstrate the effect of a surface density perturbation on the radial profiles of the molecular emission and distinguish between scenarios.

For a baseline, we take the TW Hya model of Gorti et al. (2011) as the fiducial model. The unperturbed surface density is given by,

$$\Sigma_0 = 500 r^{-0.7} \exp\left(-\frac{r^{1.3}}{100}\right) \text{ g cm}^{-2}, \quad (6.1)$$

where r is the radial distance in au. The distribution was derived by fitting various gas spectra and dust continuum observed from the sub-millimetre to optical wavelengths. The model was made to reproduce integrated intensities rather than spatially resolved observations. Thus, while the model may not fully reproduce spatially resolved observations, it is a model with temperatures and densities expected in TW Hya. The model has a dust mass of $2.4 \times 10^{-4} M_\odot$ with an MRN-like grain size distribution, $n(a) \propto a^{-3.5}$, with maximum and minimum sizes of 1 mm and $0.09 \mu\text{m}$ respectively. The assumed relative abundance of polycyclic aromatic hydrocarbons (PAH) per hydrogen nuclei is 10^{-9} . The unperturbed model, Model A, is shown in Fig. 6.4 with the gas density, gas temperature and dust temperature in the panels, running left to right.

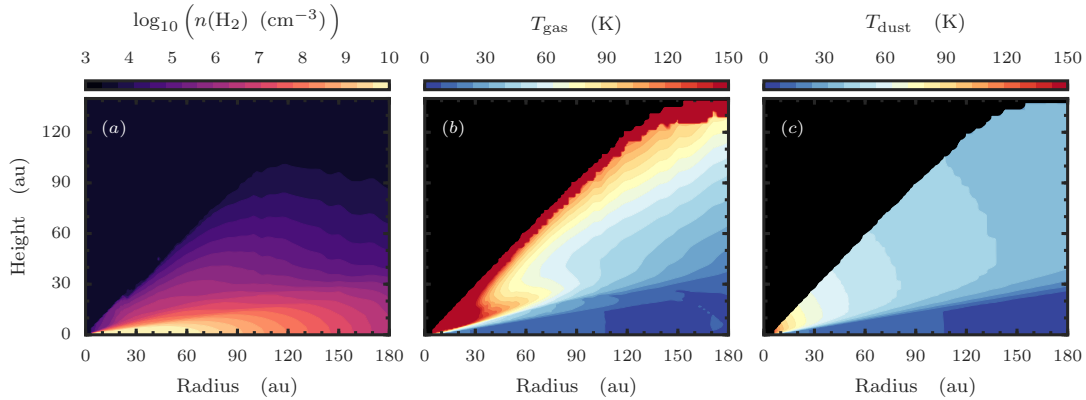


Figure 6.4 Physical structure of the fiducial model, Model A: $n(\text{H}_2)$, left; T_{gas} , center and T_{dust} , right.

The surface density is then perturbed with a Gaussian depression characterised by center d_0 , width Δd and depth d such that the resulting surface density is given by,

$$\Sigma(r) = \Sigma_0(r) \times \left(1 - d \cdot \exp \left[-\frac{1}{2} \frac{(r - d_0)^2}{\Delta d^2} \right] \right). \quad (6.2)$$

Three perturbations to the surface density are considered: Model B, a perturbation in the total surface density as in [Debes et al. \(2013\)](#), $d = 0.3$, $\Delta d = 20$ au and $d_0 = 80$ au; Model C, the outer perturbation from [van Boekel et al. \(in press\)](#), $d = 0.55$, $\Delta d = 15$ au and $d_0 = 80$ au; and Model D, a fully depleted gap, $d = 1$, $\Delta d = 9.45$ au and $d_0 = 80$ au³. The widths have been chosen such that each perturbed model has the same total mass. For each of the perturbed models, we also only apply the perturbation to the dust surface density, thereby creating a region with an enhanced gas-to-dust ratio, in order to test the hypothesis of a reduction in local heating by grains.

With the prescribed surface densities covering between 3.9 and 200 au (although TW Hya is observed to have material as close in as 1 au, this will not contribute to the low-energy molecular line emission concerned with here and is thus ignored in this modelling), the 1+1D disk physical structure was solved for self-consistently including heating and cooling processes following [Gorti et al. \(2011\)](#). Gas and dust temperatures are treated independently allowing the gas temperatures in the upper, more strongly irradiated regions of the disk to deviate strongly from those of the dust. The stellar radiation was set-up assuming a central star of mass $0.7 M_{\odot}$, radius $1.1 R_{\odot}$ and effective temperature of 4200 K. This comprises of a total far-UV luminosity of 3×10^{31} erg s⁻¹, an X-ray spectrum which covers 0.1–10 keV and a total X-ray luminosity of 1.6×10^{30} erg s⁻¹ and a cosmic ray ionization rate of 1.3×10^{-17} s⁻¹. The accretion rate is assumed to be $10^{-9} \dot{M}_{\odot} \text{ yr}^{-1}$, as constrained by the X-ray and UV observations (e.g., [Brickhouse et al., 2012](#)).

The resulting physical structures were used as the basis for the chemical modelling with the 1+1D code ALCHEMIC ([Semenov et al., 2010](#)), described in detail in Chapter 2,

³ A perturbation centre of 80 au was chosen guided by the observed location of the dip assuming the pre-Gaia distance of 54 pc. The location of the dip center should not alter the work's conclusions.

employing a full gas-grain network with deuterium fractionation, including up to triply-deuterated species (Albertsson et al., 2014), and assuming uniformly-sized amorphous olivine grains with the radius of $7 \mu\text{m}$. This grain size choice results in a grain surface per cell equivalent to that of the size ensemble used in the physical modelling. A ‘low metals’, mainly atomic set of initial abundances was used (Lee et al., 1998; Semenov et al., 2010). Chemistry was modelled over 1 Myr without taking dynamics and disk evolution into account, which is appropriate assumption for such chemically simple, fast-evolving species as CO, CN, and CS (Semenov & Wiebe, 2011).

These chemical abundances were then used for non-local thermal equilibrium (non-LTE) 3D radiative transfer modeling using LIME (Brinch & Hogerheijde, 2010). In the modelling a turbulent broadening component of $v_{\text{turb}} = 0.3c_s$, where c_s is the local sound-speed, was assumed (Teague et al., 2016). The collisional rates for CO and CS were taken from Yang et al. (2010) and Lique et al. (2010) respectively, stored in the LAMDA database⁴. CN emission was not considered as the LAMDA database does not contain up-to-date collisional rates for the hyperfine ensemble observed.

A final step was to make a comparison with the observation. The `simobserve` task in CASA was used to simulate observations using the same array configuration in order to account for the uv sampling and spatial resolution.

6.4 Results

As the observed molecular emission is affected by both excitation and abundance effects, the latter also depending on the physical structure of the disk, this Section will explore each stage of the modelling process in turn. Note that the aim of this modelling section is not to model TW Hya, rather explore the impact of different depth surface density perturbations on molecular emission.

Physical Structure

A depression in the surface density will create a change in the vertical structure of the disk, altering the amount of incident radiation and consequently the temperature and density of the region, impacting the chemical evolution. Figure 6.5 compares the different $n(\text{H}_2)$ and T_{gas} structures for the seven models around the perturbation centre. As T_{dust} remains largely unchanged, we do not plot those figures.

The shallow, $d = 0.3$, perturbation in Models B and Bd makes no significant changes to the physical structures compared to the physical structure of the standard disk, Model A. A slight reduction of the surface density over the dip does not affect the disk temperature structure, while gas density variations over the dip are too weak to be visible in the top row of Fig. 6.5.

With the slightly deeper perturbation in Model C, the scale height of the disk is reduced and results in a less vertically extended disk. With the depletion of smaller grains,

⁴ <http://home-strw.leidenuni.nl/~moldata/>

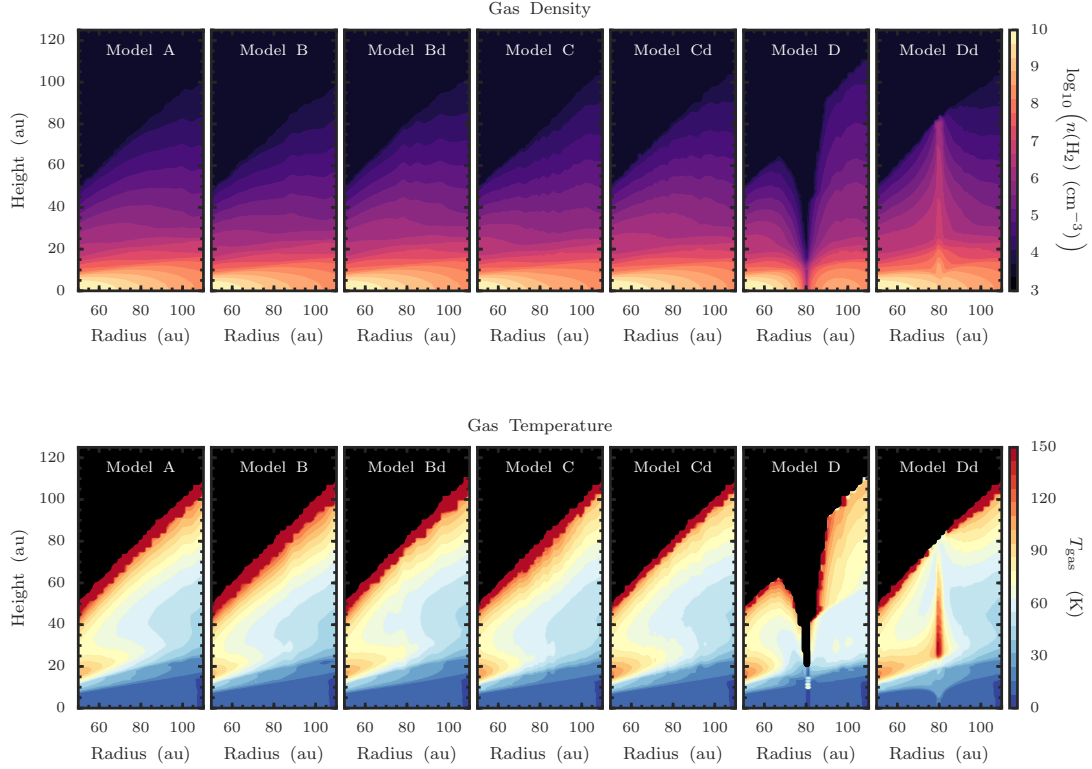


Figure 6.5 Comparison of the $n(\text{H}_2)$, top, and T_{gas} , bottom, structures for the seven models over the gap location, 80 ± 30 au. The physical structure outside this radial region is comparable for all seven molecules. As the dust temperature structure is indistinguishable between the models and so not shown. A compendium of all models can be found in Appendix C.

the gas is unable to cool as efficiently in Model Cd relative to Model C, resulting in a slightly warmer region with a temperature increase of ≈ 5 K.

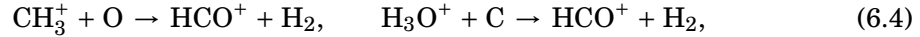
The effects of a fully depleted region in Models D and Dd are much more prominent, as shown in the final two columns of Fig. 6.5. For Model D, the reduction in surface density lowers the scale height of the disk, resulting in a highly irradiated outer surface. This enhances UV driven processes, such as H_2 pumping and photoelectric and PAH heating, resulting in a local temperature increase. In the dust depleted region in Model Dd, collisional cooling becomes less efficient, and gas gets locally hotter than in the unperturbed Model A. This results in a sharp spike in gas temperature, also increasing the gas scale height locally.

Chemical Structure

In the chemical network used CO is readily abundant, formed through a dissociative recombination,

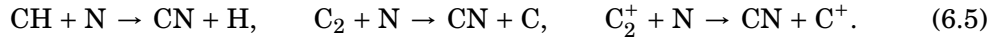


where the HCO^+ is formed mainly through reactions with the atomic C and O reservoir,



although other neutral-neutral pathways exist, but would be only a minor constituent. Removal from the gas phase is through either photodissociation by UV photons with $\lambda \lesssim 1150 \text{ \AA}$, or freeze-out onto grains, as discussed in Chapter 2.

CN requires an abundance of simple hydrocarbons, CH, C₂ or C₂⁺, formed quickly through ion-neutral reactions, which react with the atomic nitrogen reservoir,



Similarly to CO, CN is destroyed mainly through photodissociation from FUV photons with wavelengths again $\lambda \lesssim 1150 \text{ \AA}$, however does not benefit from the self-shielding CO does.

Finally, CS is efficiently formed through the recombination of HCS⁺, or HOCS⁺ at warmer temperatures, $T \gtrsim 50 \text{ K}$, with H₂ and in general formed earlier than CO. It is primarily depleted from the gas phase by freezing out onto grain surfaces with a freeze-out temperature ranging between 30 and 40 K depending on the local pressure.

The calculated column densities are shown in Fig. 6.6. For our unperturbed Model A at $r = 100 \text{ au}$, $N(\text{CO}) \sim 10^{18} \text{ cm}^{-2}$, $N(\text{CN}) \sim 5 \times 10^{13} \text{ cm}^{-2}$ and $N(\text{CS}) \sim 10^{13} \text{ cm}^{-2}$, values which are in good overall agreement with typically observed values in T Tauri disks (Guilloteau et al., 2012; Chapillon et al., 2012) and predicted for TW Hya (Kastner et al., 2014).

As with the physical structure of the shallow dip, Models B and Bd, the column densities for the three molecules deviate little from those of the unperturbed Model A. This demonstrates that changes in volume density on the order of 30%, such as those found in the perturbation for Debes et al. (2013), are insufficient to impact the CS chemistry and is unlikely to cause the observed feature in the emission profile. $N(\text{CO})$ rises slightly over the perturbation region due to the less efficient freeze-out of CO.

In contrast, Model C shows a clear depletion in $N(\text{CS})$ relative to Model A because the reduced density of the disk shifts the molecular layer deeper into the disk. For the dust depleted case, Model Cd, both $N(\text{CO})$ and $N(\text{CS})$ increase over the perturbation location as their freeze-out becomes less severe due to the much longer gas-grain collisional timescales. The enhancement of the disk UV irradiation in the gap cannot efficiently dissociate self-shielded CO molecules, and also does not affect drastically the CS molecular layer that sits deeper inside the disk.

In contrast, the molecular layer of the photo-stable radical CN is located above the CS and CO molecular layers. Hence, CN is less sensitive to the reduced freeze-out efficiency. This is clearly seen with the insensitivity of $N(\text{CN})$ to any of the perturbations in Models B, Bd, C or Cd.

Models D and Dd are extreme cases. The impact of reduced efficiency of depletion is most clearly seen in Model Dd which shows a spike of $N(\text{CS})$ where there are no grains available for the freeze-out, in stark contrast to what is observed in TW Hya. Furthermore, a fully depleted region of gas results in no molecular gas, as shown in Model D

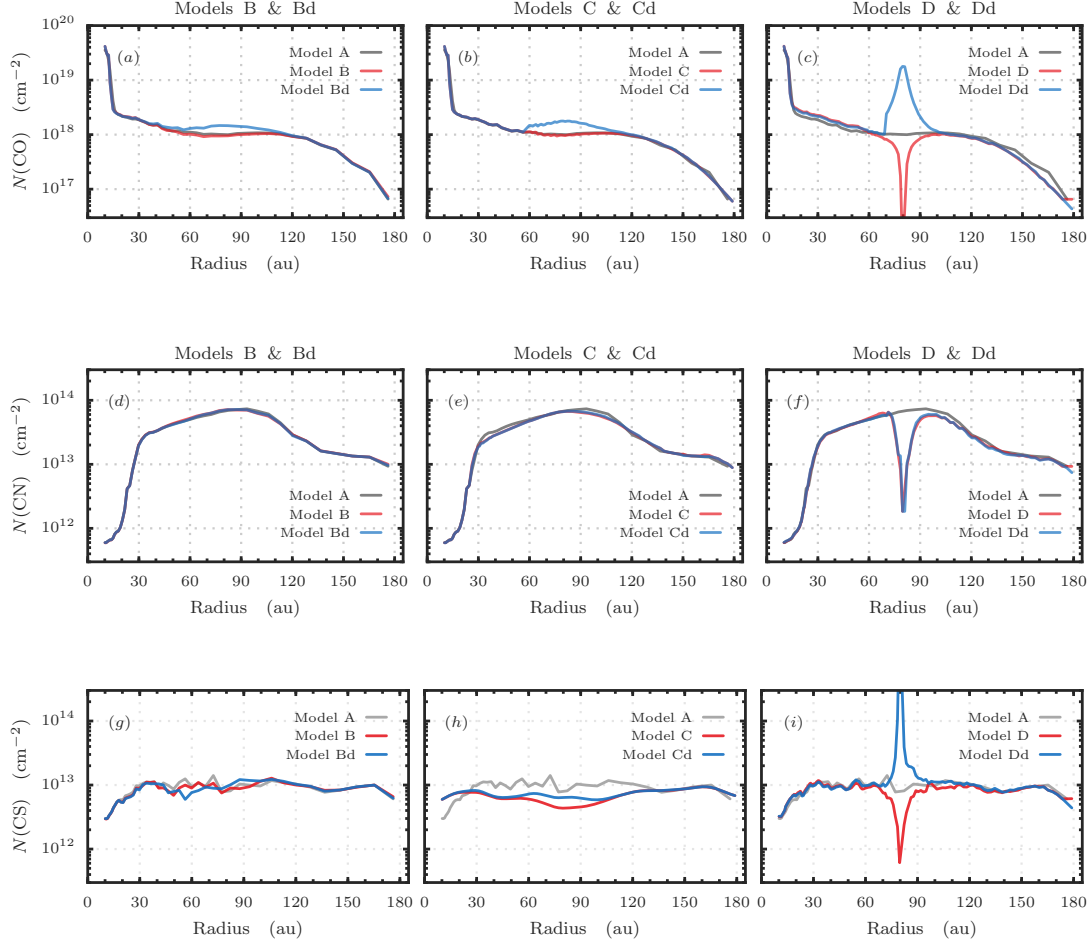


Figure 6.6 Column densities of CO, top, CN, center and CS, bottom, from Model A in gray, compared to those from the perturbed models. The red lines are for models with the perturbation applied to the total surface density, blue are where the perturbation is just in the dust surface density. Models B, C and D are in panels (a), (b) and (c) respectively.

with a large gap in $N(\text{CS})$. Such extreme changes in column density should be readily detectable in the emission profiles.

Interestingly, the vertically-averaged CO abundance relative to H_2 , $x(\text{CO})$, is lower than a standard value for solar the metallicity molecular gas, $\sim 2 \times 10^{-4}$. We find $x(\text{CO})$ increases from $\sim 10^{-7}$ at 15 au to a peak at 160 au of $\sim 10^{-4}$, consistent with the observationally inferred values & reported in Favre et al. (2013), Schwarz et al. (2016) and Kama et al. (2016a).

Molecular Emission

Figures 6.7 and 6.8 show the CO $J = (2-1)$ and CS $J = (5-4)$ radial intensity profiles after continuum subtraction for all seven models. Note that CN emission is not discussed here due to the lack of accurate collisional rates available for the non-LTE radiative transfer required (see Chapter 5). The left column shows the radial profile directly from LIME and the right column shows the radial profile for the simulated observations. The solid lines represent models with constant gas-to-dust ratios while dotted lines are for models with

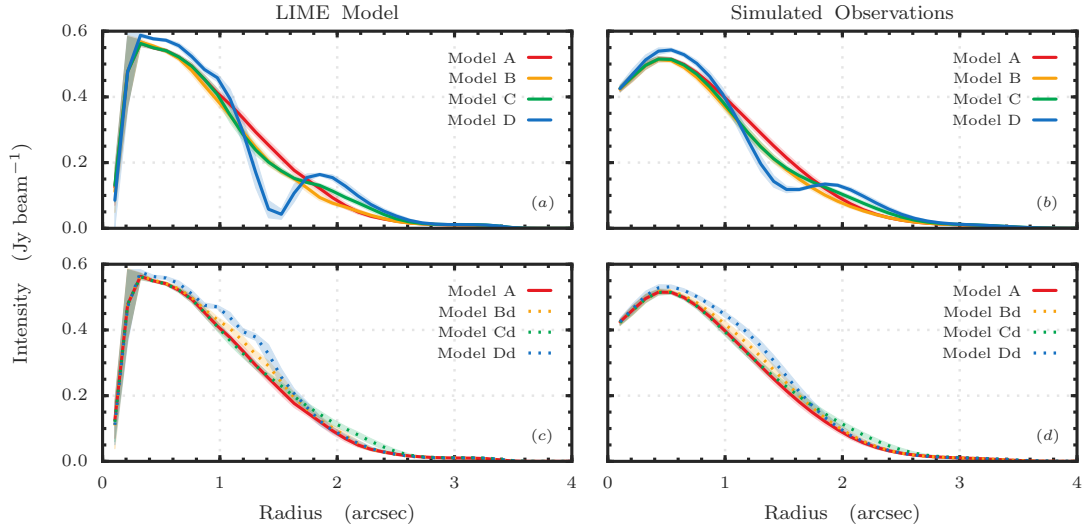


Figure 6.7 Continuum subtracted radial profiles of CO $J = (2 - 1)$ for the seven models considered. The top column is for models with constant gas-to-dust ratios, Models B, C and D, while the bottom row shows the models with a perturbed dust surface density profile, Models Bd, Cd and Dd. The left column shows radial profiles directly from the LIME while the right hand column shows the radial profiles after simulating the observations with the correct beam size and noise levels. The shaded regions around each line demonstrate the azimuthal deviation in each radial bin.

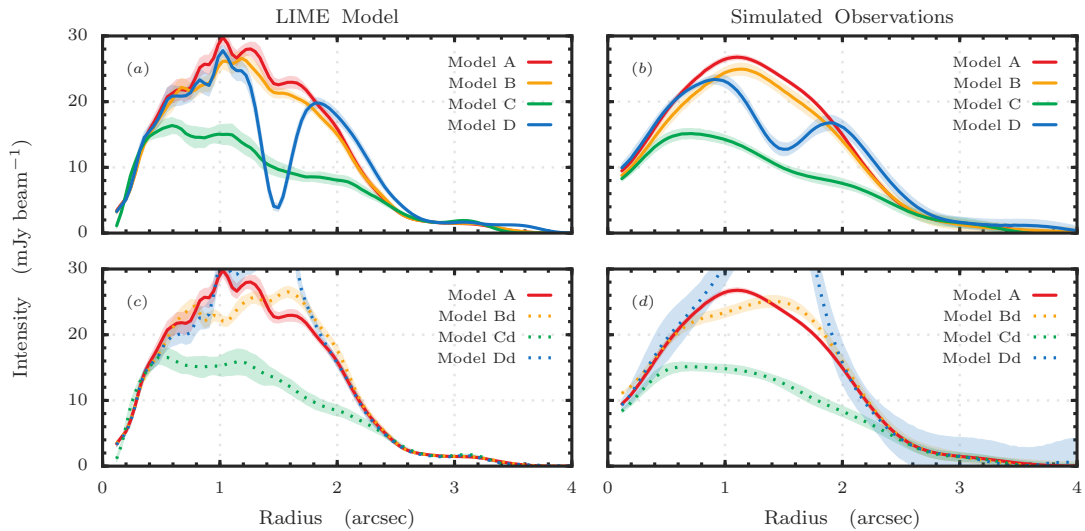


Figure 6.8 As Fig. 6.7, but for CS $J = (5 - 4)$. The peak of emission for Model Dd is $\sim 50 \text{ mJy beam}^{-1} \text{ km s}^{-1}$. Note that the bumps in the LIME models are due to the spikes seen $N(\text{CS})$, as shown in Fig. 6.6, a numerical effect which arises due to the sensitivity of the freeze-out of CS to the temperature structure.

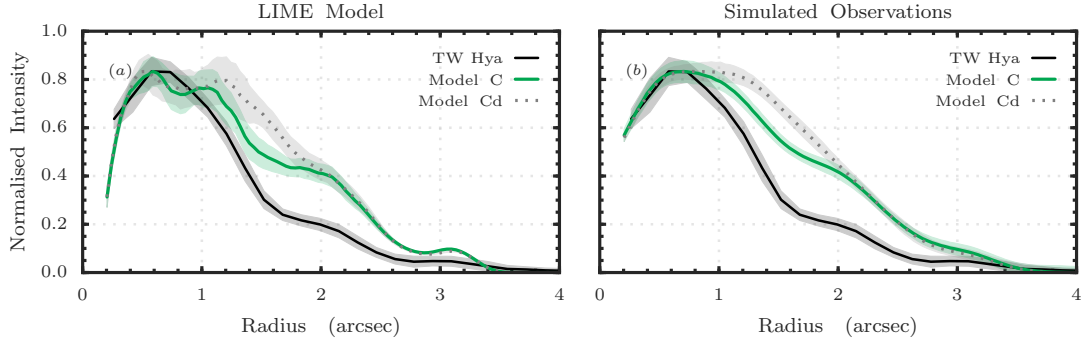


Figure 6.9 Comparing normalised radial profiles of TW Hya, black solid line, Model C, green solid line, and Model Cd, gray dotted line. Panel (a) shows the models from LIME, while panel (b) shows the models after simulating observations.

dust surface density perturbations and the shaded regions show the azimuthal variance of the radial bin. For the LIME model, the noise is intrinsic Monte-Carlo noise from the random grid in LIME.

CO emission, as it is highly optically thick, will be mostly sensitive to the temperature structure of the disk. This is seen in Fig. 6.7 as even a large change in $N(\text{CO})$ for Model Dd does not result in a large change in emission. Indeed for the two more realistic cases, Models B(d) and C(d), no clear feature is observed at the perturbation location of $r \sim 1.5''$. As expected for the extreme case of Model D a large feature is observed. Including the effects of beam smear show that the depth of the feature can be under-estimated. This is discussed further in Section 6.5. These emission profiles clearly rule out Model D as a possibly scenario for TW Hya, while CO alone does not allow one to distinguish between other scenarios.

For CS, as expected from the column densities, Models B and Bd exhibit no clear deviation from the unperturbed Model A, further demonstrating that a shallow dip cannot simultaneously explain the CS emission morphology and the NICMOS observations of [Debes et al. \(2013\)](#). Conversely, the extreme models of Model D and Dd produce clear features which would be easily recognisable in the observations had the surface density perturbation been so dramatic.

Models C and Cd show a clear deficit of emission relative to Model A due to the reduced column densities described in the previous section. Both emission profiles here show a more comparable morphology to the observations than other models. This is more clearly seen in Fig. 6.9 which compares the normalised radial profiles. Panel (a) shows the LIME models and panel (b) shows the simulated observations. Model C clearly has a radial morphology which is comparable to the observations while Model Cd lacks the depression at $1.6''$.

These simulated observations suggest that the surface density perturbation used in [van Boekel et al. \(in press\)](#) would be able to produce a similar radial morphology in CS $J = (5-4)$ emission as observed in TW Hya, while remaining undetected in CO $J = (2-1)$ emission. Furthermore, the more shallow perturbation used in [Debes et al. \(2013\)](#) was insufficient to make a noticeable change from the fiducial model and a fully depleted gap

Table 6.2 Comparison of published observations with model intensities.

Species	Transition	Rest Frequency (GHz)	I_{obs} (Jy km s ⁻¹)	I_{mod} (Jy km s ⁻¹)	$ \delta I $ (%)	Refs.
¹² CO	$J = (2 - 1)$	230.538	16.24	15.58	4.06	1
¹³ CO	$J = (3 - 2)$	330.588	4.71	5.83	23.78	2
	$J = (6 - 5)$	440.765	12.28	11.98	2.44	2
C ¹⁸ O	$J = (3 - 2)$	329.331	1.21	1.36	12.40	2
	$J = (6 - 5)$	439.089	1.60	1.61	0.63	2
CS	$J = (5 - 4)$	244.936	1.24	1.44	16.13	1
	$J = (6 - 5)$	293.912	2.3	1.72	25.22	3
	$J = (7 - 6)$	342.883	2.4	1.73	27.92	3

References: (1) [Teague et al. \(2016\)](#); (2) [Schwarz et al. \(2016\)](#); (3) [Kastner et al. \(2014\)](#).

would result in features which are far more prominent in the observations.

6.5 Discussion

The previous section has demonstrated that a surface density perturbation, which has been found to well model the scattered light profile of TW Hya, also produces a similar feature in the CS emission which has been observed in TW Hya. In the following section, we discuss the applicability of these models to TW Hya, explore potential physical mechanisms to produce such a perturbation, and consider the possibility of future work to better characterise such features.

Applicability to TW Hya

Foremost, it is important to understand the applicability of the modelling process to the specific case of TW Hya. Although the fiducial model was made to fit spatially integrated intensity of TW Hya and the modelled column densities for all three molecules are comparable to what is expected for such a T Tauri disk, there is a sufficiently large set of archival observations with which to make a comparison.

In addition to the two lines modelled for this work CO $J = (2 - 1)$ and CS $J = (5 - 4)$, previously published observations allow for a thorough comparison. [Schwarz et al. \(2016\)](#) have observed the $J = (6 - 5)$ and $J = (3 - 2)$ transitions for both ¹³CO and C¹⁸O isotopologues. In addition, [Kastner et al. \(2014\)](#) measured an integrated flux for the CS $J = (7 - 6)$ and $J = (6 - 5)$ transitions, as described in Table 6.2. As the chemical network does not include CO isotopologues, isotopologue abundances were scaled from ¹²CO assuming abundance ratios of $n(^{12}\text{CO}) / n(^{13}\text{CO}) = 84$, consistent with the ISM ([Wilson & Rood, 1994](#)), and $n(^{13}\text{CO}) / n(\text{C}^{18}\text{O}) = 10$, which was found for TW Hya ([Schwarz et al., 2016](#)).

The modelled integrated fluxes are listed in Table 6.2 along with their associated relative deviation in percent. Model A reproduces 8 emission lines to an average accuracy of

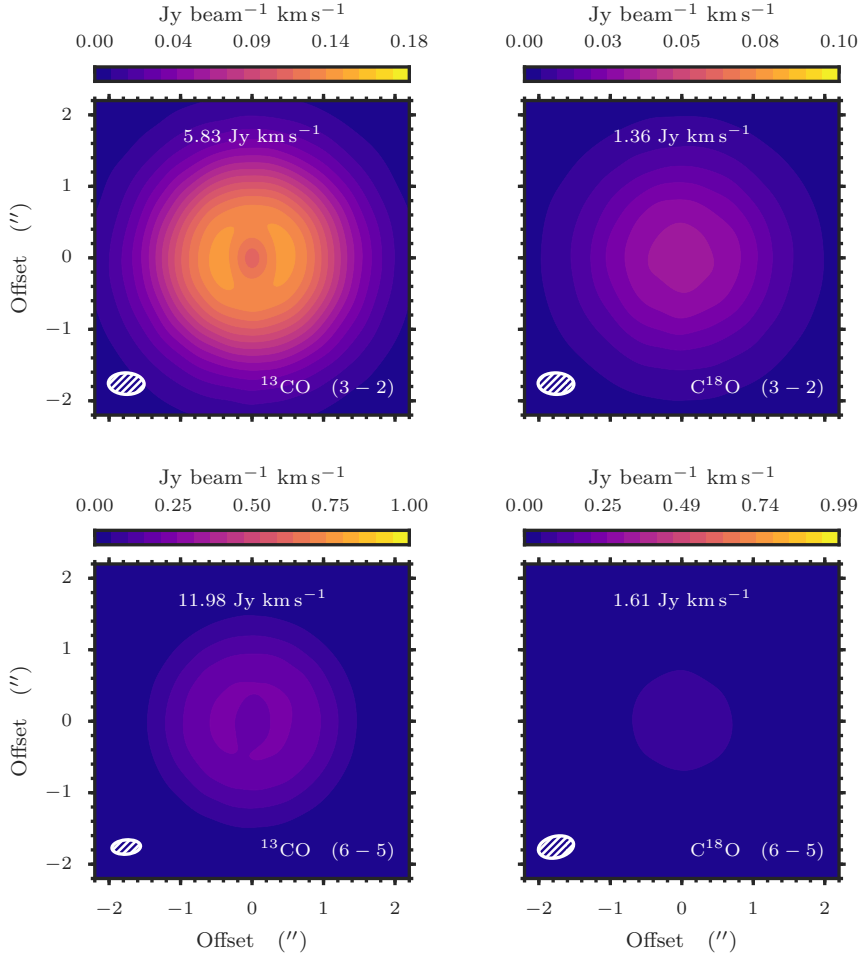


Figure 6.10 Modelled line intensity for ^{13}CO , left column, and C^{18}O , right column for $J = (3-2)$, top row, and $J = (6-5)$, bottom row. The colour scaling has been chosen to make a direct comparison with Fig. 1 from Schwarz et al. (2016). The integrated fluxes are at the top of each panel and a representative beam in the bottom left corner.

$\sim 15\%$ with the CS lines dominating the discrepancy. Reproducing a range of integrated fluxes gives confidence that the fiducial model is indeed representative of TW Hya.

A closer inspection of the radial profiles shows that all lines fail to match the observed radial profile in the same manner: emission in the outer disk ($r \gtrsim 90$ au) is over produced while in the inner disk it is under produced. Figure 6.10 shows the CO isotopologue emission to be compared with Fig. 1 from Schwarz et al. (2016). The observations of TW Hya display much stronger, centrally peaked emission and considerably less extended emission. This is likely because the fiducial model was made to fit integrated intensities, rather than spatially resolved observations, allowing some leeway in the radial gradients of the temperature and density profiles.

Such leeway in the radial profiles is not likely to be significant enough impact the findings here and thus give further confidence that the radial feature observed is indeed due to a surface density depression.

Carving a Gap

Although the modelling has suggested that a surface density perturbation could be the cause of the observed feature, it does not constrain the mechanism for producing such a perturbation. In the following I discuss some possible causes.

Embedded Planets

An attractive and commonly invoked mechanisms for explaining surface density perturbations is a planet carved gap (Lin & Papaloizou, 1986). Crida et al. (2006) show that the depth and width of a depression in the surface density can be used to constrain the mass of embedded planets. Debes et al. (2013) used this relationship with their perturbed surface density to estimate an embedded planetary mass of between 6 and 28 M_{\oplus} .

For the partially filled case, as suggested by the modelling, Duffell (2015) derives an analytic expression for the planet mass,

$$q^2 = \frac{3\pi\alpha d}{(1-d)f_0\mathcal{M}^5}, \quad (6.6)$$

where $q = m_{\text{planet}}/M_*$, α is the viscosity parameter (Shakura & Sunyaev, 1973), d is the depth as in Eqn. 6.2, $f_0 = 0.45$, a dimensionless parameter, and $\mathcal{M} = r/H_p$ is the Mach number. Taking the depth of the perturbation from Model C, $d = 0.45$, consistent with the depth found by van Boekel et al. (in press), $M_* = 0.7 M_{\odot}$ and $\alpha = 10^{-4} - 10^{-3}$, values appropriate for TW Hya (Teague et al., 2016), we find using Eqn. 6.6 a potential planet mass of 12 – 38 M_{\oplus} .

A better estimation could be made with a more precisely determined depth, d , requiring the dip feature to be observed in multiple molecular species equally sensitive to changes in local density and constrains on the local value of α . In addition, high-resolution observations of HCN and its isotopologues have been proposed as a chemical tracers of such an embedded planet (Cleeves et al., 2015a), allowing for a direct indication of a planet-opened gap.

Disk Instabilities

Pure hydrodynamical or magnetohydrodynamical instabilities can also create significant perturbations in the gas density structure (Turner et al., 2014). These instabilities can be broadly split into two types: ones producing azimuthally symmetric features, and those producing distinct azimuthal structures.

Molecular emission from TW Hya, in addition to the mm-continuum and scattered light observations, shows no strong azimuthal variance (Qi et al., 2013; Debes et al., 2013; Kastner et al., 2015; Akiyama et al., 2015; Rapson et al., 2015; Nomura et al., 2016; Andrews et al., 2016; Tsukagoshi et al., 2016; Schwarz et al., 2016; van Boekel et al., in press). Thus, instabilities which routinely produce vortices, spiral arms or azimuthally asymmetric gaps are likely not present at ~ 90 au in TW Hya. These include the baroclinic instability (Klahr & Bodenheimer, 2003; Cossins et al., 2010; Douglas et al., 2013; Takahashi et al., 2016), vertical shear instability (Nelson et al., 2013; Stoll & Kley, 2014;

Richard et al., 2016), zombie vortex instability (Marcus et al., 2015) and the Rossby wave instability (Lovelace et al., 1999; Varnière & Tagger, 2006; Lyra et al., 2015).

A more promising candidate is the magneto-rotational instability (MRI) (Balbus & Hawley, 1990). Flock et al. (2015) simulated a generic T Tauri disk assuming a gas-to-dust ratio of 100 which developed a surface density depression outside the dead-zone with a depth of $d \approx 0.5$. The change in density structure and Elsasser number over this boundary forms axis-symmetric zonal flows, carving the gap. A measurement of the radial extent of the dead-zone (or confirmation of its presence) would provide a great test for this instability, however previous analyses of the ionization and turbulent velocity structures have yet to detect the edge (Cleeves et al., 2015b; Teague et al., 2016). Furthermore, Flock et al. (2015) note that no structure is seen in simulated scattered light images, contrary to the case for TW Hya.

Grain Evolution

Motivated by the observed rings in scattered light, Birnstiel et al. (2015) demonstrated that grain evolution naturally leads to a region with a deficit of μm sized grains without the need to invoke perturbed surface densities. This arises due to the lack of replenishment of μm sized grains from the slow growth and drift time-scales at this region. Such a deficit of μm sized grains manifests as a dip in scattered light emission, but not thermal mm-continuum, because of the lack of grain surface to reflect the light.

Such a feature would have implications for molecular abundances, however detailed chemical modelling of such a mechanism, requiring the transport of frozen-out volatiles, is beyond the scope of this work. Modelling of recent observations of C_2H and C_3H_2 in TW Hya (Bergin et al., 2016) has shown that treating grain evolution can lead to significant changes in the local abundances of volatile species and is therefore an important avenue of exploration.

Molecular Tracers

In order to distinguish between scenarios, a better characterisation of the perturbation, such a depth and width, are required. By observing and modelling a range of molecular lines a tight constraint can be made on the local physical conditions. However, despite the large archive of molecular line observations in TW Hya, the radial feature has thus far only been observed in CS.

N_2H^+ observations do not betray structure in the outer disk Qi et al. (2013). However, the stark inner hole has been used as a proxy of the CO snowline at ≈ 30 au which was attributed as the cause of the inner depression of ^{13}CO and C^{18}O observed by Schwarz et al. (2016) and also seen by Nomura et al. (2016). The CO isotopologue emission also showed an enhancement at ≈ 60 au, consistent with a secondary thermal desorption front (Cleeves, 2016). This suggests an enhancement in CS at ≈ 120 au due to a secondary desorption front is an unlikely scenario due to the large distance from any clear transition in grain properties.

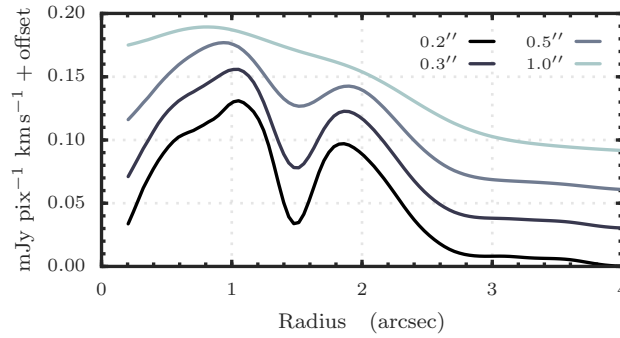


Figure 6.11 Radial intensity profiles for CS $J = (5-4)$ from Model D assuming different beam sizes. All models have the same integrated intensity. An arbitrary offset has been included to allow for easier comparison between profiles.

Kastner et al. (2015) observed C_2H emission in a ring between 45 and 120 au with the Sub-Millimeter Array (SMA), arguing the observed line intensities and radial location suggest a vertical segregation of grain sizes and considerable dust grain processing. Bergin et al. (2016) further argued with observations of C_2H and C_3H_2 that hydrocarbon rings require a local enhancement of the C/O ratio which could be achieved by the sedimentation and radial drift of grains rich in volatile ices. While these observations are not suggestive of a surface density perturbation, they do indicate that chemical abundances and the grain evolution are tightly coupled and must be considered together.

The modelling performed in Section 6.3 suggested that molecular lines such as N_2H^+ , H_2CO , HCN and HNC are all sensitive to small changes in the volume density, as invoked here. A full treatment of the radiative transfer for these molecules is left for future work, however it is clear that a larger repertoire of molecular tracers will provide unparalleled constraints on the physical structure of the outer disk.

Perturbation Depth

As discussed above, better discrimination between physical mechanisms can be made with through a more thorough characterisation of the physical conditions over the gap region which can be achieved through observations of molecular line emission. However, tracing features in molecular line emission rather than in continuum or scattered light will always be limited by the spatial resolution achievable. To understand how effective large beams are at masking such radial features, simulated observations of Model D were produced using range of beam sizes, $\theta_{\text{beam}} = 0.2, 0.3, 0.5$ and $1''$, as shown in Figure 6.11.

This demonstrates that a feature is only detectable by visual inspection for beam sizes of comparable size or smaller to the feature size. Thus, with a gap FWHM of $\approx 0.4''$ at 59 pc, only observations with spatial resolutions of $\theta_{\text{beam}} \lesssim 0.5''$ would potentially detect the feature. While a partially depleted gap, such as Model C, would need to be observed at an even higher resolution in order to detect the feature. Thus it is essential for not only a range of molecular species to be observed, but also high-resolution observations in resolve the features which may be hidden with large beam sizes. Achieving such a high

spatial resolution will be the ultimate limitation in future studies.

6.6 Conclusion

In this Chapter I have further analysed CS $J = (5 - 4)$ emission from the TW Hya disk which exhibits a dip-like feature at ≈ 90 au, comparable in morphology and position to the NICMOS total intensity scattered light observations [Debes et al. \(2013\)](#) and SPHERE polarized intensities ([van Boekel et al., in press](#)). Through self-consistent thermochemical modelling and extensive chemical and radiative transfer modelling, it has been demonstrated that a depression in surface density results in comparable morphology of the radial profile observed in CS.

Using a suite of models it was shown that a surface density perturbation with a depth of 55% relative to a fiducial model, as used by [van Boekel et al. \(in press\)](#) to model SPHERE observations of TW Hya, produces CS emission profiles comparable to those observed from the TW Hya disk. A less severe perturbation of 30%, as used by [Debes et al. \(2013\)](#) to model NICMOS observations, was insufficient to strongly alter the physical and chemical structure of the disk, while a fully depleted region produced features which were far too deep. Models with the perturbation applied only to the dust surface density, therefore enhancing the local gas-to-dust ratio, were shown to impede the freeze-out of CS, resulting in an enhancement of CS emission, in clear contrast to the observations.

These observations demonstrate the utility of molecular tracers in making a connection between features seen in scattered light and deeper within the disk. Higher angular resolution observations promise to better characterise the local physical conditions around such features, allowing for a more decisive exploration of the potential physical processes at play.

Summary and Outlook

7.1 Summary

This thesis used interferometric sub-mm observations of molecular line emission in two disks, DM Tau and TW Hya, in conjunction with extensive modelling, to unravel the physical condition pertinent to planet formation. Two chapters, 4 and 5, were based on work published in *Astronomy & Astrophysics*, [Teague et al. \(2015, 2016\)](#) while the work of the final chapter, Chapter 6, has been submitted to *The Astrophysical Journal*.

Chapters 2 and 3 reviewed the current state of modelling and observing protoplanetary disks. As observations continue to be taken, the equations which describe the physical structure will be refined and move towards a more accurate pictures of a protoplanetary disks. Furthermore, with ALMA allowing for more sensitive surveys than ever before, the molecular inventory of protoplanetary disks will be expanded, providing a test-bed for the refined models of disks.

In Chapter 4, HCO^+ and DCO^+ emission was used to constrain the deuterium and ionization structure of DM Tau. The deuterium fraction of HCO^+ , $R_{\text{D}}(\text{HCO}^+)$, is frequently used in star formation environments to infer a thermal history. A measured fraction of $R_{\text{D}}(\text{HCO}^+) = 0.1 - 0.2$, consistent with TW Hya and HD 163296 ([Qi et al., 2008](#); [Mathews et al., 2013](#)), suggests that deuterium fractionation continues through the disk lifetime and can potentially be used as a ‘chemical clock’. We have further demonstrated that in a protoplanetary disk this ratio is strongly affected by the OPR of H_2 whereby the larger energy of ortho- H_2 allows it to efficiently liberate deuterium from H_2D^+ and therefore larger surveys of the ortho-para chemistry must be made in order to full understand deuterium fractionation. However, this will remain a challenge as in disks and molecular clouds this ratio has to be indirectly constrained using ortho- H_2D^+ observations from ALMA and para- D_2H^+ observations with the Stratospheric Observatory for Infrared Astronomy (SOFIA).

Furthermore, as the most abundant molecular ion in a protoplanetary disk, HCO^+ and DCO^+ emission was used to constrain the ionization structure of the disk. Assuming a steady-state closed system, akin to that used in [Caselli et al. \(2008\)](#), an ionization

fraction of $x(e^-) \sim 10^{-7}$ was found in the HCO^+ molecular layer, comparable to those found by [Dutrey et al. \(2007\)](#) and [Öberg et al. \(2011b\)](#). Chemical modelling showed the sensitivity of HCO^+ and DCO^+ abundances to the incident radiation field, with a radial gradient in R_D being proposed as a diagnostic between the influences of X-ray and UV radiation.

ALMA observations allowed for the first mapping of turbulent broadening in a protoplanetary disk, as described in Chapter 5. Using three different approaches for each of the three lines of $\text{CO } J = (2-1)$, $\text{CN } N = (2-1)$ and $\text{CS } J = (5-4)$, kinetic temperatures were calculated in order to remove the thermal broadening component of the line. Beam smear was accounted for by modelling the disk at face on values and inclined values. The methods all found comparable values of $v_{\text{turb}} \sim 0.2c_s$ across the radius of the disk. Such a value is consistent with predictions from global MHD models of the MRI ([Simon et al., 2015](#); [Flock et al., 2015](#)), suggesting that such a dynamical process could be driving angular-momentum transport and planet formation within the disk.

The idea of active planet formation in the disk of TW Hya was further explored in Chapter 6. The $\text{CS } J = (5-4)$ emission displays a dip-like in emission, remarkably similar in morphology to those observed in scattered light images ([Debes et al., 2013](#); [Akiyama et al., 2015](#); [Rapson et al., 2015](#); [van Boekel et al., in press](#)). As much success has been found in modelling the scattered light observations with a perturbation in the surface density, usually with an embedded planet invoked as the perturber, thermo-chemical modelling was used to explore how molecular emission reacts to such a gap. With the inclusion of a surface density perturbation of similar properties to that used in [van Boekel et al. \(in press\)](#), the morphology of the radial profile of $\text{CS } J = (5-4)$ intensity was well reproduced. Both a less severe perturbation, as used by [Debes et al. \(2013\)](#) to model the scattered light, and a fully depleted case yield no discernible and a far too extreme feature in the radial profile respectively. This modelling suggests that this could be the first detection of a surface density perturbation with molecular line emission.

7.2 Outlook

The findings of this thesis provide the foundations upon which additional studies can be made. In this section I will briefly discuss possible avenues of investigation which stem from this thesis.

Already, ALMA programs have been carried out with the aim of further characterising deuterium fractionation in protoplanetary disks ([Öberg, 2016](#)). These have, for example, led to the first detection of N_2D^+ ([Huang & Öberg, 2015](#)) and better constraints on the DCN / HCN ratio, vital tools in measuring R_D in CO depleted regions of the disk as well as some surprises, such as double rings of DCO^+ emission in IM Lup ([Öberg et al., 2015](#)). Such observations are further cementing the finding raised in Chapter 4, that the molecular abundances are more tightly coupled to a range of physical parameters than simply one variable, in this case the thermal history, requiring a much more accurate global picture of the disk.

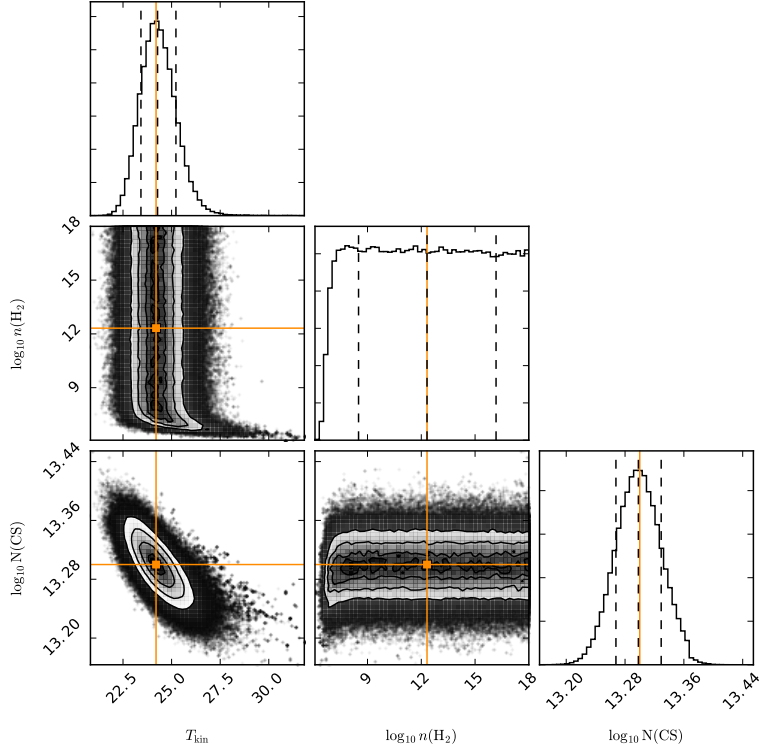


Figure 7.1 Example of the possibility of constraining T_{kin} , $n(\text{H}_2)$ and $N(\text{CS})$ through the relative intensities of three emission lines: $J = (7 - 6)$, $(5 - 4)$ and $(3 - 2)$. For this example a flux calibration uncertainty of 5% was assumed. The orange lines show the true values of $T_{\text{kin}} = 24.2$ K, $\log_{10} n(\text{H}_2) = 12.32$ and $\log_{10} N(\text{CS}) = 13.3$. The best fit values are: $T_{\text{kin}} = 24.27 \pm 0.90$ K, $\log_{10} n(\text{H}_2) = 12.32 \pm 3.84$ and $\log_{10} N(\text{CS}) = 13.30 \pm 0.03$.

When it comes to measuring turbulence, a key finding in this thesis was that the measure of v_{turb} will ultimately be limited to how well T_{kin} can be measured. By using multiple transitions of the same molecule, assuming that all transitions arise from the same region in the disk and therefore share the same excitation conditions, T_{kin} , $N(\text{mol})$ and $n(\text{H}_2)$ can be incredibly well constrained. Proposed for ALMA Cycle 4 observations (PI Teague), 5 hours were granted with an A grading to observe the CS lines of $J = (7 - 6)$ and $(3 - 2)$ to compliment the $(5 - 4)$ data presented in Chapters 5 and 6. Using an excitation analysis, Fig. 7.1 demonstrate how well we estimate these observations can constrain T_{kin} , even with an assumed flux calibration of $\approx 5\%$. Such a well constrained temperature promises an unparalleled measure of v_{turb} in protoplanetary disks.

Another conclusion from Chapter 5 which requires further exploration is to develop a method to distinguish between drivers of turbulent motions. The approach outlined in the previous paragraph only works for face-on disks due to the complication of beam smear on the line widths. The results in Chapter 5 already showed promise in that molecular emission can trace v_{turb} at varying heights in the disk, potentially distinguishing between gravo-turbulence and other hydrodynamical instabilities (Forgan et al., 2012). Although limited by the absolute accuracy one can extract v_{turb} through parametric model fitting, relative values between molecules with different temperature profile would be strong

evidence for a vertical gradient in v_{turb} . Furthermore, looking at the large disturbances caused by dynamical instabilities, such as vortices, would provide a distinction between instability scenarios. Exploring the azimuthal dependence of the bulk rotation of the gas in addition to the radial gradient (as done in, for example, [Rosenfeld et al., 2012](#)) could potentially provide clues to the global dynamics.

Finally, Chapter 6 demonstrated that molecular emission can trace surface density perturbations, a traditional signpost of on-going planet formation. While this avenue of investigation will undoubtedly be dominated by mm-continuum images which can achieve spatial resolutions far surpassing that of molecular emission, molecular emission will have a large part to play in terms of deriving the local physical conditions.

Molecular emission yields a wealth of information which cannot be attained from observations of dust alone. Excitation analyses, as described above, will allow for the gas temperatures to be directly measured without having to perform iterative fitting of a global model. These analyses will also provide constraints on the column densities of molecules to further benchmark chemical models. Combining these with the different heights of molecular layers would also potentially allow for a vertical profile of a gap to be constructed. Simulations have suggested that by constraining the gap profile through such observations would provide exceptionally tight constraints on the mass of the embedded planet (for instance [Fung et al., 2014](#); [Duffell, 2015](#)). These methods combined with indirect tracers, such as a local enhancement in thermal desorption due to the accreting protoplanet ([Cleeves et al., 2015b](#)), will allow for the detections of the embryos of planets.

CN in TW Hya

The quality of the CN $N = (2 - 1)$ data obtained used in Chapters 5 and 6 allowed for the fitting of the line centres of the hyperfine components to a better precision than measured in the laboratory. Figure A.1 displays the azimuthally averaged lines at different radial positions. Table A.1 shows the updated line centre values used in this thesis.

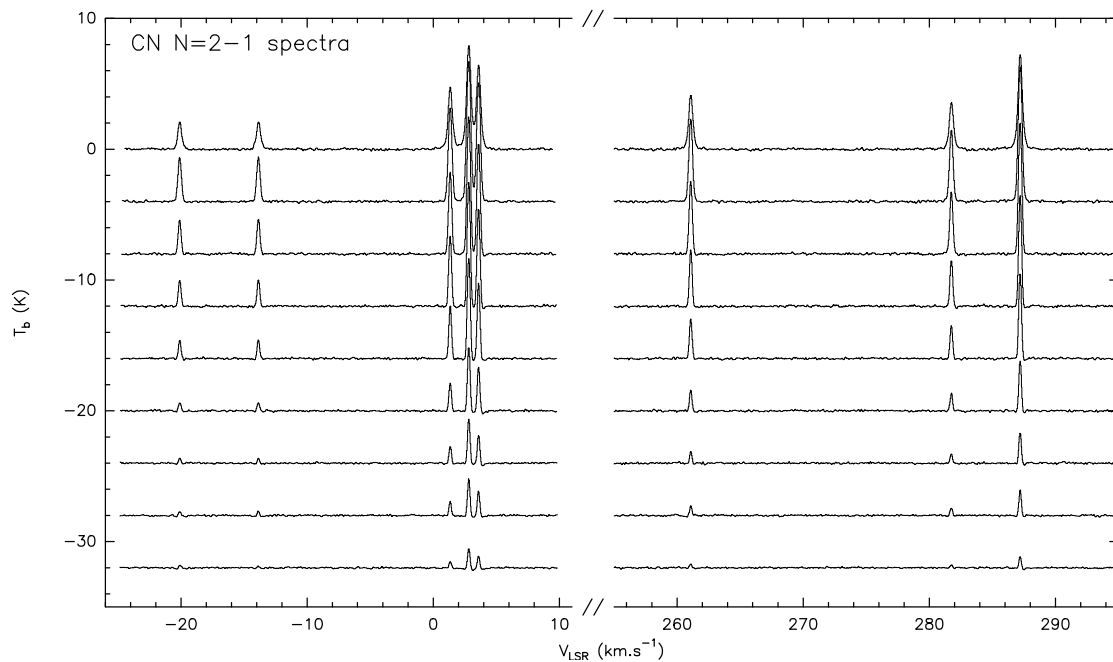


Figure A.1 Full compliment of the azimuthally averaged CN spectra including all hyperfine components. The radial offsets show different radial positions in the disk, separated by roughly a beam width.

Table A.1 New Frequencies for CN $N = (2 - 1)$ transitions.

Old Frequency (MHz)	New Frequency (MHz)	Offset (MHz)	Transition
226659.5584	226659.564	+0.008	CN N=2-1 J=3/2-1/2, F=5/2-3/2
226663.6928	226663.694	+0.001	CN N=2-1 J=3/2-1/2, F=1/2-1/2
226679.3114	226679.331	+0.020	CN N=2-1 J=3/2-1/2, F=3/2-1/2
226874.1908	226874.191	0.000	CN N=2-1 J=5/2-3/2, F=5/2-3/2
226874.7813	226874.781	[0]	CN N=2-1 J=5/2-3/2, F=7/2-5/2
226875.8960	226875.896	0.000	CN N=2-1 J=5/2-3/2, F=3/2-1/2
226887.4202	226887.403	-0.017	CN N=2-1 J=5/2-3/2, F=3/2-3/2
226892.1280	226892.128	0.000	CN N=2-1 J=5/2-3/2, F=5/2-5/2
226905.3574	226905.353	-0.004	CN N=2-1 J=5/2-3/2, F=3/2-5/2

Note: CN N=2-1 line frequencies were measured in laboratory by [Skatrud et al. \(1983\)](#); Values in Column 1 are the fitted values from the CDMS Database ([Müller et al., 2001](#)). Column 2 indicates the values derived from ALMA observations.

Error Derivations for Turbulence

In this Appendix I derive the uncertainty relations for v_{turb} used in Chapter 5. These uncertainties are assumed to be uncorrelated.

B.1 Direct Turbulent Velocity Dispersion

Assuming T_{kin} is known, the turbulent velocity component v_{turb} is given by

$$v_{\text{turb}} = \sqrt{\Delta V^2 - \frac{2kT}{\mu m_p}}. \quad (\text{B.1})$$

We assume $\delta T \gg \delta \Delta V$, therefore the uncertainty on v_{turb} is

$$\delta v_{\text{turb}} = \left| \frac{\partial v_{\text{turb}}}{\partial T} \delta T \right|, \quad (\text{B.2})$$

$$= \frac{k}{\mu m_p} \left(\Delta V^2 - \frac{2kT}{\mu m_p} \right)^{-1/2} \delta T. \quad (\text{B.3})$$

Dividing by v_{turb} to obtain the relative error gives

$$\frac{\delta v_{\text{turb}}}{v_{\text{turb}}} = \frac{k}{\mu m_p} \left(\Delta V^2 - \frac{2kT}{\mu m_p} \right)^{-1} \delta T. \quad (\text{B.4})$$

From rearranging Eq. B.1 for ΔV ,

$$\Delta V_i^2 = v_{\text{turb}}^2 + \frac{2kT}{\mu_i m_p} \quad (\text{B.5})$$

$$= \frac{2kT}{m_p} \left(\frac{\mathcal{M}^2}{\mu_H} + \frac{1}{\mu_i} \right) \quad \text{where} \quad \mathcal{M} \equiv \frac{v_{\text{turb}}}{\sqrt{2c_s}}, \quad (\text{B.6})$$

we can substitute this into Eq. B.4 to yield

$$\frac{\delta v_{\text{turb}}}{v_{\text{turb}}} = \frac{k}{\mu m_p} \left(\frac{2kT}{m_p} \left[\frac{\mathcal{M}^2}{\mu_H} + \frac{1}{\mu} \right] - \frac{2kT}{\mu m_p} \right)^{-1} \delta T, \quad (\text{B.7})$$

$$= \frac{2\mu_H}{\mu \mathcal{M}^2} \frac{\delta T}{T}. \quad (\text{B.8})$$

B.2 Co-spatial Kinetic Temperature

The kinetic temperature and its associated uncertainty are

$$T = \frac{m_p}{2k} \frac{\mu_a \mu_b}{\mu_b - \mu_a} (\Delta V_a^2 - \Delta V_b^2), \quad (\text{B.9})$$

$$\delta T = \frac{2m_p}{2k} \frac{\mu_A \mu_B}{\mu_B - \mu_A} \sqrt{(\Delta V_A \cdot \delta \Delta V_A)^2 + (\Delta V_B \cdot \delta \Delta V_B)^2}. \quad (\text{B.10})$$

We assume that the relative errors on the line width are proportional to one another such that,

$$\frac{\delta \Delta V_A}{\Delta V_A} = x \cdot \frac{\delta \Delta V_B}{\Delta V_B} = \frac{\delta \Delta V}{\Delta V}, \quad (\text{B.11})$$

where x scales the relative errors if they are not the same; Fig. 5.9 uses $x = 1$. Substituting these into the Eq. B.10 yields

$$\delta T = 2 \frac{m_p}{2k} \frac{\mu_A \mu_B}{\mu_B - \mu_A} \sqrt{\left(\Delta V_A^2 \cdot \frac{\delta \Delta V}{\Delta V}\right)^2 + \left(\frac{\Delta V_B^2}{x} \cdot \frac{\delta \Delta V}{\Delta V}\right)^2}, \quad (\text{B.12})$$

$$= 2 \frac{m_p}{2k} \frac{\mu_A \mu_B}{\mu_B - \mu_A} \frac{\delta \Delta V}{\Delta V} \sqrt{\Delta V_A^4 + \frac{\Delta V_B^4}{x^2}}. \quad (\text{B.13})$$

Substituting for ΔV_A^4 and ΔV_B^4 from Eq. B.6 and rearranging for the relative uncertainty on T ,

$$\frac{\delta T}{T} = \frac{2\mu_A \mu_B}{\mu_B - \mu_A} \frac{\delta \Delta V}{\Delta V} \sqrt{\left(\frac{\mathcal{M}^2}{\mu_H} + \frac{1}{\mu_A}\right)^2 + \frac{1}{x^2} \cdot \left(\frac{\mathcal{M}^2}{\mu_H} + \frac{1}{\mu_B}\right)^2}. \quad (\text{B.14})$$

B.3 Co-spatial Turbulent Velocity Dispersion

This can be repeated with the turbulent velocity dispersion:

$$v_{\text{turb}} = \sqrt{\frac{\mu_B \Delta V_B^2 - \mu_A \Delta V_A^2}{\mu_B - \mu_A}} \quad (\text{B.15})$$

$$\delta v_{\text{turb}} = \sqrt{\frac{(\mu_B \Delta V_B \delta \Delta V_B)^2 + (\mu_A \Delta V_A \delta \Delta V_A)^2}{(\mu_B - \mu_A) \cdot (\mu_B \Delta V_B^2 - \mu_A \Delta V_A^2)}}. \quad (\text{B.16})$$

Substituting for the relative line widths from Eq. B.11 and for v_{turb} from Eq. B.1 gives

$$\delta v_{\text{turb}} = \frac{1}{\mu_B - \mu_A} \frac{1}{v_{\text{turb}}} \frac{\delta \Delta V}{\Delta V} \sqrt{\mu_A^2 \Delta V_A^4 + \frac{\mu_B^2}{x^2} \Delta V_B^4}. \quad (\text{B.17})$$

Rearranging Eq. B.6 yields

$$\mu_i \Delta V_i^2 = v_{\text{turb}}^2 \left(\mu_i + \frac{\mu_H}{\mathcal{M}^2} \right), \quad (\text{B.18})$$

which can be substituted into Eq. B.17. After some rearranging, we find

$$\frac{\delta v_{\text{turb}}}{v_{\text{turb}}} = \frac{1}{\mu_B - \mu_A} \frac{\delta \Delta V}{\Delta V} \sqrt{\left(\mu_A + \frac{\mu_H}{\mathcal{M}^2}\right)^2 + \frac{1}{x^2} \cdot \left(\mu_B + \frac{\mu_H}{\mathcal{M}^2}\right)^2}. \quad (\text{B.19})$$

Physical Models from Chapter 6

This Appendix contains all the physical models used for the modelling in Chapter 6. The fiducial model is that of [Gorti et al. \(2011\)](#), the end product of a modelling effort to fit a range of integrated line intensities of TW Hya.

The surface density is given by,

$$\Sigma_0 = 500 r^{-0.7} \exp\left(-\frac{r^{1.3}}{100}\right) \text{ g cm}^{-2}, \quad (\text{C.1})$$

where r is the radial distance in au. The model has a gas mass of $0.06 M_\odot$, a homogeneous gas-to-dust ratio of 100 and an MRN-like grain size distribution, $n(a) \propto a^{-3.5}$, with maximum and minimum sizes of 1 mm and $0.09 \mu\text{m}$ respectively. Gas and dust temperatures are treated independently allowing the gas temperatures in the upper, more strongly irradiated regions of the disk to deviate strongly from those of the dust.

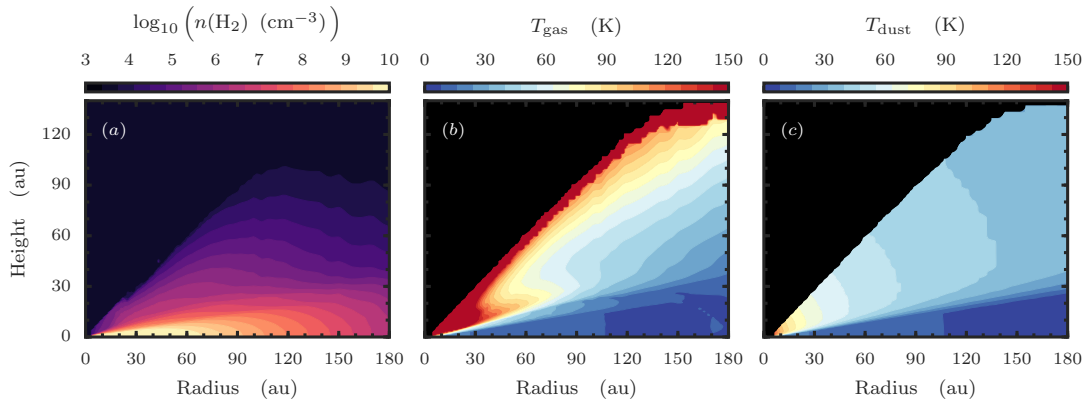


Figure C.1 Physical structure of Model A, the fiducial model used in Chapter 6. The left panel shows the $n(\text{H}_2)$ structure, while the central and right-most panels show the gas and dust temperatures respectively. Note that the gas temperature has been clipped at 150 K in order to better see the global structure.

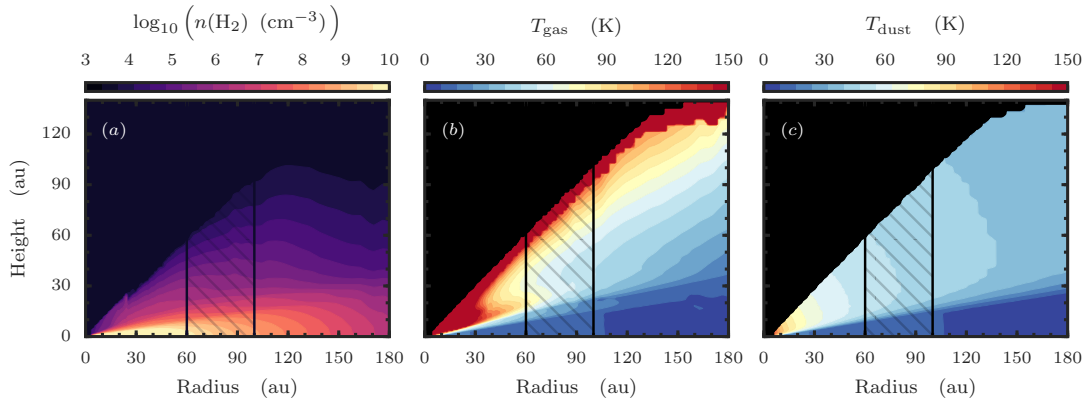


Figure C.2 As Fig. C.1 but for Model B. Hatched regions shows the perturbation.

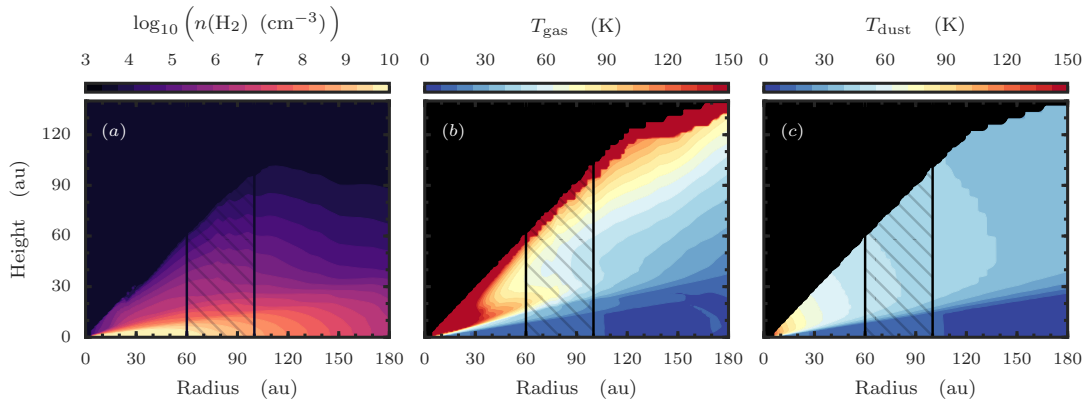


Figure C.3 As Fig. C.1 but for Model Bd. Hatched regions shows the perturbation.

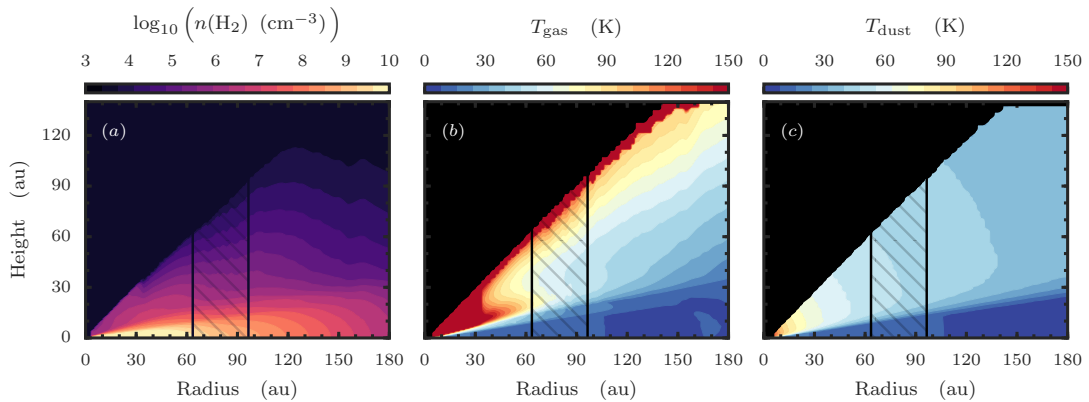


Figure C.4 As Fig. C.1 but for Model C. Hatched regions shows the perturbation.

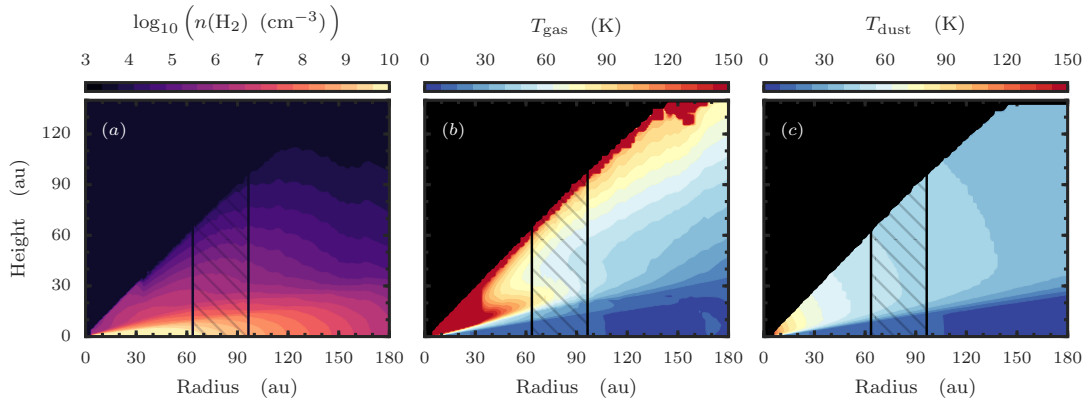


Figure C.5 As Fig. C.1 but for Model Cd. Hatched regions shows the perturbation.

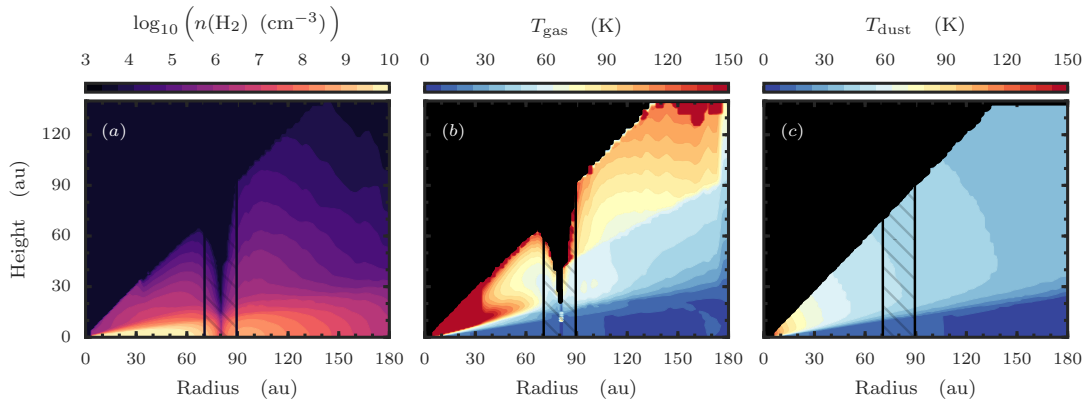


Figure C.6 As Fig. C.1 but for Model D. Hatched regions shows the perturbation.

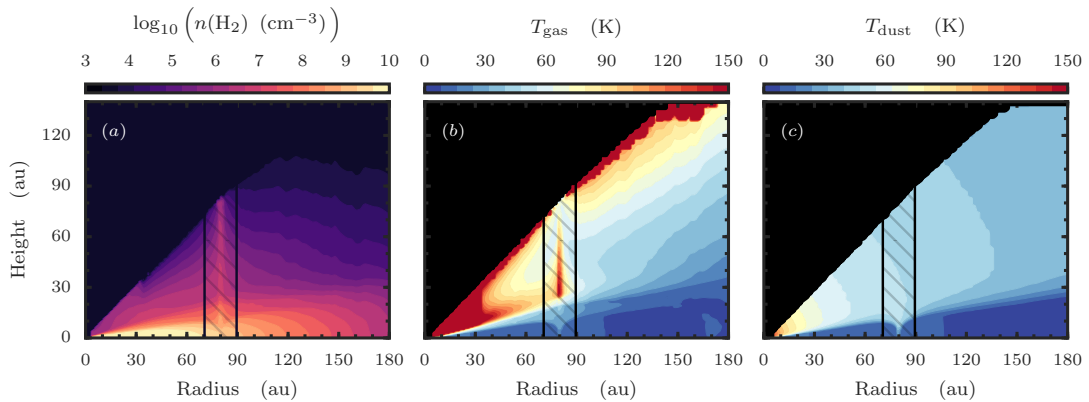


Figure C.7 As Fig. C.1 but for Model Dd. Hatched regions shows the perturbation.

Glossary

- ALMA** Atacama Large Millimetre Array.
- CASA** Common Astronomy Software Applications.
- CRP** cosmic ray particles.
- E-ELT** European Extremely Large Telescope.
- ESA** European Space Agency.
- eVLA** Extended Very Large Array.
- FUV** far-ultraviolet.
- GPI** Gemini Planet Imager.
- HST** Hubble Space Telescope.
- IR** infra-red.
- IRAM** Institut de Radioastronomie Millimétrique.
- IRAS** Infrared Astronomical Satellite.
- ISM** interstellar medium.
- JWST** James Webb Space Telescope.
- KIDA** Kinetic Database for Astrochemistry.
- LAMDA** Leiden Atomic and Molecular Database.
- LTE** local thermodynamic equilibrium.
- MCMC** Monte-Carlo Markov Chain.
- MHD** magneto-hydrodynamic.
- MRI** magneto-rotational instability.
- non-LTE** non-local thermodynamic equilibrium.
- OPR** ortho-to-para ratio.
- PdBI** Plateau de Bure Interferometer.
- PSF** point spread function.
- SED** spectral energy distribution.
- SLRN** short lived radionuclides.
- SMA** Smithsonian Millimetre Array.
- SNR** signal-to-noise ratio.
- SOFIA** Stratospheric Observatory for Infrared Astronomy.
- SPHERE** Spectro-Polarimetric High-contrast Exoplanet Research.
- UMIST** University of Manchester Institute of Science and Technology.
- UV** ultraviolet.
- VLA** Karl G. Jansky Very Large Array.
- VLT** Very Large Telescope.
- YSO** young stellar object.

Bibliography

- Agúndez, M., & Wakelam, V. 2013, *Chemical Reviews*, 113, 8710
- Aikawa, Y., & Herbst, E. 1999, *A&A*, 351, 233
- Aikawa, Y., van Zadelhoff, G. J., van Dishoeck, E. F., & Herbst, E. 2002, *A&A*, 386, 622
- Akimkin, V., Zhukovska, S., Wiebe, D., et al. 2013, *ApJ*, 766, 8
- Akiyama, E., Momose, M., Hayashi, H., & Kitamura, Y. 2011, *PASJ*, 63, 1059
- Akiyama, E., Muto, T., Kusakabe, N., et al. 2015, *ApJL*, 802, L17
- Albertsson, T., Semenov, D., & Henning, T. 2014, *ApJ*, 784, 39
- Albertsson, T., Semenov, D. A., Vasyunin, A. I., Henning, T., & Herbst, E. 2013, *ApJS*, 207, 27
- ALMA Partnership, Brogan, C. L., Pérez, L. M., et al. 2015, *ApJL*, 808, L3
- Altwegg, K., Balsiger, H., Bar-Nun, A., et al. 2015, *Science*, 347, 1261952
- Andre, P., Ward-Thompson, D., & Barsony, M. 1993, *ApJ*, 406, 122
- Andrews, S. M., Rosenfeld, K. A., Kraus, A. L., & Wilner, D. J. 2013, *ApJ*, 771, 129
- Andrews, S. M., & Williams, J. P. 2007, *ApJ*, 659, 705
- Andrews, S. M., Wilner, D. J., Hughes, A. M., Qi, C., & Dullemond, C. P. 2010, *ApJ*, 723, 1241
- Andrews, S. M., Wilner, D. J., Hughes, A. M., et al. 2012, *ApJ*, 744, 162
- Andrews, S. M., Wilner, D. J., Zhu, Z., et al. 2016, *ApJL*, 820, L40
- Ansdell, M., Williams, J. P., van der Marel, N., et al. 2016, *ApJ*, 828, 46
- Armitage, P. J. 2015, *ArXiv e-prints*, arXiv:1509.06382
- Balbus, S. A., & Hawley, J. F. 1990, in *Bulletin of the American Astronomical Society*, Vol. 22, *Bulletin of the American Astronomical Society*, 1209
- Barenfeld, S. A., Carpenter, J. M., Ricci, L., & Isella, A. 2016, *ApJ*, 827, 142
- Beckwith, S. V. W., Sargent, A. I., Chini, R. S., & Guesten, R. 1990, *AJ*, 99, 924
- Benisty, M., Juhasz, A., Boccaletti, A., et al. 2015, *A&A*, 578, L6
- Bergin, E., Calvet, N., D'Alessio, P., & Herczeg, G. J. 2003, *ApJL*, 591, L159
- Bergin, E. A., Du, F., Cleeves, L. I., et al. 2016, *ArXiv e-prints*, arXiv:1609.06337
- Bergin, E. A., Cleeves, L. I., Gorti, U., et al. 2013, *Nature*, 493, 644
- Bethell, T. J., & Bergin, E. A. 2011, *ApJ*, 739, 78
- Biham, O., Furman, I., Pirronello, V., & Vidali, G. 2001, *ApJ*, 553, 595
- Birnstiel, T., Andrews, S. M., Pinilla, P., & Kama, M. 2015, *ApJL*, 813, L14

- Blum, J., & Wurm, G. 2008, *ARA&A*, 46, 21
- Bohren, C. F., & Huffman, D. R. 1998, *Absorption and Scattering of Light by Small Particles*, 544
- Brickhouse, N. S., Cranmer, S. R., Dupree, A. K., et al. 2012, *ApJL*, 760, L21
- Brinch, C., & Hogerheijde, M. R. 2010, *A&A*, 523, A25
- Bruderer, S. 2013, *A&A*, 559, A46
- Bruderer, S., Doty, S. D., & Benz, A. O. 2009, *ApJS*, 183, 179
- Bruderer, S., van Dishoeck, E. F., Doty, S. D., & Herczeg, G. J. 2012, *A&A*, 541, A91
- Butner, H. M., Lada, E. A., & Loren, R. B. 1995, *ApJ*, 448, 207
- Calvet, N., D'Alessio, P., Watson, D. M., et al. 2005, *ApJL*, 630, L185
- Cannon, C. J. 1973, *ApJ*, 185, 621
- Carrasco-González, C., Henning, T., Chandler, C. J., et al. 2016, *ApJL*, 821, L16
- Carrera, D., Johansen, A., & Davies, M. B. 2015, *A&A*, 579, A43
- Casassus, S., Cabrera, G. F., Förster, F., et al. 2006, *ApJ*, 639, 951
- Casassus, S., van der Plas, G., M, S. P., et al. 2013, *Nature*, 493, 191
- Caselli, P., & Ceccarelli, C. 2012, *A&A Rv*, 20, 56
- Caselli, P., Stantcheva, T., Shalabiea, O., Shematovich, V. I., & Herbst, E. 2002, *Planet. Space Sci.*, 50, 1257
- Caselli, P., Vastel, C., Ceccarelli, C., et al. 2008, *A&A*, 492, 703
- Chapillon, E., Guilloteau, S., Dutrey, A., Piétu, V., & Guélin, M. 2012, *A&A*, 537, A60
- Chiang, E. I., & Goldreich, P. 1997, *ApJ*, 490, 368
- Cleeves, L. I. 2016, *ApJL*, 816, L21
- Cleeves, L. I., Adams, F. C., & Bergin, E. A. 2013a, *ApJ*, 772, 5
- Cleeves, L. I., Adams, F. C., Bergin, E. A., & Visser, R. 2013b, *ApJ*, 777, 28
- Cleeves, L. I., Bergin, E. A., & Adams, F. C. 2014a, *ApJ*, 794, 123
- Cleeves, L. I., Bergin, E. A., Alexander, C. M. O. ., et al. 2014b, *Science*, 345, 1590
- Cleeves, L. I., Bergin, E. A., & Harries, T. J. 2015a, *ApJ*, 807, 2
- Cleeves, L. I., Bergin, E. A., Qi, C., Adams, F. C., & Öberg, K. I. 2015b, *ApJ*, 799, 204
- Cossins, P., Lodato, G., & Testi, L. 2010, *MNRAS*, 407, 181
- Crabtree, K. N., Indriolo, N., Kreckel, H., Tom, B. A., & McCall, B. J. 2011, *ApJ*, 729, 15
- Crida, A., Morbidelli, A., & Masset, F. 2006, *Icarus*, 181, 587
- Cridland, A. J., Pudritz, R. E., & Alessi, M. 2016, *MNRAS*, 461, 3274
- Crossfield, I. J. M. 2015, *PASP*, 127, 941
- Cuzzi, J. N., Hartlep, T., & Estrada, P. R. 2016, in *Lunar and Planetary Science Conference, Vol. 47, Lunar and Planetary Science Conference*, 2661
- Cuzzi, J. N., Hogan, R. C., Paque, J. M., & Dobrovolskis, A. R. 2001, *ApJ*, 546, 496
- D'Alessio, P., Calvet, N., Hartmann, L., Lizano, S., & Cantó, J. 1999, *ApJ*, 527, 893
- Dartois, E., Dutrey, A., & Guilloteau, S. 2003, *A&A*, 399, 773

- Debes, J. H., Jang-Condell, H., Weinberger, A. J., Roberge, A., & Schneider, G. 2013, *ApJ*, 771, 45
- Douglas, T. A., Caselli, P., Ilee, J. D., et al. 2013, *MNRAS*, 433, 2064
- Draine, B. T. 1978, *ApJS*, 36, 595
- Draine, B. T., & Bertoldi, F. 1996, *ApJ*, 468, 269
- Drążkowska, J., & Dullemond, C. P. 2014, *A&A*, 572, A78
- Drozdovskaya, M. N., Walsh, C., van Dishoeck, E. F., et al. 2016, *MNRAS*, 462, 977
- Duffell, P. C. 2015, *ApJL*, 807, L11
- Dullemond, C. P. 2012, *RADMC-3D: A multi-purpose radiative transfer tool*, , arXiv:1202.015
- Dullemond, C. P., & Dominik, C. 2005, *A&A*, 434, 971
- Dutrey, A., Guilloteau, S., & Guelin, M. 1997, *A&A*, 317, L55
- Dutrey, A., Guilloteau, S., & Simon, M. 1994, *A&A*, 286, 149
- Dutrey, A., Henning, T., Guilloteau, S., et al. 2007, *A&A*, 464, 615
- Dutrey, A., Wakelam, V., Boehler, Y., et al. 2011, *A&A*, 535, A104
- Ercolano, B., Mayr, D., Owen, J. E., Rosotti, G., & Manara, C. F. 2014, *MNRAS*, 439, 256
- Favre, C., Cleeves, L. I., Bergin, E. A., Qi, C., & Blake, G. A. 2013, *ApJL*, 776, L38
- Fayolle, E. C., Bertin, M., Romanzin, C., et al. 2011, *ApJL*, 739, L36
- Fayolle, E. C., Bertin, M., Romanzin, C., et al. 2013, *A&A*, 556, A122
- Fedele, D., van den Ancker, M. E., Henning, T., Jayawardhana, R., & Oliveira, J. M. 2010, *A&A*, 510, A72
- Finocchi, F., Gail, H.-P., & Duschl, W. J. 1997, *A&A*, 325, 1264
- Flaherty, K. M., Hughes, A. M., Rosenfeld, K. A., et al. 2015, *ApJ*, 813, 99
- Flock, M., Ruge, J. P., Dzyurkevich, N., et al. 2015, *A&A*, 574, A68
- Flower, D. R., Pineau des Forêts, G., & Walmsley, C. M. 2004, *A&A*, 427, 887
- Flower, D. R., Pineau Des Forêts, G., & Walmsley, C. M. 2006, *A&A*, 449, 621
- Foreman-Mackey, D., Hogg, D. W., Lang, D., & Goodman, J. 2013, *PASP*, 125, 306
- Forgan, D., Armitage, P. J., & Simon, J. B. 2012, *MNRAS*, 426, 2419
- Fung, J., Shi, J.-M., & Chiang, E. 2014, *ApJ*, 782, 88
- Gaia Collaboration, Brown, A. G. A., Vallenari, A., et al. 2016, *ArXiv e-prints*, arXiv:1609.04172
- Gammie, C. F. 2001, *ApJ*, 553, 174
- Garrod, R. T., & Herbst, E. 2006, *A&A*, 457, 927
- Garrod, R. T., Wakelam, V., & Herbst, E. 2007, *A&A*, 467, 1103
- Gerlich, D. 1990, *JChPh*, 92, 2377
- Gerlich, D., Herbst, E., & Roueff, E. 2002, *Planet. Space Sci.*, 50, 1275
- Glassgold, A. E., Feigelson, E. D., Montmerle, T., & Wolk, S. 2005, in *Astronomical Society of the Pacific Conference Series*, Vol. 341, *Chondrites and the Protoplanetary Disk*, ed. A. N. Krot, E. R. D. Scott, & B. Reipurth, 165
- Glassgold, A. E., Najita, J., & Igea, J. 1997a, *ApJ*, 480, 344

- Glassgold, A. E., Najita, J., & Igea, J. 1997b, *ApJ*, 485, 920
- Goldreich, P., & Ward, W. R. 1973, *ApJ*, 183, 1051
- Gorti, U., Hollenbach, D., Najita, J., & Pascucci, I. 2011, *ApJ*, 735, 90
- Graedel, T. E., Langer, W. D., & Frerking, M. A. 1982, *ApJS*, 48, 321
- Greene, T. P., Wilking, B. A., Andre, P., Young, E. T., & Lada, C. J. 1994, *ApJ*, 434, 614
- Guelin, M., Langer, W. D., Snell, R. L., & Wootten, H. A. 1977, *ApJL*, 217, L165
- Guilloteau, S., Di Folco, E., Dutrey, A., et al. 2013, *A&A*, 549, A92
- Guilloteau, S., & Dutrey, A. 1998, *A&A*, 339, 467
- Guilloteau, S., Dutrey, A., Wakelam, V., et al. 2012, *A&A*, 548, A70
- Guilloteau, S., Piétu, V., Dutrey, A., & Guélin, M. 2006, *A&A*, 448, L5
- Guilloteau, S., Piétu, V., Chapillon, E., et al. 2016, *A&A*, 586, L1
- Gullbring, E., Hartmann, L., Briceño, C., & Calvet, N. 1998, *ApJ*, 492, 323
- Harries, T. J., Monnier, J. D., Symington, N. H., & Kurosawa, R. 2004, *MNRAS*, 350, 565
- Hartigan, P., Edwards, S., & Ghandour, L. 1995, *ApJ*, 452, 736
- Hartmann, L., Calvet, N., Gullbring, E., & D'Alessio, P. 1998, *ApJ*, 495, 385
- Hasegawa, T. I., Herbst, E., & Leung, C. M. 1992, *ApJS*, 82, 167
- Henning, T., & Meeus, G. 2011, *Dust Processing and Mineralogy in Protoplanetary Accretion Disks*, 114–148
- Henning, T., & Semenov, D. 2013, *Chemical Reviews*, 113, 9016
- Henning, T., Semenov, D., Guilloteau, S., et al. 2010, *ApJ*, 714, 1511
- Herbig, G. H. 1960, *ApJS*, 4, 337
- Herbst, E., & Klemperer, W. 1973, *ApJ*, 185, 505
- Högbom, J. A. 1974, *A&AS*, 15, 417
- Hogerheijde, M. R., Bekkers, D., Pinilla, P., et al. 2016, *A&A*, 586, A99
- Hollenbach, D., Johnstone, D., Lizano, S., & Shu, F. 1994, *ApJ*, 428, 654
- Honvault, P., Jorfi, M., González-Lezana, T., Faure, A., & Pagani, L. 2011, *Physical Review Letters*, 107, 023201
- Horne, K., & Marsh, T. R. 1986, *MNRAS*, 218, 761
- Huang, J., & Öberg, K. I. 2015, *ApJL*, 809, L26
- Huang, J., Öberg, K. I., & Andrews, S. M. 2016, *ApJL*, 823, L18
- Hughes, A. M., Wilner, D. J., Andrews, S. M., Qi, C., & Hogerheijde, M. R. 2011, *ApJ*, 727, 85
- Hugo, E., Asvany, O., & Schlemmer, S. 2009, *JChPh*, 130, 164302
- Ida, S., & Lin, D. N. C. 2004, *ApJ*, 616, 567
- Johansen, A., Oishi, J. S., Mac Low, M.-M., et al. 2007, *Nature*, 448, 1022
- Johansen, A., Youdin, A., & Mac Low, M.-M. 2009, *ApJL*, 704, L75
- Jonkheid, B., Faas, F. G. A., van Zadelhoff, G.-J., & van Dishoeck, E. F. 2004, *A&A*, 428, 511
- Kama, M., Bruderer, S., Carney, M., et al. 2016a, *A&A*, 588, A108

- Kama, M., Bruderer, S., van Dishoeck, E. F., et al. 2016b, *A&A*, 592, A83
- Kamp, I. 2015, in *European Physical Journal Web of Conferences*, Vol. 102, *European Physical Journal Web of Conferences*, 00010
- Kastner, J. H., Hily-Blant, P., Rodriguez, D. R., Punzi, K., & Forveille, T. 2014, *ApJ*, 793, 55
- Kastner, J. H., Qi, C., Gorti, U., et al. 2015, *ApJ*, 806, 75
- Kataoka, A., Tanaka, H., Okuzumi, S., & Wada, K. 2013, *A&A*, 557, L4
- Katz, N., Furman, I., Biham, O., Pirronello, V., & Vidali, G. 1999, *ApJ*, 522, 305
- Keto, E. R. 1990, *ApJ*, 355, 190
- Klahr, H., & Hubbard, A. 2014, *ApJ*, 788, 21
- Klahr, H. H., & Bodenheimer, P. 2003, *ApJ*, 582, 869
- Kley, W., & Nelson, R. P. 2012, *ARA&A*, 50, 211
- Koerner, D. W., Sargent, A. I., & Beckwith, S. V. W. 1993, *Icarus*, 106, 2
- Lada, C. J. 1987, in *IAU Symposium*, Vol. 115, *Star Forming Regions*, ed. M. Peimbert & J. Jugaku, 1–17
- Lee, H.-H., Herbst, E., Pineau des Forets, G., Roueff, E., & Le Bourlot, J. 1996, *A&A*, 311, 690
- Lee, H.-H., Roueff, E., Pineau des Forets, G., et al. 1998, *A&A*, 334, 1047
- Lenz, D. D., & Ayres, T. R. 1992, *PASP*, 104, 1104
- Lin, D. N. C., & Papaloizou, J. 1986, *ApJ*, 309, 846
- Lique, F., Spielfiedel, A., Feautrier, N., et al. 2010, *JChPh*, 132, 024303
- Lissauer, J. J. 1993, *ARA&A*, 31, 129
- Loomis, R. A., Cleeves, L. I., Öberg, K. I., Guzman, V. V., & Andrews, S. M. 2015, *ApJL*, 809, L25
- Lovelace, R. V. E., Li, H., Colgate, S. A., & Nelson, A. F. 1999, *ApJ*, 513, 805
- Lynden-Bell, D., & Pringle, J. E. 1974, *MNRAS*, 168, 603
- Lyra, W., Turner, N. J., & McNally, C. P. 2015, *A&A*, 574, A10
- Mamajek, E. E. 2009, in *American Institute of Physics Conference Series*, Vol. 1158, *American Institute of Physics Conference Series*, ed. T. Usuda, M. Tamura, & M. Ishii, 3–10
- Manara, C. F., Testi, L., Natta, A., et al. 2014, *A&A*, 568, A18
- Manara, C. F., Rosotti, G., Testi, L., et al. 2016, *A&A*, 591, L3
- Mangum, J. G., & Shirley, Y. L. 2016, *PASP*, 128, 029201
- Marcus, P. S., Pei, S., Jiang, C.-H., et al. 2015, *ApJ*, 808, 87
- Mathews, G. S., Klaassen, P. D., Juhász, A., et al. 2013, *A&A*, 557, A132
- Mazzitelli, I. 1989, in *European Southern Observatory Conference and Workshop Proceedings*, Vol. 33, *European Southern Observatory Conference and Workshop Proceedings*, ed. B. Reipurth, 433–445
- McClure, M., Bergin, T., Cleeves, I., et al. 2016, *ArXiv e-prints*, arXiv:1608.07817
- McJunkin, M., France, K., Schneider, P. C., et al. 2014, *ApJ*, 780, 150
- Meeus, G., Waters, L. B. F. M., Bouwman, J., et al. 2001, *A&A*, 365, 476
- Menu, J., van Boekel, R., Henning, T., et al. 2014, *A&A*, 564, A93
- Miotello, A., Bruderer, S., & van Dishoeck, E. F. 2014, *A&A*, 572, A96

- Miotello, A., van Dishoeck, E. F., Kama, M., & Bruderer, S. 2016, *A&A*, 594, A85
- Mordasini, C., Alibert, Y., & Benz, W. 2009, *A&A*, 501, 1139
- Mordasini, C., Alibert, Y., Benz, W., Klahr, H., & Henning, T. 2012, *A&A*, 541, A97
- Müller, H. S. P., Thorwirth, S., Roth, D. A., & Winnewisser, G. 2001, *A&A*, 370, L49
- Muzerolle, J., Calvet, N., & Hartmann, L. 2001, *ApJ*, 550, 944
- Muzerolle, J., Luhman, K. L., Briceño, C., Hartmann, L., & Calvet, N. 2005, *ApJ*, 625, 906
- Natta, A., Testi, L., & Randich, S. 2006, *A&A*, 452, 245
- Nelson, R. P., Gressel, O., & Umurhan, O. M. 2013, *MNRAS*, 435, 2610
- Ng, K.-C. 1974, *JChPh*, 61, 2680
- Nomura, H., Tsukagoshi, T., Kawabe, R., et al. 2016, *ApJL*, 819, L7
- Öberg, K. I. 2016, in *IAU Symposium*, Vol. 314, *Young Stars & Planets Near the Sun*, ed. J. H. Kastner, B. Stelzer, & S. A. Metchev, 143–148
- Öberg, K. I., Fayolle, E. C., Cuppen, H. M., van Dishoeck, E. F., & Linnartz, H. 2009a, *A&A*, 505, 183
- Öberg, K. I., Furuya, K., Loomis, R., et al. 2015, *ApJ*, 810, 112
- Öberg, K. I., Murray-Clay, R., & Bergin, E. A. 2011a, *ApJL*, 743, L16
- Öberg, K. I., van Dishoeck, E. F., & Linnartz, H. 2009b, *A&A*, 496, 281
- Öberg, K. I., Qi, C., Fogel, J. K. J., et al. 2011b, *ApJ*, 734, 98
- O'dell, C. R., & Wen, Z. 1994, *ApJ*, 436, 194
- Okuzumi, S., Tanaka, H., Kobayashi, H., & Wada, K. 2012, *ApJ*, 752, 106
- Ormel, C. W., & Klahr, H. H. 2010, *A&A*, 520, A43
- Ossenkopf, V., & Henning, T. 1994, *A&A*, 291, 943
- Pagani, L., Lesaffre, P., Jorfi, M., et al. 2013, *A&A*, 551, A38
- Pagani, L., Salez, M., & Wannier, P. G. 1992, *A&A*, 258, 479
- Pagani, L., Vastel, C., Hugo, E., et al. 2009, *A&A*, 494, 623
- Pascucci, I., Sterzik, M., Alexander, R. D., et al. 2011, *ApJ*, 736, 13
- Pascucci, I., Testi, L., Herczeg, G. J., et al. 2016, *ArXiv e-prints*, arXiv:1608.03621
- Piétu, V., Dutrey, A., & Guilloteau, S. 2007, *A&A*, 467, 163
- Pohl, A., Pinilla, P., Benisty, M., et al. 2015, *MNRAS*, 453, 1768
- Pringle, J. E. 1981, *ARA&A*, 19, 137
- Qi, C., D'Alessio, P., Öberg, K. I., et al. 2011, *ApJ*, 740, 84
- Qi, C., Öberg, K. I., Andrews, S. M., et al. 2015, *ApJ*, 813, 128
- Qi, C., Wilner, D. J., Aikawa, Y., Blake, G. A., & Hogerheijde, M. R. 2008, *ApJ*, 681, 1396
- Qi, C., Ho, P. T. P., Wilner, D. J., et al. 2004, *ApJL*, 616, L11
- Qi, C., Öberg, K. I., Wilner, D. J., et al. 2013, *Science*, 341, 630
- Rapson, V. A., Kastner, J. H., Millar-Blanchaer, M. A., & Dong, R. 2015, *ApJL*, 815, L26
- Reboussin, L., Guilloteau, S., Simon, M., et al. 2015, *A&A*, 578, A31

- Rice, W. K. M., Lodato, G., & Armitage, P. J. 2005, *MNRAS*, 364, L56
- Richard, S., Nelson, R. P., & Umurhan, O. M. 2016, *MNRAS*, 456, 3571
- Roberge, A., Weinberger, A. J., & Malumuth, E. M. 2005, *ApJ*, 622, 1171
- Roberts, H., Herbst, E., & Millar, T. J. 2004, *A&A*, 424, 905
- Roberts, H., & Millar, T. J. 2000, *A&A*, 361, 388
- Rodgers, S. D., & Millar, T. J. 1996, *MNRAS*, 280, 1046
- Rosenfeld, K. A., Andrews, S. M., Hughes, A. M., Wilner, D. J., & Qi, C. 2013, *ApJ*, 774, 16
- Rosenfeld, K. A., Qi, C., Andrews, S. M., et al. 2012, *ApJ*, 757, 129
- Roueff, E., Lis, D. C., van der Tak, F. F. S., Gerin, M., & Goldsmith, P. F. 2005, *A&A*, 438, 585
- Ruffle, D. P., & Herbst, E. 2000, *MNRAS*, 319, 837
- Rybicki, G. B., & Lightman, A. P. 1979, *Radiative processes in astrophysics*
- Safronov, V. S. 1972, *Evolution of the protoplanetary cloud and formation of the earth and planets.*
- Sargent, A. I., & Beckwith, S. 1987, *ApJ*, 323, 294
- Sargent, A. I., & Beckwith, S. V. W. 1991, *ApJL*, 382, L31
- Schöier, F. L., van der Tak, F. F. S., van Dishoeck, E. F., & Black, J. H. 2005, *A&A*, 432, 369
- Schwarz, K. R., Bergin, E. A., Cleeves, L. I., et al. 2016, *ApJ*, 823, 91
- Semenov, D., & Wiebe, D. 2011, *ApJS*, 196, 25
- Semenov, D., Wiebe, D., & Henning, T. 2004, *A&A*, 417, 93
- Semenov, D., Hersant, F., Wakelam, V., et al. 2010, *A&A*, 522, A42
- Shakura, N. I., & Sunyaev, R. A. 1973, *A&A*, 24, 337
- Shirley, Y. L. 2015, *PASP*, 127, 299
- Simon, J. B., Hughes, A. M., Flaherty, K. M., Bai, X.-N., & Armitage, P. J. 2015, *ApJ*, 808, 180
- Simon, M., Dutrey, A., & Guilloteau, S. 2000, *ApJ*, 545, 1034
- Sipilä, O., Caselli, P., & Harju, J. 2013, *A&A*, 554, A92
- Skatrud, D. D., De Lucia, F. C., Blake, G. A., & Sastry, K. V. L. N. 1983, *Journal of Molecular Spectroscopy*, 99, 35
- Smith, B. A., & Terrile, R. J. 1984, *Science*, 226, 1421
- Stoll, M. H. R., & Kley, W. 2014, *A&A*, 572, A77
- Takahashi, S. Z., Tsukamoto, Y., & Inutsuka, S. 2016, *MNRAS*, 458, 3597
- Tazzari, M., Testi, L., Ercolano, B., et al. 2016, *A&A*, 588, A53
- Teague, R., Semenov, D., Guilloteau, S., et al. 2015, *A&A*, 574, A137
- Teague, R., Guilloteau, S., Semenov, D., et al. 2016, *A&A*, 592, A49
- Testi, L., Birnstiel, T., Ricci, L., et al. 2014, *Protostars and Planets VI*, 339
- Thi, W.-F., Mathews, G., Ménard, F., et al. 2010, *A&A*, 518, L125
- Thommes, E. W., & Duncan, M. J. 2006, *The accretion of giant-planet cores*, ed. H. Klahr & W. Brandner (Cambridge University Press), 129

- Thommes, E. W., Duncan, M. J., & Levison, H. F. 2003, *Icarus*, 161, 431
- Tsukagoshi, T., Nomura, H., Muto, T., et al. 2016, *ApJL*, 829, L35
- Turner, N. J., Fromang, S., Gammie, C., et al. 2014, *Protostars and Planets VI*, 411
- van Boekel, R., SPHERE Collaboration, & Other, A. N. in press, *ApJ*
- van der Marel, N., van Dishoeck, E. F., Bruderer, S., et al. 2013, *Science*, 340, 1199
- van Dishoeck, E. F., Jonkheid, B., & van Hemert, M. C. 2006, *Faraday Discussions*, 133, 231
- van Dishoeck, E. F., Thi, W.-F., & van Zadelhoff, G.-J. 2003, *A&A*, 400, L1
- van Leeuwen, F. 2007, *A&A*, 474, 653
- Varnière, P., & Tagger, M. 2006, *A&A*, 446, L13
- Vasyunin, A. I., & Herbst, E. 2013, *ApJ*, 769, 34
- Vaupré, S., Hily-Blant, P., Ceccarelli, C., et al. 2014, *A&A*, 568, A50
- Wagner, K., Apai, D., Kasper, M., & Robberto, M. 2015, *ApJL*, 813, L2
- Wakelam, V., Herbst, E., Loison, J.-C., et al. 2012, *ApJS*, 199, 21
- Walmsley, C. M., Flower, D. R., & Pineau des Forêts, G. 2004, *A&A*, 418, 1035
- Walsh, C., Nomura, H., & van Dishoeck, E. 2015, *A&A*, 582, A88
- Walsh, C., Loomis, R. A., Öberg, K. I., et al. 2016, *ApJL*, 823, L10
- Weidenschilling, S. J. 1977, *MNRAS*, 180, 57
- Weintraub, D. A., Zuckerman, B., & Masson, C. R. 1989, *ApJ*, 344, 915
- Wetherill, G. W., & Stewart, G. R. 1989, *Icarus*, 77, 330
- Whipple, F. L. 1972, in *From Plasma to Planet*, ed. A. Elvius, 211
- Willacy, K. 2007, *ApJ*, 660, 441
- Williams, J. P., & Best, W. M. J. 2014, *ApJ*, 788, 59
- Wilson, T., Rohlf, K., & Huettemeister, S. 2010, *Tools of Radio Astronomy* (Springer-Verlag Berlin Heidelberg)
- Wilson, T. L., & Rood, R. 1994, *ARA&A*, 32, 191
- Woitke, P. 2015, in *European Physical Journal Web of Conferences*, Vol. 102, *European Physical Journal Web of Conferences*, 00007
- Woitke, P., Kamp, I., & Thi, W.-F. 2009, *A&A*, 501, 383
- Yang, B., Stancil, P. C., Balakrishnan, N., & Forrey, R. C. 2010, *ApJ*, 718, 1062
- Yen, H.-W., Koch, P. M., Liu, H. B., et al. 2016, *ArXiv e-prints*, arXiv:1610.01780
- Youdin, A. N., & Goodman, J. 2005, *ApJ*, 620, 459
- Zakhochay, O. V., del Burgo, C., & Zakhochay, V. A. 2015, *Advances in Astronomy and Space Physics*, 5, 33
- Zhang, K., Bergin, E. A., Blake, G. A., et al. 2016, *ApJL*, 818, L16
- Zhang, K., Blake, G. A., & Bergin, E. A. 2015, *ApJL*, 806, L7
- Zsom, A., & Dullemond, C. P. 2008, *A&A*, 489, 931
- Zsom, A., Ormel, C. W., Güttler, C., Blum, J., & Dullemond, C. P. 2010, *A&A*, 513, A57

Acknowledgements

This thesis is the product of much support, friendship and generosity of many people.

First and foremost, thanks should go to my supervisors, Dima and Thomas. Your mentorship and advice over the last three and a bit years have been invaluable. The unbounded enthusiasm with which we have approached these projects has undoubtedly spurred me on to achieve far more than I had anticipated.

Special thanks should also go to the students at MPIA, who, while providing an immensely enjoyable and welcoming environment to work in, have helped immeasurably through discussing ideas, overcoming problems and putting up with numerous inane questions about plotting figures with `matplotlib`. Good luck with all your theses.

To my collaborators near and far, thank you for your advice and support while carrying out these projects. Having many pairs of eyes to look over drafts and your critical input has been indispensable.

Also all those involved with IMPRS, thank you for helping to stay sane. The retreats have been excellent fun and show that there's a lot more to science than just sitting at a computer. Particular thanks should also go to Christian Fendt for providing so many opportunities through the IMPRS-HD school.

Christina, thank you for making the last couple of years so great (and a particular thanks for the unenviable task of translating my abstract). Knowing you were there has made struggling through some of the tougher days possible. Here's to many more.

Finally, my parents. Mum, Dad: your unwavering support and encouragement over the last 26(ish) years has been amazing. Without you, I would not have achieved even half of what I have done now. Thank you for everything.